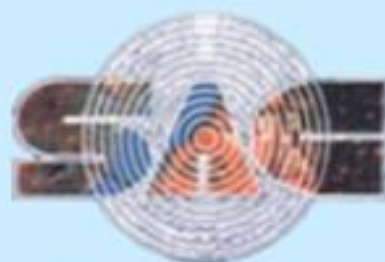
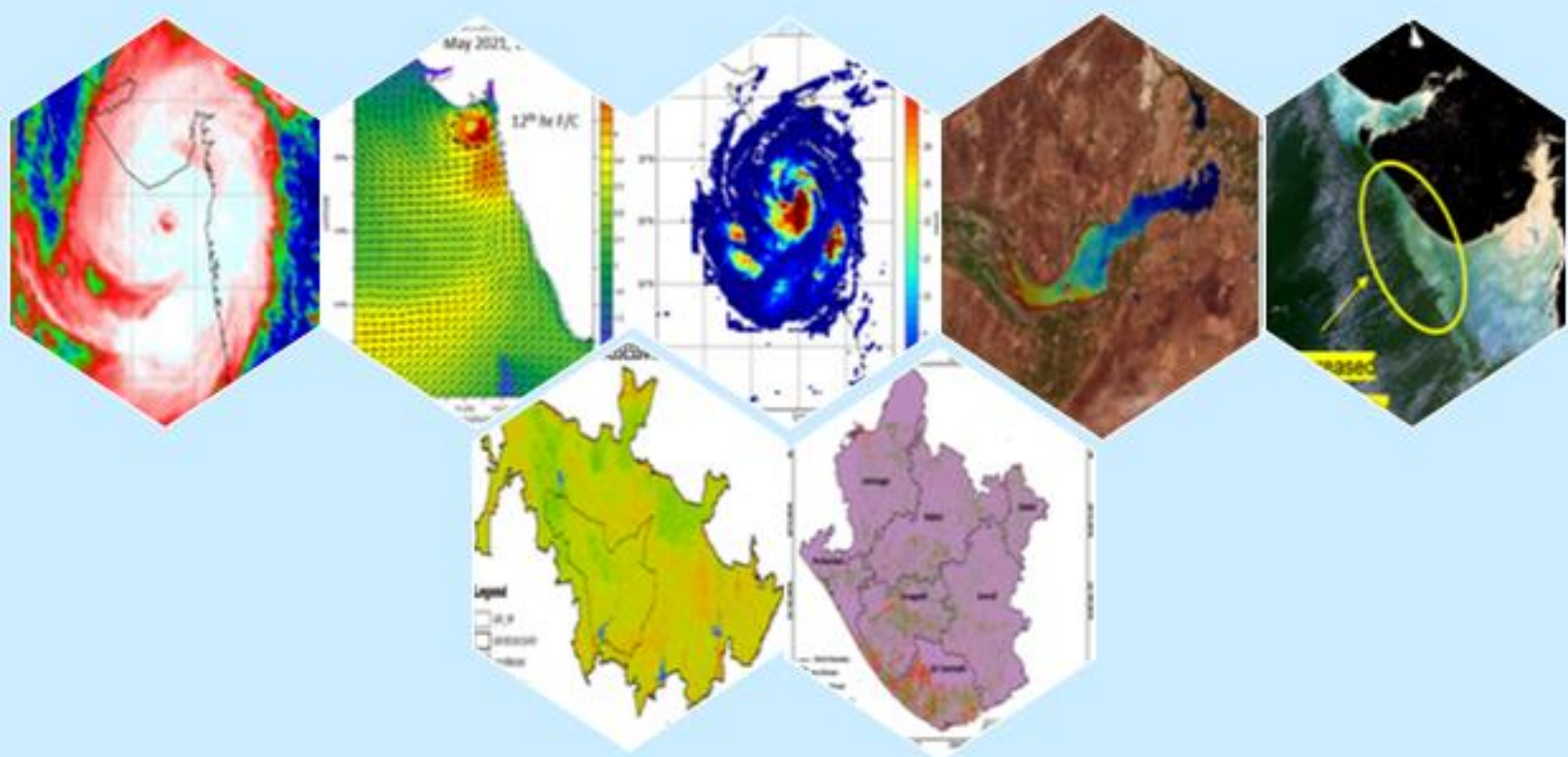


TROPICAL CYCLONE TAUKTAE

PREDICTION, MONITORING AND ANALYSIS OF AFTER EFFECTS
SAC/EPSA/SR-02/2021



Earth, Ocean, Atmosphere, Planetary Sciences and Applications Area
Space Applications Centre (ISRO), Ahmedabad-380015
July, 2021

Document Control and DATA Sheet

Report No.	SAC/EPSA/ SR-02/2021
Date	July, 2021
Title	Tropical Cyclone TAUKTAE: Prediction, Monitoring and Analysis of After Effects
Type of Report	Scientific Report
No. of Pages	117
Authors	Team
Number of Figures	68
Number of Tables	14
Number of References	60
Originating Unit	EPSA/SAC
Abstract	On May 14, 2021 an Extremely Severe Cyclonic Storm (ESCS) Tauktae developed over the Arabian Sea that hit the Saurashtra coast about 20 km northeast of Diu with maximum sustained wind speed (MSW) of 90 kts on May 17, 2021. Cyclone was continuously monitored in the real-time and forecasts were generated using a combination of satellite observations, statistical and dynamical models at Space Applications Centre (SAC/ISRO), Ahmedabad. Post-landfall effects of cyclone on coastal zone and resources, agricultural crops, forest regions, inland water inundation, and ocean primary productivity were analysed using in-situ observations, satellite data and numerical models. The role of satellite data in understanding different processes related to cyclone has been brought out in this report.
Key words	cyclone, prediction, satellite observations, sea surface temperature, storm surge, inundation, wave prediction, salinity, rainfall, flood, hydrological modelling, upwelling, biological productivity, chlorophyll, damage assessment, crops, forest
Security classification	Unrestricted

Team

1. Neeru Jaiswal
2. Shivani Shah
3. Anup Kumar Mandal
4. Seemanth M.
5. Jishad M.
6. Suchandra Aich Bhowmick
7. Neerja Sharma
8. Shard Chander
9. Amit K. Dubey
10. Vibhuti B. Jha
11. Rohit Pradhan
12. Nimisha Singh
13. Debojyoti Ganguly
14. R.K. Sarangi
15. N. Jaiganesh
16. Arvind Sahay
17. Saroj Maity
18. C. P. Singh
19. C. Patnaik
20. Ayan Das
21. Mukesh Kumar
22. Neeraj Agarwal
23. Mehul Pandya
24. Mini Raman
25. Bimal Bhattacharya
26. R.P. Singh
27. A K Varma
28. Rashmi Sharma
29. I. M. Bahuguna

Acknowledgements

The preparation of this report on various aspects of cyclone TAUKTAE was jointly carried out by scientists of a task team constituted by, Deputy Director, Earth, Ocean, Atmosphere and Planetary Science Applications Area (EPSA), SAC (ISRO).

Task team members wish to express sincere gratitude to the Director, SAC (ISRO), for his keen interest, overall guidance and encouragement for the work undertaken in this report.

Encouragement and persistent support with guidance given by Deputy Director, Earth, Ocean, Atmosphere and Planetary Science Applications Area (EPSA), SAC (ISRO) during the course of this work is gratefully acknowledged. He was instrumental in formation of the task teams with specific objectives and provided full support for successfully executing the study objectives.

It was not possible to complete the study without the support of various national and international agencies. We sincerely thank India Meteorological Department (IMD) for the real-time cyclone updates and for providing the best estimates of cyclone track and intensity. The data provided by Indian National Centre for Ocean Information Services (INCOIS) for oceanic studies is very much acknowledged. Authors are thankful to NDC/NRSC, Hyderabad for providing Oceansat-2 OCM datasets. Thanks are due to the National Center for Environmental Prediction (NCEP) for providing the valuable data for the models, JTWC for providing real-time cyclone track and intensity estimation, JAXA for providing GSMAp rainfall data, NASA archive for providing MODIS AQUA, VIIRS and OLCI data datasets which has been used to produce chlorophyll images and TRMM3B42 datasets which has been used to validate the rain products. The authors also acknowledge the Environmental Modeling Center (EMC) of NCEP for providing HWRF modeling system.

Authors are thankful to Google Earth Engine team for providing a cloud-based high performance platform for providing data and carrying out the analysis.

v

Summary

On May 14, 2021 an Extremely Severe Cyclonic Storm (ESCS) TAUKTAE developed over the Arabian Sea and hit the Saurashtra coast near Diu with maximum sustained wind speed (MSW) of 90 kts on May 17, 2021. Cyclone was continuously monitored in the real-time and forecasts were generated using a combination of satellite observations, statistical and dynamical models at Space Applications Centre (SAC/ISRO), Ahmedabad. Post-landfall effects of cyclone on coastal zone and resources, agricultural crops, forest regions, inland water inundation, and ocean primary productivity were analysed using in-situ observations, satellite data and numerical models. The role of satellite data in understanding different processes related to cyclone has been brought out in this report. Accurate predictions of cyclogenesis, intensification and landfall as well as the prediction of ocean state helped in saving many lives, due to appropriate measures by disaster management authorities.

The genesis potential parameter (GPP) using NCEP-GFS data showed the signatures of tropical cyclogenesis in Arabian Sea on 9th May. Once declared as a tropical storm by IMD, prediction of cyclone track and intensity were made at SAC using in-house dynamical-numerical modelling system comprising of SAC-Lagrangian Advection Model and Hurricane Weather Research Forecast (HWRF) model. These real-time predictions were validated using observations from India Meteorological Department. The 24 hour lead time prediction error in landfall position and time was about 31 km and 1 hour (delay), respectively. Apart from this, cyclone structural parameters and rapid changes in the inner core of TC were estimated using INSAT-3D data. The surface wind speed derived from SMAP satellite was also analyzed to study cyclone wind asymmetry.

In this study, satellite observations are explored to analyse the conducive ocean condition before formation of the cyclone primarily from the air-sea interaction perspective. Impact of the storm during and after passage of the cyclone is also observed using satellite measures and numerical models. Warming was observed in AS prior to the event, due to phenomenal freshening near the Kerala and Karnataka coasts. The warm SST anomalies along west coast of India along with anti-cyclonic eddies as observed in satellite based sea

level anomaly measurements indicated higher oceanic heat content. Surface cooling (~ 1°C) and enhancement in surface salinity (~ 0.5 – 1 psu) was observed after passage of the due to upwelling by Ekman pumping.

Precipitation during cyclone was well captured by H-E rainfall algorithm based on INSAT-3D satellite measurements. Tropical cyclone (TC) rain structure was captured well from genesis to dissipation. H-E recorded rain structure of cyclone very well and discriminated the warm eye from destructive eye wall region as well. The rain estimated from H-E shows good agreement with IMD surface observations and GPM-IMERG satellite products with R value of 0.5 and 0.59, respectively. Results infer the reliability and usefulness of H-E rain products from INSAT-3D/3DR in monitoring TC Tauktae rain over ocean and coastal regions as well.

In this report, various hydrological aspects are also analyzed with the help of remote sensing dataset with the aim of potential identification of most vulnerable areas for flood. The cyclone induced flood inundation probability was derived by making use of in-house developed SACHYDRO hydrological model. Surface inundation after Cyclone TAUKTAE in the West Coast of India was mapped using Sentinel-1, C band SAR data at a 10 m resolution. AMSR2 36GHz MPDI based flood index maps were generated for Cyclone Tauktae during 18-19 May 2021. Sentinel-2 multispectral dataset were analysed to understand the changes in the turbidity due to cyclone.

Remote sensing based data analysis was carried out to study the upwelling and impact of cyclone on Ocean biological productivity in Saurashtra coast using OCM-2 data. It was observed that upwelling velocity during cyclone Tauktae was ~5 m/day and dropped to less than 1 m/day in the post landfall week. SST data analysis showed decrease of up to 2-3 °C. A localized patch of enhanced chlorophyll concentration was observed near coastal regions of Gujarat and northern Maharashtra in daily OCM-2 imagery. Thermocline displacement of up to 20 m was observed along cyclone track.

The damage to agricultural and horticulture crops due to cyclone Tauktae was assessed in the coastal regions of Gujarat using microwave and optical sensors data by four anomaly

indices i.e. mean NDVI anomaly, NDVI difference, Standard Score and Vegetation Condition Index (VCI). During a catastrophic event like cyclone, this kind of analysis provide a very useful quicker damage assessment and contingency planning subject to frequent (1-3 days) availability and on-line accessibility of Analysis-Ready-Data (ARD) in optical bands and SAR from very high resolution (1-5m) satellites.

To assess the damage in forest region due to Tauktae cyclone in Gir protected area, a detailed study has been carried out using microwave and optical sensor data and presented in this report. It was found that Tauktae cyclone affected 30% (441 sq. km) of the Gir protected area with moderate to severe impacts.

Table of Contents

1.	PREDICTION AND MONITORING OF CYCLONE	- 1 -
1.1	INTRODUCTION	2
1.1.1	<i>Brief overview of TC TAUKTAE.....</i>	2
1.2	CYCLOGENESIS PREDICTION.....	4
1.2.1	<i>Prediction of cyclogenesis using Genesis Potential Parameter</i>	4
1.2.1	<i>Prediction of cyclogenesis using Scatterometer Data</i>	7
1.3	CYCLONE TRACK AND INTENSITY PREDICTION	9
1.3.1	<i>Real-time track prediction using SAC-Lagrangian Advection Model</i>	9
1.3.2	<i>Track error analysis of Lagrangian Advection Model.....</i>	10
1.3.3	<i>Cyclone Intensity Prediction.....</i>	14
1.3.4	<i>Error analysis of the intensity prediction by HWRF model.....</i>	16
1.4	SHIP AVOIDANCE REGION ADVISORIES	17
1.5	ANALYSIS OF INSAT-3D AND 3DR OBSERVATIONS OVER TC	18
1.5.1	<i>Cyclone structure observations using INSAT3D satellite data.....</i>	19
1.5.2	<i>Cyclone Geo-location.....</i>	20
1.5.3	<i>Cyclone Intensity estimation using ADT with INSAT-3D data</i>	21
1.6	TROPICAL CYCLONE OBSERVED BY INSAT-3DR RAPID SCAN DATA.....	22
1.7	SMAP SATELLITE OBSERVATION OVER TC TAUKTAE.....	24
1.8	FORECAST DISSEMINATION THROUGH WEB PORTAL SCORPIO/MOSDAC	25
1.9	COVERAGE OF CYCLONE TAUKTAE BY MEDIA	26
1.10	CONCLUSIONS	27
	REFERENCES	27
2.	OBSERVING OCEAN CONDITIONS PRIOR AND POST CYCLONE USING SATELLITE AND IN-SITU DATA	29
2.1	INTRODUCTION	30
2.1.1	<i>Cyclone Tauktae</i>	31
2.2	DATA AND MODEL USED	31
2.2.1	<i>Satellite Data</i>	31
2.2.2	<i>Numerical Model</i>	32
2.3	RESULTS AND DISCUSSION	34
2.4	CONCLUSION	39
	REFERENCES	40

3.	RAINFALL ESTIMATION OVER TROPICAL CYCLONE	42
3.1	INTRODUCTION	43
3.2	H-E RETRIEVAL TECHNIQUE	44
3.3	H-E RAIN DURING TROPICAL CYCLONE TAUKTAE	45
3.4	VALIDATION OF H-E RAINFALL	46
3.4.1	<i>IMD surface rainfall observation</i>	46
3.4.2	<i>GPM-IMERG rainfall products</i>	49
3.5	CONCLUSION	49
	REFERENCES	50
4.	ASSESSMENT OF SURFACE INUNDATION AND CHANGES IN WATER TURBIDITY ASSOCIATED WITH CYCLONE	51
4.1	INTRODUCTION	52
4.2	DATA USED	53
4.3	ANALYSIS OF CYCLONE INDUCED FLOODING USING HYDROLOGICAL MODELLING.....	53
4.4	SURFACE INUNDATION MAPPING USING SAR	55
4.5	SURFACE INUNDATION MAPPING USING MICROWAVE RADIOMETRY	56
4.6	IMPACT ASSESSMENT OF WATER QUALITY USING OPTICAL DATASET:.....	57
4.7	CONCLUSION	58
	REFERENCES	59
5.	IMPACT OF CYCLONE ON COASTAL-OCEAN BIOLOGICAL PRODUCTIVITY	60
5.1	INTRODUCTION	61
5.2	DATA USED	61
5.3	METHODOLOGY	62
5.4	RESULTS	63
5.4.1	<i>Chlorophyll from Ocean Color Monitor (OCM-2) imagery before and after cyclone</i>	66
5.5	DISCUSSION	67
5.6	CONCLUSION	68
	REFERENCES	68
6.	DAMAGE ASSESSMENT OF AGRICULTURAL AND HORTICULTURAL CROPS USING OPTI-SAR DATA OVER SAURASHTRA REGION OF GUJARAT CAUSED BY CYCLONE	70

6.1	INTRODUCTION	71
6.2	STUDY AREA AND DATASET.....	72
6.3	METHODOLOGY	73
	<i>6.3.1. Generation of anomaly indicators using only-optical data</i>	73
	<i>6.3.2. Development of damage detection protocol using only-SAR data.....</i>	74
6.4	RESULTS AND DISCUSSION:	76
	<i>6.4.1. Damage detection.....</i>	76
6.5	CONCLUSIONS	90
	REFERENCES	91
7.	DAMAGE ASSESSMENT OF GIR FOREST AREA IN GUJARAT	93
7.1	INTRODUCTION	94
7.2	MATERIALS AND METHODS	95
	<i>7.2.1 Study Area</i>	95
	<i>7.2.2 Data-used</i>	97
	<i>7.2.3 Methodology</i>	98
7.3	RESULTS AND DISCUSSION	100
7.3	CONCLUSIONS	105
	REFERENCES	105

1. Prediction and Monitoring of cyclone

Neeru Jaiswal, Shivani Shah and A K Varma

1.1 Introduction

Tropical cyclones (TCs) are one of the most violent weather manifestations that include number of different hazards like storm surge, flooding, extreme winds, torrential rains, thunderstorms, and lightening and cause devastation along the coastal regions. Each year tremendous economy losses and deaths are caused by the TCs throughout the world. To overcome/reduce such losses, the accurate prediction of TC formation, is required so that precautionary measures can be taken. TC formation involves interaction between synoptic scale as well as the mesoscale process. The North Indian Ocean (NIO) is a potentially energetic region for the development of TCs. Prediction of the development of any cyclonic system in the NIO is being done as a regular exercise at Space Applications Centre, Ahmedabad (SAC-ISRO) using the indigenously developed algorithms. Once the system is developed, prediction of its track and intensity are generated in real-time and disseminated through a web based application “Satellite based cyclone observation and real-time prediction over Indian ocean” (SCORPIO) (<https://mosdac.gov.in/scorpio>), available on the MOSDAC portal (<https://mosdac.gov.in>). The similar exercise was performed during the formation of TC Tauktae, and discussed in the present report.

1.1.1 Brief overview of TC TAUKTAE

Tropical cyclone Tauktae was the first tropical cyclone of the year 2021 that formed in the North Indian Ocean. It was the second extremely severe cyclonic storm to hit Gujarat in the last 23 years. It was developed from a low pressure area, formed over southeast Arabian Sea & adjoining Lakshadweep area in the morning (0830 hrs IST/ 0300 UTC) of 13th May 2021. Under favorable environmental conditions, it turned into a depression over Lakshadweep area in the morning (0830 hrs IST) of 14th May, 2021. It intensified into a deep depression over Lakshadweep area and adjoining southeast & eastcentral Arabian Sea in the same afternoon (1430 hrs IST/ 0900 UTC of 14th May) and into cyclonic storm “TAUKTAE” in the same midnight (2330 hrs IST/1800 UTC) over the same region. It continued moving nearly northwards, and intensified into a very severe cyclonic storm over eastcentral Arabian Sea in the early hours (0230 hrs IST/2100 UTC) of 16th May. It gradually started moving north-northwestwards and intensified rapidly into an extremely severe cyclonic storm in the early hours (0530 hrs IST/0000 UTC) of 17th May. Thereafter, it entered marginally unfavourable environment, weakened gradually and crossed

Saurashtra coast near latitude 20.8°N and longitude 71.1°E, close to northeast of Diu (about 20 km northeast of Diu) during 2000-2300 hours IST of 17th May, 2021 with maximum sustained wind speed of 160-170 kmph gusting to 185 kmph (IMD Report, 2021). The best track of TC provided by India Meteorological Department (IMD), Delhi with its intensity categories is shown in Fig.1.1. The IMD classification of cyclone categories is given in Table 1.1.

Table 1.1: IMD classification of categories of cyclonic system

System	Associated wind speed (knots)
Low pressure area	<17
Depression	17-27
Deep Depression	28-33
Cyclonic Storm	34-47
Severe Cyclonic Storm (SCS)	48-63
Very SCS (VSCS)	64-85
Extremely SCS (ESCS)	86-119
Super Cyclonic Storm(SuC)	>119

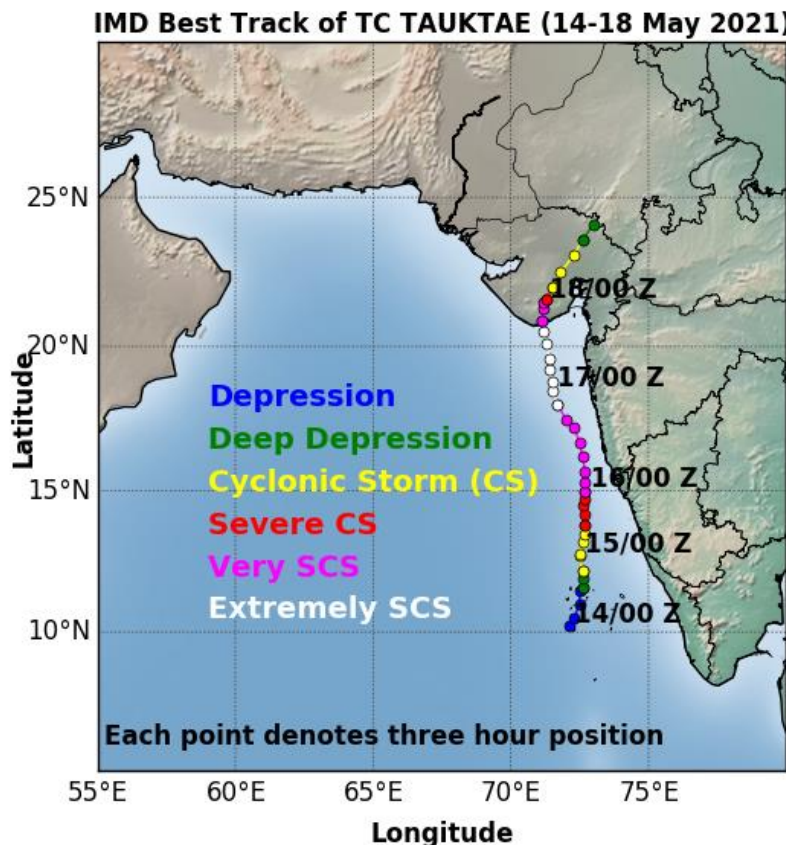


Figure 1.1: Three-hourly IMD best track of TC Tauktae with its intensity.

Cyclone name “Tauktae”, was given by Oman. As per global convention, the thirteen countries that make up the Indian Ocean Region—Bangladesh, India, Iran, Maldives, Myanmar, Oman, Pakistan, Qatar, Saudi Arabia, Sri Lanka, Thailand, United Arab Emirates, Yemen—have drawn up a list of names for tropical cyclones, which are assigned serially with the alphabetic order of the nation’s name. The word “TAUKTAE” means Gecko, a highly vocal lizard.

1.2 Cyclogenesis Prediction

The prediction of tropical cyclogenesis (TCG) of cyclonic systems that develop in the NIO is being done at SAC using in-house developed technique. This technique is based on wind pattern matching of the scatterometer derived surface wind observations and provides 1-4 days advance TCG prediction (Jaiswal and Kishtawal, 2011; 2013). During cyclone active months of the NIO i.e. April-June and October-December, the cyclogenesis prediction technique is regularly run to detect the earliest signatures of any possibility of cyclonic activity in the Bay of Bengal (BoB) and Arabian Sea (ARB) region. Due to unavailability of SCATSAT-1 satellite data, this technique could not be run and the cyclogenesis of TC TAUKTAE could not be predicted. The model forecasts can be examined to investigate the signatures of tropical cyclogenesis. Advanced prediction of tropical cyclogenesis based on model forecasted parameters is discussed in the next section.

1.2.1 Prediction of cyclogenesis using Genesis Potential Parameter

A cyclone genesis parameter, termed the genesis potential parameter (GPP), for the Indian Sea was proposed by Kotal et al. 2019. The parameter is defined as the product of four variables, namely vorticity at 850 hPa, middle tropospheric relative humidity, middle tropospheric instability, and the inverse of vertical wind shear. The variables are calculated using the National Centers for Environmental Prediction (NCEP), USA, reanalysis data, averaged within a circle of 2.5° radius around the centre of cyclonic system. The GPP, at early development stage of a cyclonic storm provides a useful predictive signal for intensification of the system.

$$GPP = \begin{cases} \frac{\zeta_{850} \times M \times I}{S} & \text{if } \zeta_{850} > 0, M > 0 \\ 0 & \text{otherwise} \end{cases} \quad (1)$$

$$M = \frac{(RH - 40)}{30}$$

Where, ζ_{850} is low level relative vorticity (at 850 hPa in 10^{-5} s^{-1}), S is vertical wind shear (between 200 and 850 hPa in s^{-1}), RH is the mean relative humidity (between 700 and 500 hPa) and I is middle-tropospheric instability (temperature difference between 850 hPa and 500 hPa). All the variables are estimated by computing the grided values and averaging it over an area of radius 2.5° . The maximum value of GPP in the NIO region was compared to the pre-determined threshold value for cyclogenesis. The threshold value to detect cyclogenesis was determined by maximizing the probability of detection (POD) and minimizing the false alarm ratio (FAR). POD is the ratio of the total number of detected TC formation and total number of formed cases and FAR is the ratio of the total number of predicted TC formation that does not occur (develop) and total number of non-developed cases. For threshold determination, GFS analysis fields, during nine TCs formed in the NIO during the period 2009-10 and 100 non-developed cases were analyzed. The GPP was estimated using the 850 hPa wind fields, deep vertical wind shear (850-200 hPa), warm core (850-500 hPa), and mean relative humidity (700-500 hPa). The TC formation has been determined by varying the different threshold values of GPP, which are obtained by minimum of the maximum values of GPP using the GFS analysis fields on the day of TC formation of all cyclones. These thresholds have also been used to predict the TCG by the GFS analysis fields of 100 non-developed cases. The optimum threshold values for GPP was found as “2” which is then used to identify the TCG in GFS forecasted fields (Singh et al., 2013). The GPP value was computed in NIO with the GFS data prior to the formation of TC TAUKTAE to detect its cyclogenesis signatures. The spatial plots of GPP with the required parameters used in GPP computations (as given in Eq. 1) are shown in Fig. 1.2 for 00 UTC and 12 UTC forecasts of GFS on 20, 21 and 22 May 2021. The maximum GPP values for all analyzed forecasts are summarized in Table 1.2.

Table 1.2: Maximum GPP computed in Arabian Sea before formation of TC TAUKTAE

Date	00 UTC 09 MAY	00 UTC 10 MAY	00 UTC 11 MAY	00 UTC 12 MAY	00 UTC 13 MAY	00 UTC 14 MAY
Maximum GPP	7.84	4.07	9.37	6.01	6.80	14.45

The values of GPP (>5.0) shows the strengthening of cyclogenesis conditions.

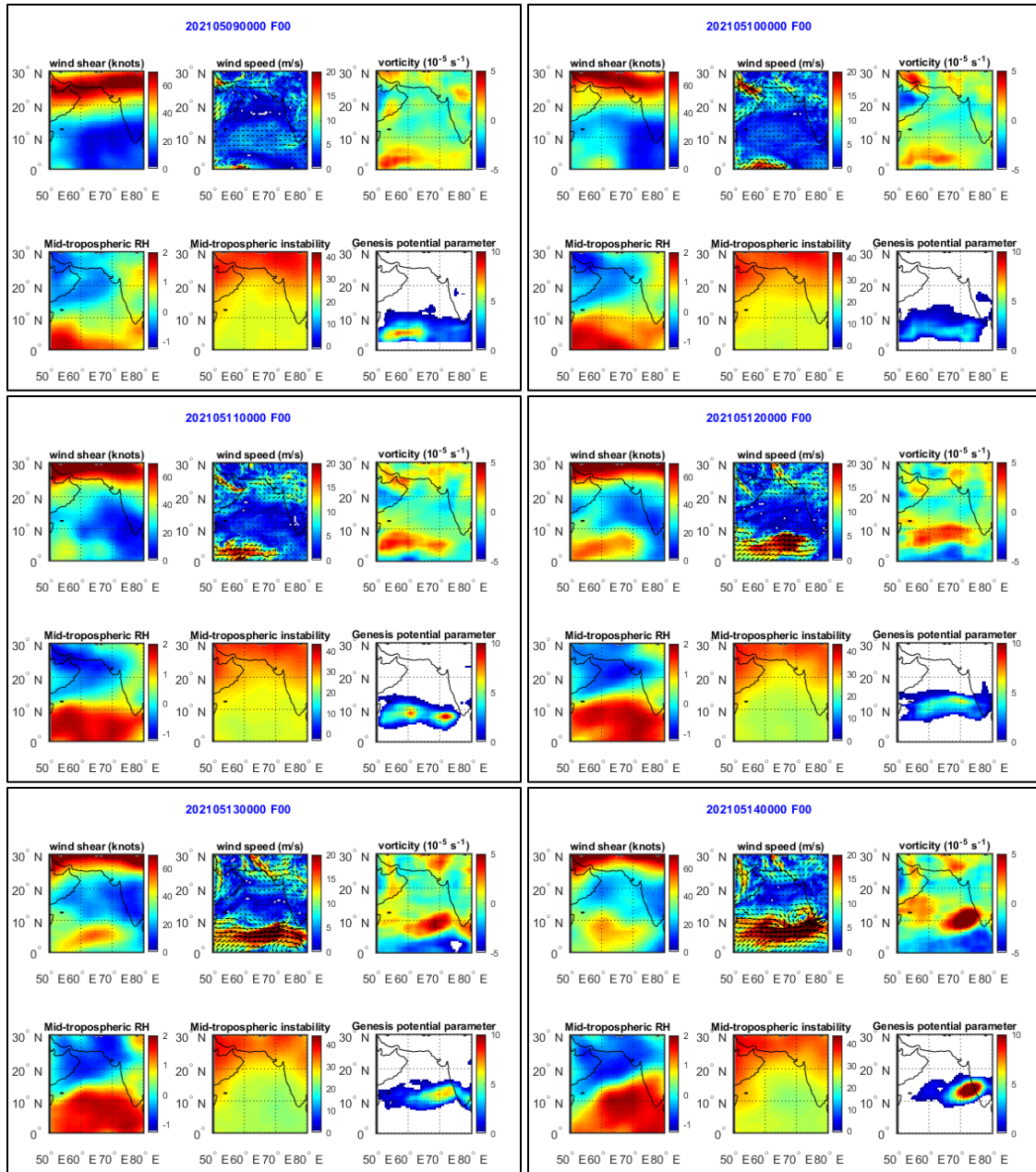


Figure 1.2: Spatial plot of cyclogenesis parameters and GPP values for 00 UTC of 9, 10, 11, 12, 13 and 14 May 2021.

1.2.1 Prediction of cyclogenesis using Scatterometer Data

A technique has been developed at SAC for cyclogenesis prediction using scatterometer data. This technique is based on the premise that there is some similarity between the low-level wind pattern of the developing systems, which can be detected and used to identify the developing and non-developing low-pressure systems. In this technique, the real-time observed winds are matched to the wind patterns archived within the database of all developed systems in the past and the most similar wind pattern was selected. This similarity was quantified using a matching index as given in the following expression.

$$cc = \frac{\frac{1}{N} \sum_{i=1}^N (A_i - \bar{A}) * (B_i - \bar{B})}{\sqrt{\frac{1}{N} \sum_i^N |A_i - \bar{A}|^2} \times \sqrt{\frac{1}{N} \sum_i^N |B_i - \bar{B}|^2}} \quad (1)$$

where \bar{A} and \bar{B} represents the mean value of the complex vectors A and B respectively. N is the dimension of vector A (or B) and A and B are the complex numbers formed using the wind vectors [*for example $A = (u+iv)$*].

If the matching index value is found to be greater or equal to some pre-defined threshold values (0.6 for NIO), the cyclogenesis is predicted. The scatterometer data of QuikSCAT and OSCAT were used in the development and testing of the algorithm (Jaiswal and Kishtawal, 2011; 2013). During the years 2010-13, OSCAT data was used for the real-time cyclogenesis prediction using the above-discussed approach. In the year 2014 the OSCAT stopped working and thereafter the surface wind observations from RAPIDSCAT were being used in the real-time prediction of TCG in NIO at SAC. SCATSAT1 (Scatterometer Satellite1) satellite was launched on 26th September, 2016 to provide weather forecasting, cyclone prediction, and tracking services to India. The SCATSAT-1 data was being utilized operationally in the real-time for TCG prediction. Recently this satellite stopped working and due to unavailability of any other satellite data with such wider swath, the above technique could not be used for the TCG prediction. However, the passes of NASA scatterometer ASCAT onboard metopA, metopB and metopC were processed to get the signature of low-level wind circulation. Due to the narrow swath of ASCAT (unlike OSCAT, SCATSAT-1 and QuickSCAT), there is a least possibility to capture the complete

low-level wind circulation in a single pass, thus the above discussed technique cannot be applied over ASCAT dataset. The earliest signatures of low-level circulation were found on all the three ASCAT passes of May 13. Wind vectors overlaid on the wind speed (m/s) by the passes of ASCAT from metopA, metopB during the genesis of TC TAUKTAE are shown in the Fig. 1.3. The strong partial wind circulation can be seen in all these passes, which may indicate to the development of this circulation into a tropical cyclone.

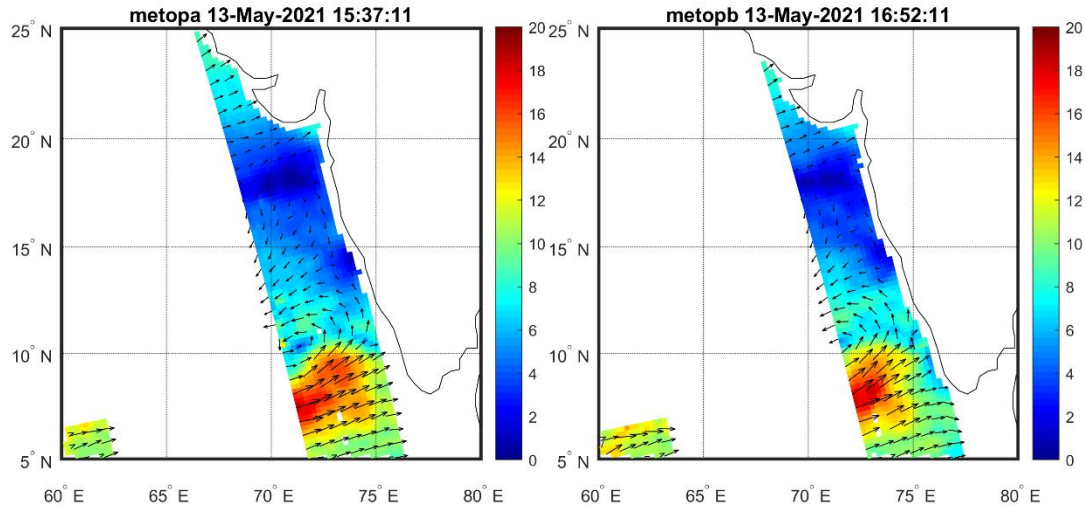


Figure 1.3: Wind vectors overlaid on the wind speed (m/s) by the passes of ASCAT from metopA (left) and metopB (right) during the genesis of TC Tauktae.

1.3 Cyclone Track and Intensity Prediction

A system has been developed in SAC for monitoring, analysis and prediction of tropical cyclones over the Indian Ocean. The results of analysis and prediction are disseminated through SCORPIO web-portal linked to MOSDAC server. After the formation of tropical cyclone in the Indian Ocean, track predictions are carried out using three different models.

(a) Indigenously developed Lagrangian advection cyclone track prediction model (LAGAM), (b) Hurricane Weather Research and Forecasting (HWRF), a coupled land-ocean-atmosphere model customized for Indian Ocean region, and (c) WRF model used for daily real-time predictions of all-India weather at 5 km resolution. The HWRF model is used for prediction of tropical cyclone intensity. The track and intensity prediction of cyclone TAUKTAE was initiated on MAY 14, 2021 and were continued until the cyclone made landfall. Real-time track prediction of cyclone Tauktae by SAC-Lagrangian advection Model, WRF and HWRF models are discussed in the following sections.

1.3.1 Real-time track prediction using SAC-Lagrangian Advection Model

SAC-Lagrangian Advection model is dynamical framework based computationally efficient model (Singh et al, 2011; 2012). It requires the high resolution $0.5^{\circ} \times 0.5^{\circ}$ forecasted atmospheric winds and temperature from Global forecast System (GFS), which is global numerical weather prediction model, run by NOAA, and the initial position of cyclone, which is obtained from Joint Typhoon Warning Centre (JTWC) for track prediction. Cyclone track prediction is provided using this model upto 96 hour with 6 hour interval. As a first step, the steering flow has been computed for every 6-hour forecast interval up to 96 hours, using the analysis as well as forecast wind fields data at 21 pressure levels (100-1000 mb) by the weighted average scheme. The weight for each level was assigned by estimating the potential vorticity (PV) which is adapted from the study by Hoover et al., 2006. Then a cyclonic vortex is removed using a synthetic cyclone, which is constructed by using the vorticity equation (Chan and Williams, 1987):

$$\frac{\partial \zeta}{\partial t} + V \cdot \nabla (\zeta + f) = 0$$

Where ζ is the vorticity and $f = \beta y + f_0$. Here y denotes latitudinal displacement, f_0 is the value of coriolis parameter at $y = 0$ and β is the rate of change of coriolis parameter with

latitude. In case of axisymmetric vortex, the velocity is calculated using the equation (Chan and Williams, 1987):

$$V(r) = V_m \left(\frac{r}{r_m} \right) \exp \left[\frac{1}{b} \left(1 - \left(\frac{r}{r_m} \right)^b \right) \right]$$

Where V_m and r_m denote the maximum value of tangential velocity and the radius at which V_m occurs, respectively. This synthetic cyclone was used to remove the existing cyclonic wind fields present in the steering flow to achieve the residual steering current. To avoid the discontinuity of wind fields due to removal of cyclonic circulation, tapered weights $W(k)$ are used for generation of residual flow fields. Now, resulting steering flow that is obtained after removing the cyclonic vortex from steering flow is used in Lagrangian Advection Model to forecast cyclone track. The computation for the trajectory of cyclone (or cyclone track) is initiated by interpolating the steering wind from model grid points to the initial location of cyclone (Brand, 1981). The real time predicted tracks for cyclone TAUKTAE have been shown in Fig. 1.4.

1.3.2 Track error analysis of Lagrangian Advection Model

The real time predicted tracks of cyclone by SAC-Lagrangian Advection Model for different initial times have been shown with the observed track of IMD in Fig. 1.5. The track forecast error for all the forecasts were computed w.r.t IMD observed track positions. The error values have been summarized in Table 1.3. IMD reported the TC crossed Saurashtra coast about 20 km northeast of Diu, near Lat.20.8°N and Long. 71.1°E during 1530-1730 UTC 17 May 2021 with maximum sustained wind speed of 90 knots gusting to 100 knots. The landfall position error for all the forecasts have been computed and reported in the Table 1.4. For 24-hour lead prediction, the landfall position error of Lagrangian advection model was found as ~31 km and landfall time error was ~1 hour.

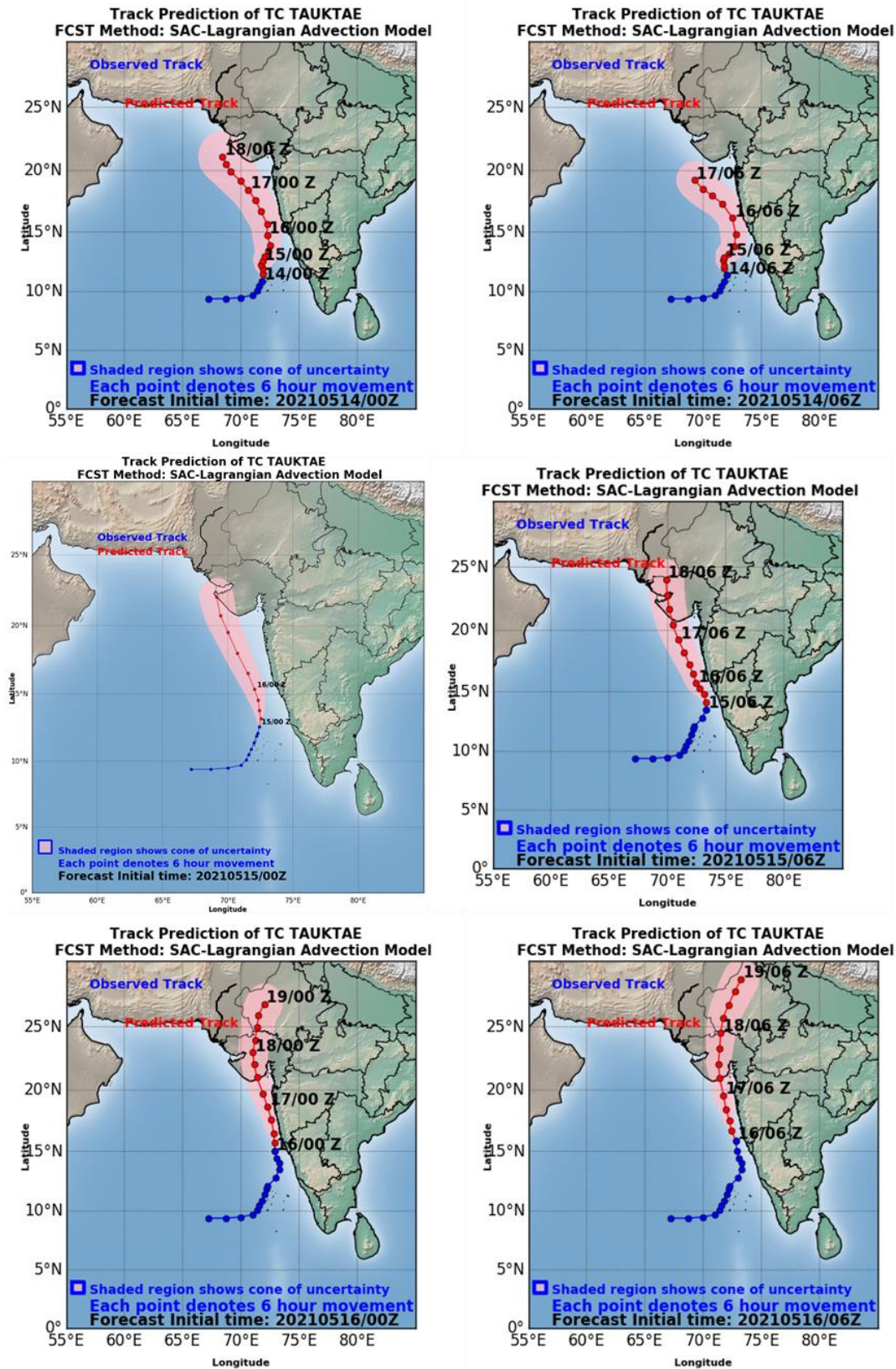


Figure 1.4: Track prediction of cyclone TAUKTAE for different initial conditions by SAC-Lagrangian advection model (Real- time generated products).

Tropical cyclone Tauktae

Real-Time Track Prediction of TC TAUKTAE (15-17 May 2021)
FCST Method: SAC-LAGAM Model

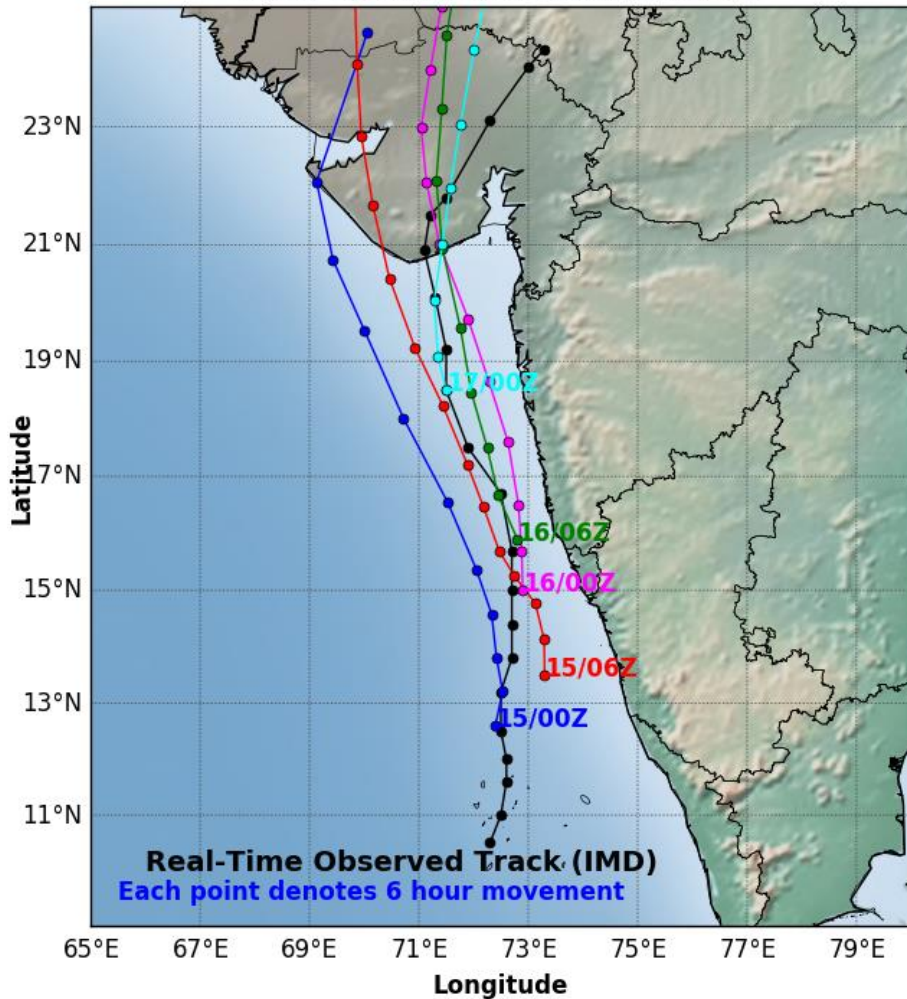


Figure 1.5: IMD best track and real-time predicted track of cyclone TAUKTAE by SAC-Lagrangian advection model for different initial time (15-MAY-00Z, 15 MAY-06Z, 16 MAY-00Z, 16 MAY-06 Z, 17 MAY-00Z).

Table 1.3: Track Forecast Error (km) of SAC-Lagrangian Advection track prediction Model w.r.t IMD observed track positions

FCST time	Initial	Track Error (km) for different Forecast Lead time				
		6	12	24	36	48
00 UTC 15 MAY		3.43	30.26	80.98	238.55	330.21
06 UTC 15 MAY		73.48	61.92	24.65	33.38	59.94
00 UTC 16 MAY		19.30	40.11	83.89	101.53	166.50
06 UTC 16 MAY		6.28	37.12	49.36	134.27	303.56
00 UTC 17 MAY		20.65	6.99	64.74	135.58	214.96
Mean Error		24.63	35.28	60.72	128.66	215.03

Table 1.4: Landfall Prediction Error (km) of SAC-Lagrangian advection track prediction Model for TC TAUKTAE.

Forecast Time/Date		Landfall Time/Date/Location				Landfall Error	
Date	Time	Date	Time	Long	Lat	Location Error (km)	Time Error (Hrs)
15MAY	00 UTC	17MAY	06 UTC	69.15	22.12	249.53	-10 hour
15MAY	06 UTC	17MAY	14 UTC	70.34	20.92	80.09	-2 hour
16MAY	00 UTC	17MAY	11 UTC	71.44	20.87	36.18	-5 hour
16MAY	06 UTC	17MAY	12 UTC	71.44	20.87	36.18	-4 hour
17MAY	00 UTC	17MAY	18 UTC	71.40	20.83	31.36	+1 hour

Cyclone landfall (IMD): Latitude: 20.8, Longitude 71.1 between 1530 UTC and 1730 UTC 17 MAY, 2021.

1.3.3 Cyclone Intensity Prediction

For cyclone intensity prediction numerical weather prediction model WRF and HWRF are utilized. WRF model is regularly run at SAC, its output are analyzed to get cyclone related parameters.

The HWRF model is a primitive-equation, non-hydrostatic, coupled atmosphere-ocean model with an atmospheric component that employs the Non-hydrostatic Mesoscale Model (NMM) dynamic core of the WRF model (WRF-NMM), with a parent and two nest domains (Biswas et al. 2018). The parent domain covers roughly 77.2° x 77.2° on a rotated latitude/longitude E-staggered grid. The location of the parent domain is determined based on the initial position of the storm provided by NHC/Joint Typhoon Warning Center (JTWC). The middle nest domain, of about 17.8° x 17.8° , and the inner nest domain, of about 5.9° x 5.9° , move along with the storm using two-way interactive nesting. The stationary parent domain has a grid spacing of 0.099° (about 13.5 km) while the middle nest grid spacing is 0.033° (about 4.5 km) and the inner nest grid spacing is 0.011° (about 1.5 km). The dynamic time steps are 30, 10, and 3.33 s, respectively, for the parent, middle nest, and inner nest domains. Starting 2018, all the basins have their model top at 10 hPa and 75 levels are used.

HWRF v4.0a includes a scale-aware Arakawa-Schubert scheme for cumulus parameterization and a Ferrier-Aligo cloud microphysics package for explicit moist physics. The Global Forecasting System (GFS) Eddy-diffusivity Mass flux scheme is used for the planetary boundary layer, along with the modified Geophysical Fluid Dynamics Laboratory (GFDL) surface layer scheme. The Monin-Obukhov scheme is used for surface flux calculations, which employs an improved air-sea momentum flux parameterization in strong wind conditions. The Noah land surface model is used to represent the land surface for calculating the surface fluxes and the amount of upwelling radiation at the lower atmospheric model boundary. Radiation effects are evaluated by the Rapid Radiative Transfer Model for General Circulation Models (RRTMG) scheme, which includes diurnal variations and interactive effects of clouds. The HWRF physics operational suite also includes parameterization of dissipative heating. The time integration is performed with a forward-backward scheme for fast waves, an implicit scheme for vertically propagating sound waves, and the Adams-Bashforth scheme for horizontal advection and for the Coriolis force. In the vertical, the hybrid pressure-sigma coordinate is used.

The NCEP Global Forecast System (GFS) analysis is used to generate the initial conditions (ICs) for the hurricane model parent domain in the operational configuration.

Numerical Experiments and Data Used

The HWRF4.0a model, used in the present study, is obtained from the NCEP website www.dtcenter.org. The model is installed and evaluated for its default configuration for NIO tropical cyclones. The present study summarizes the results of TC BULBUL for three different initial conditions i.e. 00 UTC 15, 16 and 17 MAY. The NCEP Global Forecast System (GFS) analysis and forecasts ($0.25^0 \times 0.25^0$) have been used to provide the initial and lateral boundary conditions. All the three experiments were performed in the uncoupled ocean mode and without the data assimilation module.

The intensity of simulated cyclone from different experiments is evaluated in terms of the maximum sustained wind speed (MSW). The real time intensity prediction of cyclone for all initial conditions (00 UTC 15-17 MAY) was provided on the SCORPIO web-portal (Fig. 1.6).

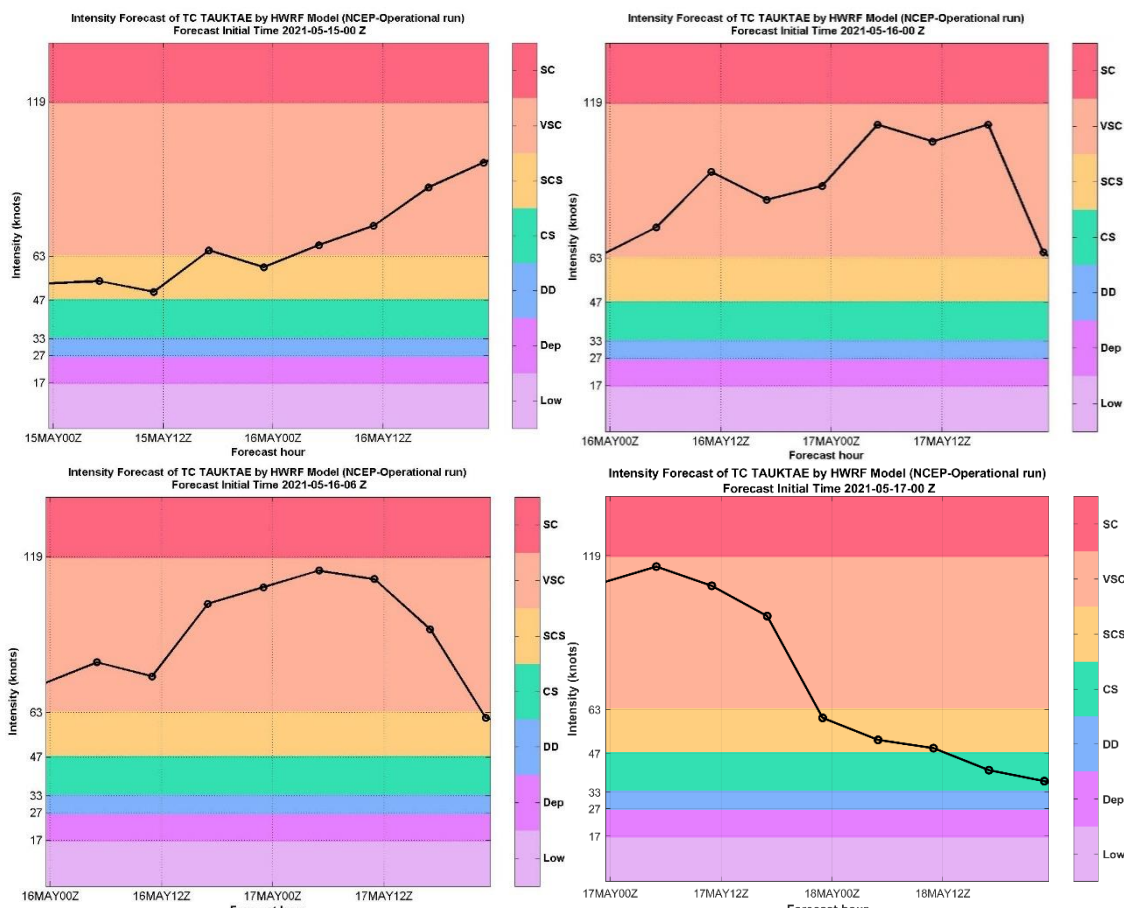


Figure 1.6: Real time forecast of cyclone intensity by HWRF model.

1.3.4 Error analysis of the intensity prediction by HWRF model

The model simulated intensity of the cyclone Tauktae for different initial conditions are presented in Fig. 1.7 along with best track intensity estimates of IMD. The error in model-simulated intensity (MSW) with respect to the IMD estimated MSW for all initial conditions are presented in Fig. 1.8. The results suggest that the model predicted the intensity very well on 00 UTC 15 MAY; however, the predictions on 00 UTC 16 and 17 May are over estimated.

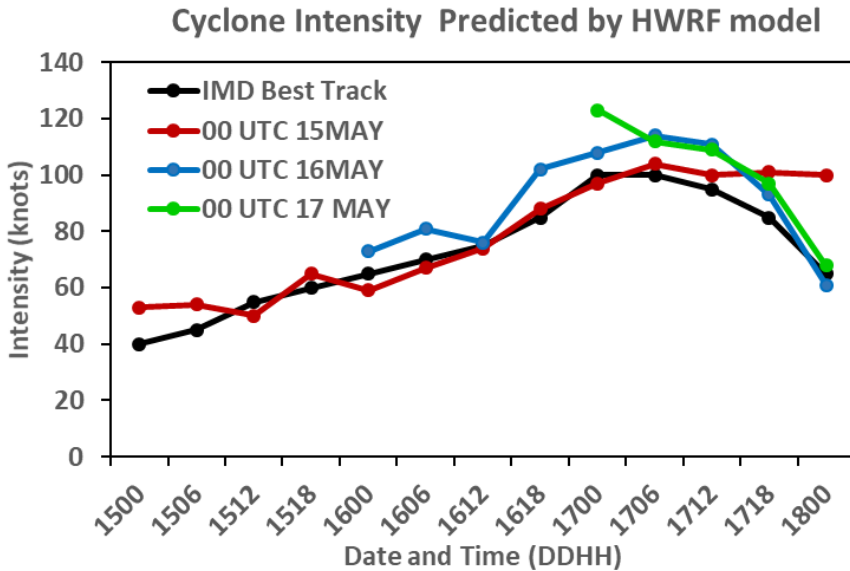


Figure 1.7: Cyclone intensity simulated by HWRF model for different initial conditions with IMD estimates.

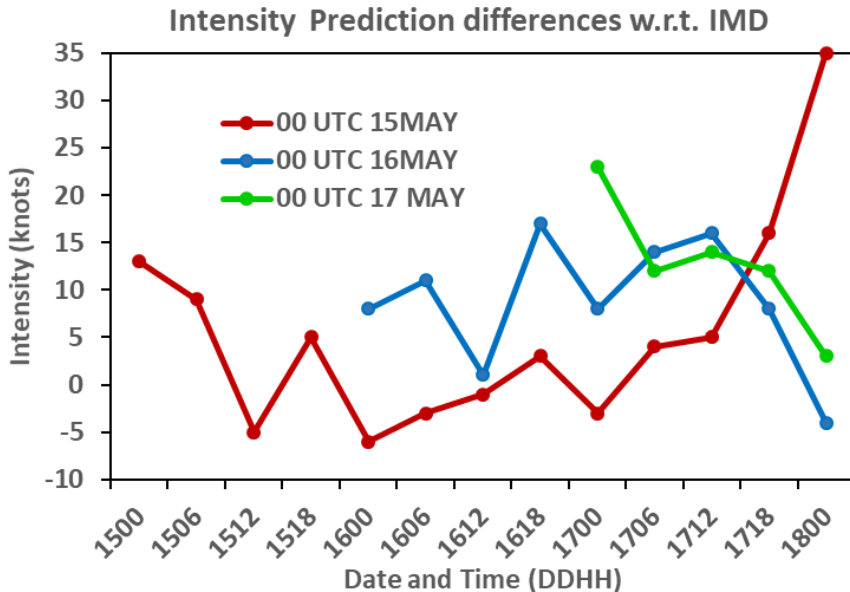


Figure 1.8: Cyclone intensity error by HWRF model w.r.t. JTWC observed intensity estimates for different initial conditions.

1.4 Ship Avoidance Region Advisories

For vessels at sea, avoiding the 34-knot wind field of a tropical cyclone is paramount. Based on operational HWRF model, 34-knot wind radial distances the graphical inputs of ship avoidance region were generated for cyclone and disseminated through SCORPIO server. The real-time generated ship avoidance region advisory products are shown in Fig. 1.9.

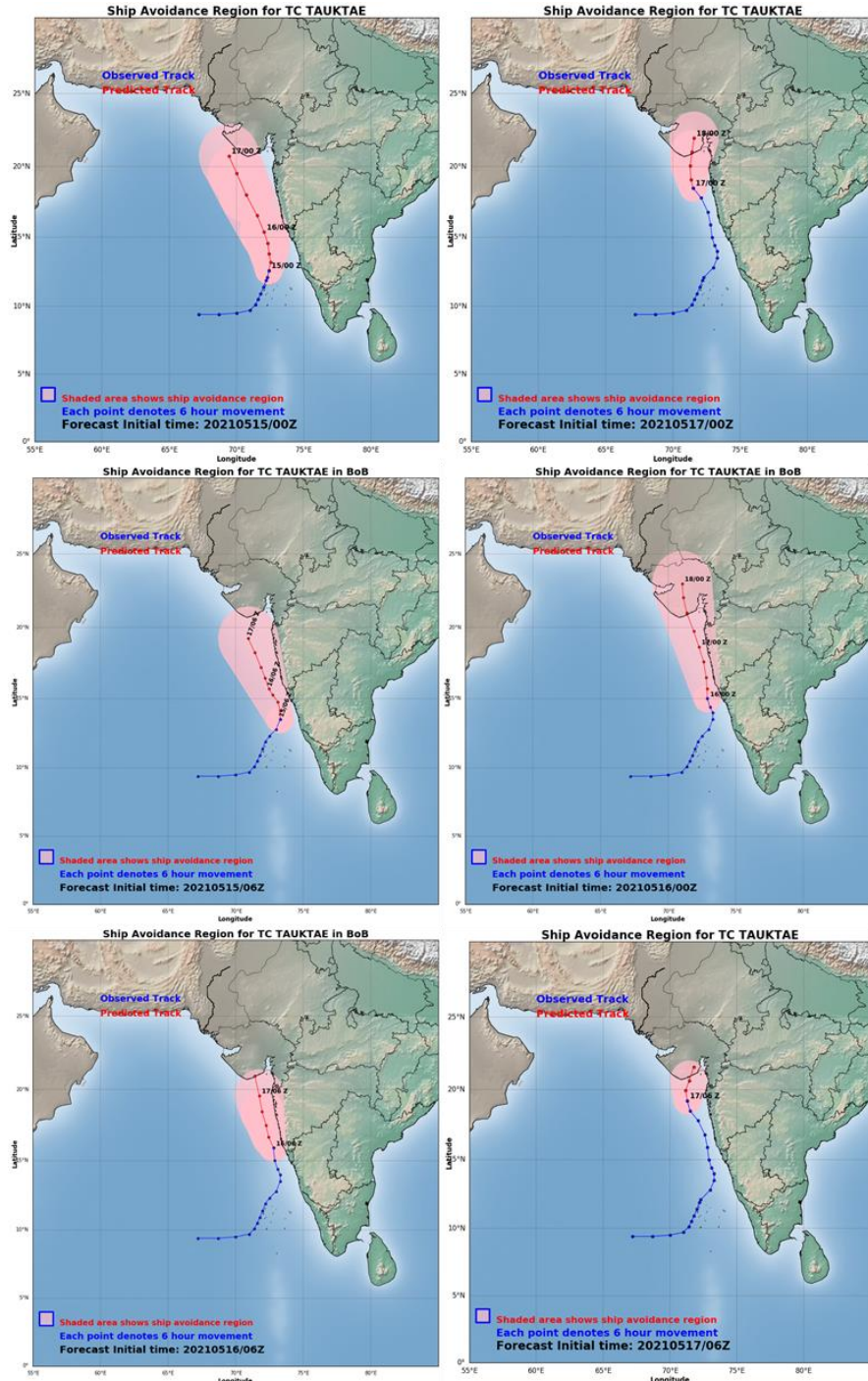


Figure 1.9: Ship avoidance region forecast advisories generated at 00, 06 UTC of 15-17 MAY

1.5 Analysis of INSAT-3D and 3DR observations over TC

India's two meteorological geostationary satellites viz., INSAT3D and INSAT3DR provides coverage over India and surrounding regions including the oceans. INSAT-3D/3DR are meteorological satellite of ISRO, an exclusive next generation mission designed for enhanced meteorological observations and monitoring of land and ocean surfaces for weather forecasting and disaster warnings. INSAT-3D and INSAT-3DR both have two meteorological payloads, an Imager (with 6 channels) and a Sounder (with 18 infrared channels and a visible channel for daytime cloud detection). The Imager has capability of taking observations of full earth-disk from geostationary orbit in one visible channel (VIS, 0.55-0.75 μm) and five infrared (IR) channels: Shortwave infrared (SWIR, 1.55-170 μm), Mid-wave infrared (MIR, 3.8-4.0 μm), Water Vapor absorption channel (WV, 6.5-7.1 μm), and two split-window thermal infrared channels (TIR1, 10.2-11.2 μm and TIR2, 11.5 to 12.5 μm). The observations from VIS and SWIR channels are available at 1 km x 1 km ground resolution at nadir, whereas MIR, TIR1, and TIR2 has resolution of 4 km x 4 km. The WV channel has coarser resolution of 8 km x 8 km at nadir. The sub-satellite points of INSAT3D and INSAT3DR are at 82 $^{\circ}$ E and 74 $^{\circ}$ E, respectively. Enhanced resolution and multi-spectral capability of INSAT-3D/3DR imager and sounder instruments provide unique opportunity to observe the development and intensification of tropical cyclones. One of the essential ingredients to the intensification of tropical cyclones is vigorous convection with associated latent-heat release through condensation processes. Identifying and quantifying active convection in geostationary satellite images can be potentially useful to the prediction of cyclone intensification. The coverage of cyclone by TIR-1 and visible channels of INSAT-3D satellite on 0929 UTC 17-MAY-2021 are shown in the Fig. 1.10.

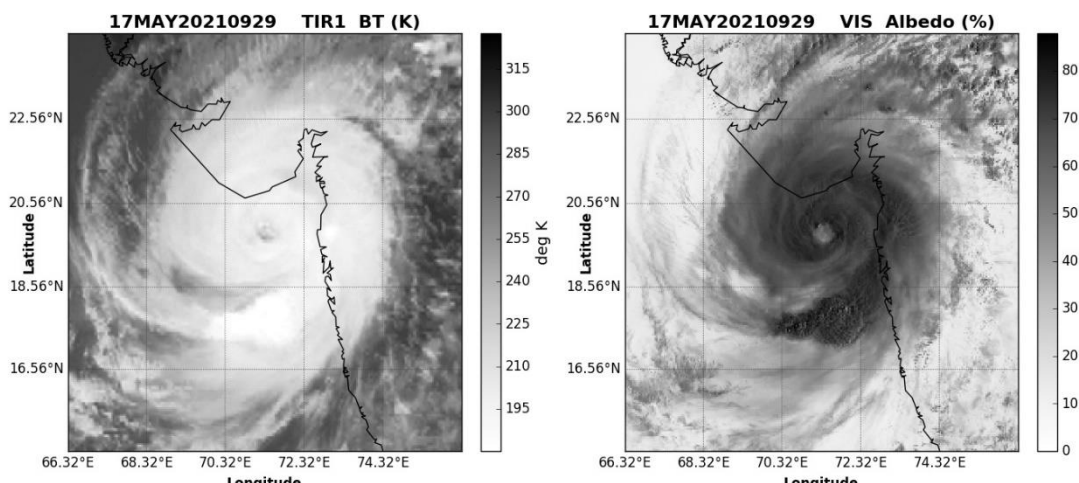


Figure 1.10: Coverage of cyclone TAUKTAE by TIR-1 and visible channels of INSAT-3D satellite on 0930 UTC 17-MAY-2021.

1.5.1 Cyclone structure observations using INSAT3D satellite data

Cyclone structural parameters are estimated using INSAT3D observations from different channels. Cyclone centric products from INSAT-3D imager channels are generated to visualize cyclone structure viz., its center, temperature of eye and its environment. Radius of Maximum Winds (R_{max}) is one of the most critical parameters that determine the tropical cyclone wind structure. This information is often required to assess the area of damage after the landfall of cyclone. The radius of maximum winds is normally very small (~ 30 km) compared to the size of cyclone, but can vary in a large range under specific circumstances. In infrared satellite images, the central region of cyclone is mostly obscured by high level cirrus clouds that cause difficulty in precise identification of R_{max} . High resolution observations from Visible and SWIR channels provide unique opportunity to identify the cloud structure near the center of cyclone. A procedure has been developed to produce cyclone centric products from each half hourly image of INSAT3D satellite. These images are very useful to study the structural changes in the core of tropical cyclone. A sample product generated on 0930 UTC 17 MAY, 2021 have been presented in the Fig. 1.11.

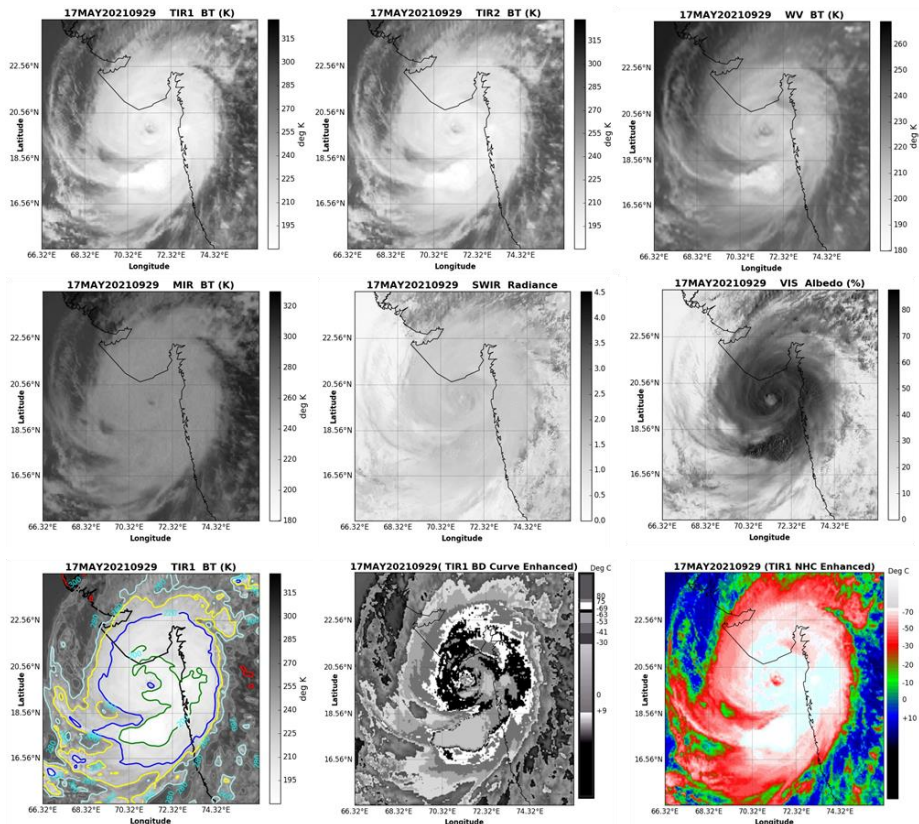


Figure 1.11: Cyclone Centric product generated using INSAT-3D imager channel. The nine panels show (a) TIR1 BT, (b) TIR2 BT, (c) WV BT, (d) MIR BT, (e) Vis Albedo, (f) SWIR radiances, (g) TIR1 BT Contours, (h) TIR1 BT BD enhanced, and (i) TIR1 BT NHC enhanced images.

1.5.2 Cyclone Geo-location

TC Tauktae was continuously observed by the half hourly acquisition of INSAT-3D satellite. In half hourly TIR imageries of INSAT 3D satellite the center location of cyclone was estimated by center determination algorithm developed at SAC. The results were disseminated through SCORPIO web-server. One of the sample products generated in the real-time has been shown in the Fig. 1.12.

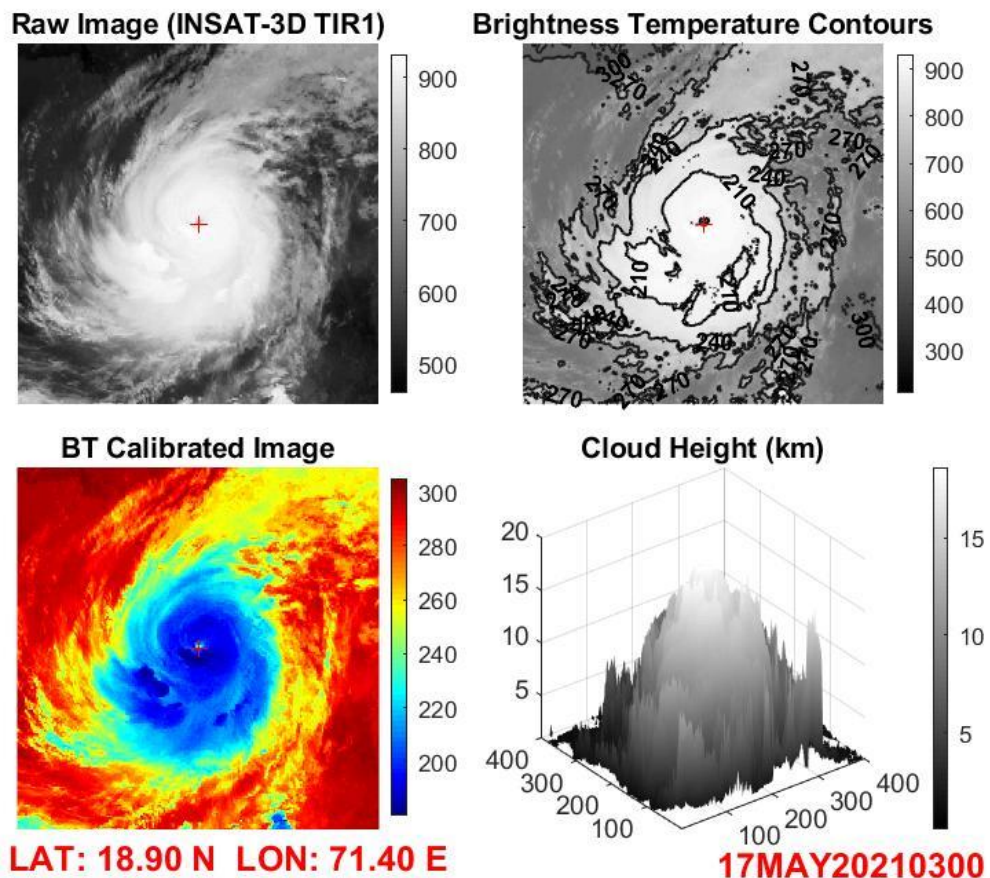


Figure 1.12: Cyclone center estimation using INSAT-3D TIR1 data. The four panels show a) INSAT-3D TIR1 raw image, (b) TIR1 BT contours, (c) BT calibrated image, and (d) cloud height (km).

1.5.3 Cyclone Intensity estimation using ADT with INSAT-3D data

Advanced Dvorak Technique (ADT) was originally developed within the Man computer Interactive Data Access System (McIDAS) architecture. The algorithm utilizes McIDAS library functions and routines to ingest infrared satellite data, display textual and graphical results, read various input data files, and write various output files. The ADT version 8.2.1, software package has been obtained from CIMSS and is installed in the “Non-McIDAS” mode (Jaiswal et al., 2021). The modules to ingest INSAT-3D satellite data in the software (version 8.2.1) are developed at Space applications Center (SAC-Ahmedabad, ISRO). The ADT was run in offline mode to estimate intensity values of TC using INSAT3D satellite data (SAC_ADT). ADT is run operationally for all global cyclones using half-hourly images of geo-stationary satellite images by CIMSS and provided at their web page in the near real time. SAC_ADT values were compared with the operational values of intensity obtained from the ADT run at CIMSS (CIMSS_ADT) and the real-time intensity values provided by IMD (Fig. 1.13). The error analysis were performed and the results shows that intensity of cyclones using INSAT-3D data by ADT are comparable to CIMSS_ADT and the best track estimates. However, there is an overestimation during 06 UTC 16 MAY to 00 UTC 17 MAY. The peak intensity of cyclone Tauktae as observed by IMD (100 knots) was estimated by SAC_ADT and CIMSS_ADT as 129 knots.

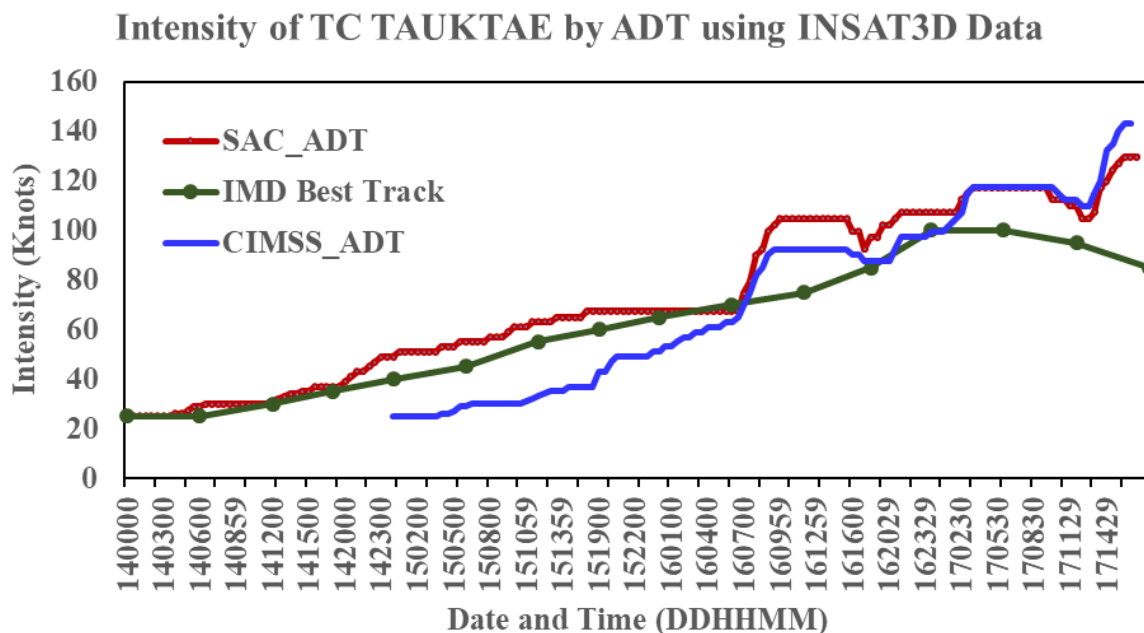


Figure 1.13: Intensity estimated by ADT using INSAT3D satellite data (SAC_ADT), CIMSS operational ADT (CIMSS_ADT) products and real-time observed values of IMD (IMD) during life time of TC.

1.6 Tropical cyclone observed by INSAT-3DR Rapid Scan Data

The rapid scan images from geostationary satellites have been proven to be useful tools in weather applications like the derivation of atmospheric motion winds, analysis of wildfires, convective initiation nowcasting, and identification of overshooting convective cloud tops. These images are useful for monitoring the convective features of storms that evolve on shorter time scales i.e. less than 15 or 30-minutes (Dworak et al. 2012; Cintineo et al. 2013). Several unique signatures have been identified within satellite imagery of severe convective storm tops, which include rapid cloud-top cooling (Cintineo et al. 2013), overshooting tops (Dworak et al. 2012), above-anvil cirrus plumes (Levizzani and Setvák 1996), the cold ring (Setvák et al. 2010) etc.

The Indian geostationary satellite INSAT3DR is being operated in rapid scan operation mode during high impact weather activities like TCs to capture the images in every 4-minutes interval. These satellite observations may be helpful in observing the rapidly changing features over TCs and thus determining its movement, structure and intensity. The atmospheric motion winds generated using rapid scan images during tropical cyclone time shows potential for providing very good quality winds information over Indian Ocean by increasing the amount of wind data availability and by capturing atmospheric movement that are too short-lived to be depicted by routine 30-minute scans. During the very severe TC TAUKTAE, in the Arabian Sea during 13-19 May 2021, the INSAT3DR satellite was operated in rapid scan mode. This TC was developed near the North Bay region and made landfall at the Odisha coast after achieving severe tropical cyclone category. The visual animation of TIR1, WV, visible and differenced “TIR1-WV” imageries over TC were also extensively analysed to observe the deep convective cloud-top movement, out flow characteristics and other structural features. The pattern of large-scale circulation around cyclone is also analysed by using atmospheric motion winds in rapid scan mode.

The differenced BT (IR-WV) values of two channels during the entire life of cyclone was computed and analyzed (Fig. 1.14). These images well represents the asymmetric clouds within eyewall and inner core region of TC. The presence of over shooting clouds at some locations is found rapidly changing as it alters in the next 4 minute imageries. The deep overshooting clouds (blue in colour, with differenced BT $<-20^{\circ}\text{C}$) were observed in the southern part of the eyewall whereas the low clouds (red in colour, with differenced BT close to 0°C) were present in the norther part. The extent of differenced BT was found to be changing in every 4 minute images.

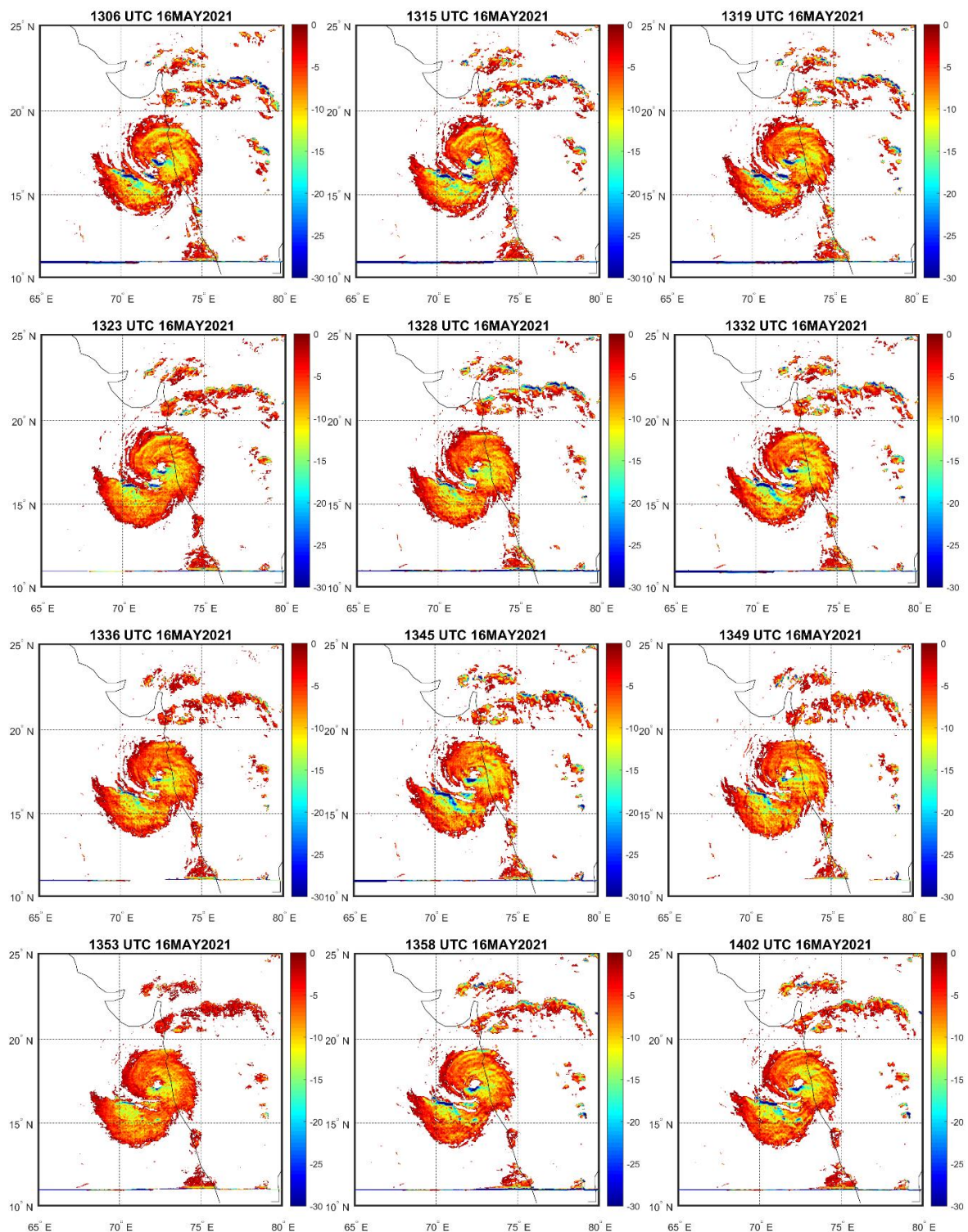


Figure 1.14: Asymmetric clouds within inner core region of TC during its peak intensity stage 1306-1402 UTC 16 May 2021.

The INSAT3D rapid acquisition images show the rapidly changing pattern within inner core region of cyclone.

1.7 SMAP satellite observation over TC TAUKTAE

Soil Moisture Active Passive (SMAP) is a United States environmental research satellite launched on 31 January 2015. The SMAP observatory includes a dedicated spacecraft and instrument suite in a near-polar, Sun-synchronous orbit. The SMAP measurement system consists of a radiometer (passive) instrument and a synthetic aperture radar (active) instrument operating with multiple polarizations in the L-band range. The combined active and passive measurement approach takes advantage of the spatial resolution of the radar and the sensing accuracy of the radiometer. The observations from L band radiometers, being in low frequency are uncontaminated by rain.

SMAP provides two wind speed products e.g. (i) Near-Real Time (NRT) wind speed and (ii) Final wind speed product. The NRT wind processing uses ancillary fields of shorter latency but lower quality. A final wind Speed version, reprocessed with a 1-month delay, which uses higher quality ancillary data. Additionally, SMAP also provide Tropical Cyclones (TC) ASCII files with SMAP 10-min maximum-sustained winds (in kn) and wind radii (in nm) for the 34 kn (17 m/s), 50 kn (25 m/s), and 64 kn (33 m/s) winds for each SMAP pass over a TC in all tropical ocean basins. The wind speed from NRT product of SMAP over TC Tauktae during 15-17 May has been shown in the Fig. 1.14. There were three partial coverage of SMAP over the system on 0130 UTC 15 May, 0239 UTC 16 May and 14UTC 17May. The maximum intensity observed by SMAP over the above passes was 33.73 m/s (65.57 knots), 32.21 m/s (62.61 knots) and 48.54 m/s (94.35 knots) respectively.

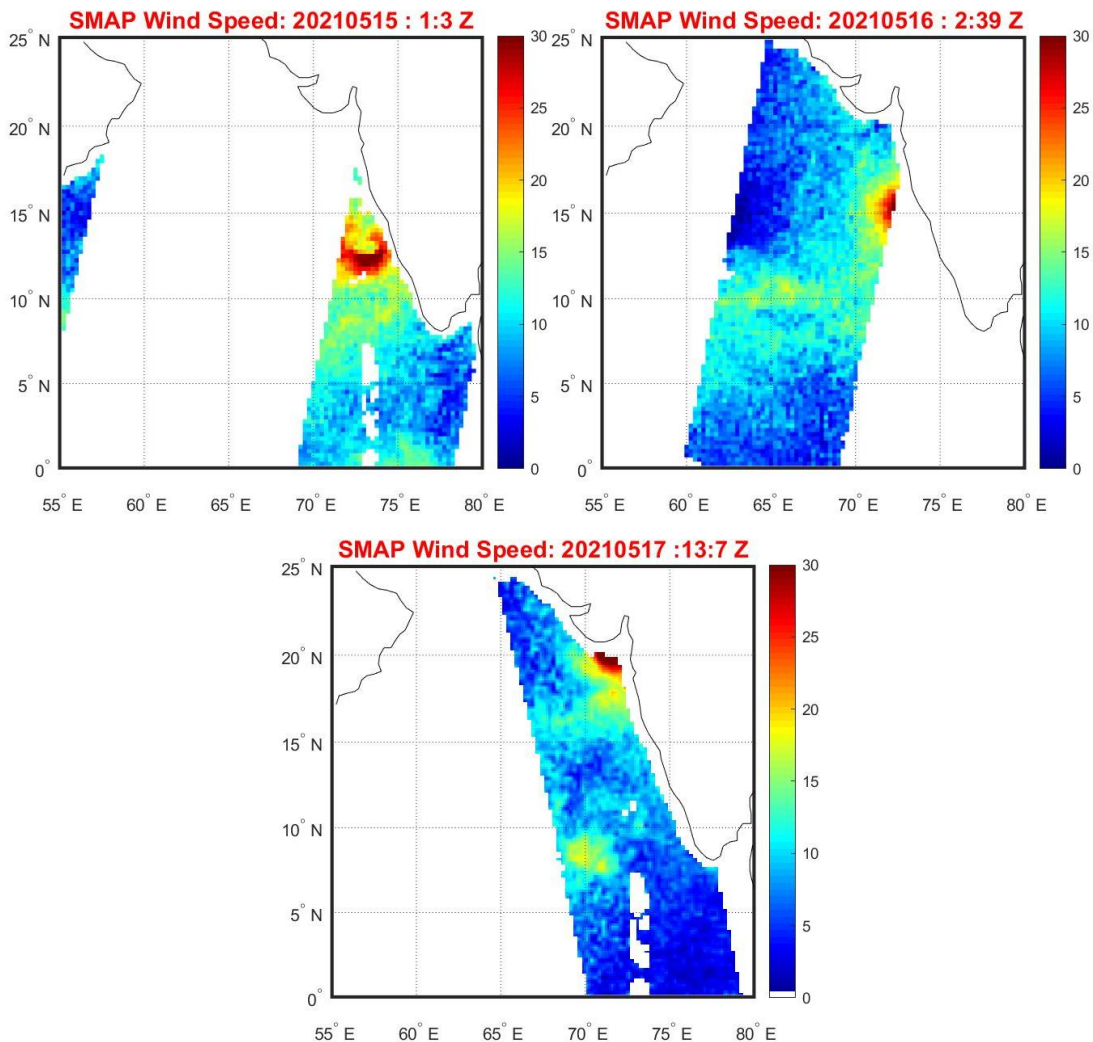


Figure 1.15: Wind speed over TC Tauktae during 15-17 May, observed by SMAP satellite (NRT product).

1.8 Forecast Dissemination through web portal SCORPIO/MOSDAC

Satellite based cyclone observation and real-time prediction over Indian ocean (SCORPIO) (<https://mosdac.gov.in/scorpio>) is a web based application designed to provide Web-GIS available on the MOSDAC portal (<https://mosdac.gov.in>). It works as a decision support system to support the disaster management system. For cyclone TAUKTAE, the scorpio website was updated in the real-time with following information:

- Cyclone track prediction
- Cyclone intensity prediction
- Ship avoidance region due to cyclonic winds
- Cyclone center estimation product using INSAT 3D data
- Cyclone centric images generated using INSAT3D imager channels
- ADCIRC based Storm surge forecast as animatef Gif

- Coastal Inundation as jpeg image
- Coastal Inundation as GIS layer along with other thematic layers to aid the Decision Support system
- Tropical Cyclone Heat Potential anomaly as GIS layer along with other thematic layers

The webpage of scorpio web-portal during cyclone TAUKTAE has been shown in the Fig. 1.16.

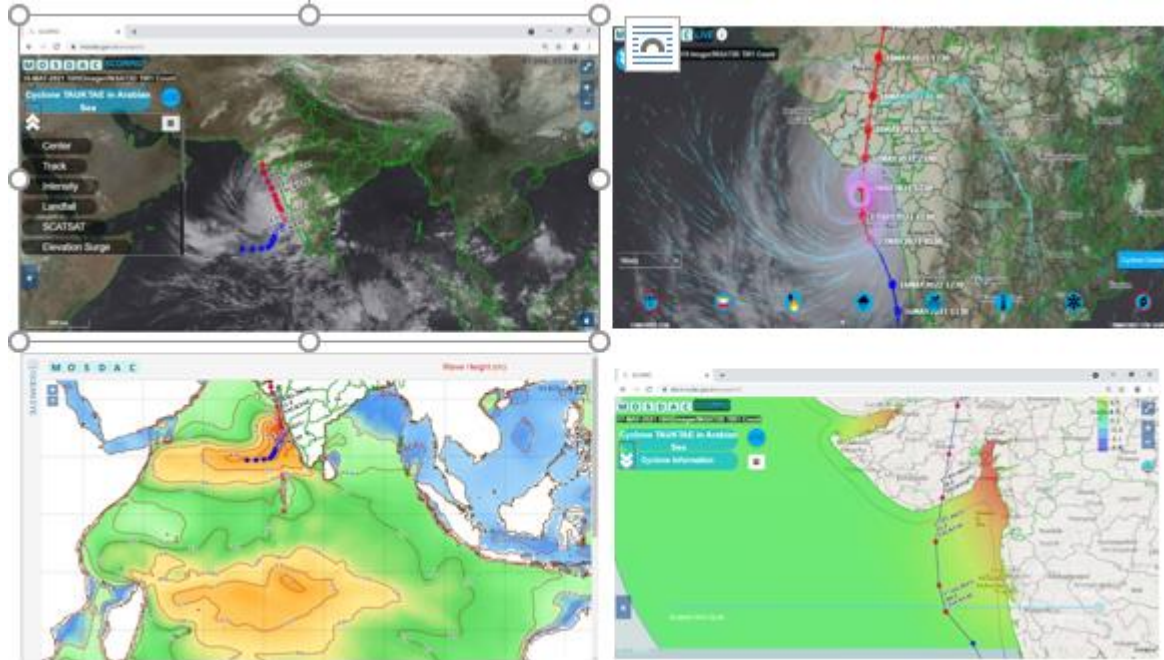


Figure 1.16: Cyclone forecast products disseminated through webserver SCORPIO

1.9 Coverage of cyclone TAUKTAE by media

Due to the advancement in the cyclone prediction models the alerts were timely generated for cyclone TAUKTAE and government took the preventive measures. The cyclone track and intensity until the landfall was continuously broadcasted via media channels, which made the wide publicity and awareness among the people. The personal interviews and live press conferences from IMD for the updates of cyclone TAUKTAE was telecasted during the whole day as cyclone was approaching the Saurashtra coast. The timely information saved the human loss and result the better preparedness to overcome the post-cyclone impacts. The media reports were providing the updates based on the foreign weather agencies as well as the India Meteorological Department.

1.10 Conclusions

The real time predictions of cyclogenesis, track and intensity of cyclone Tauktae have been discussed in this report. The real time generated forecasts were disseminated through SCORPIO web-portal linked with MOSDAC site (www.mosdac.gov.in).

The Cyclogenesis signatures of TC TAUKTAE was detected earliest on 09th May by GFS based Genesis Potential parameter. The track and intensity prediction of cyclone based on dynamical and numerical models viz. SAC-Lagrangian Advection Model and Hurricane Weather Research Forecast (HWRF) model, were provided continuously till the cyclone made landfall. The real time forecasts were compared to the real-time observed estimates obtained from India Meteorological Department and Joint typhoon Warning Centre (JTWC). The error analysis for all the forecasts have been performed and presented in the report. The landfall position and time forecast error in 24 hour was about 31.3 km and 1 hour (delay), respectively. The INSAT-3D visible and infrared data were analyzed to retrieve the cyclone structural parameter viz., center. INSAT3D TIR-1 data was used in ADT to estimate the cyclone intensity. INSAT3DR TIR-1 and water vapor images were processed to generate the differenced image (TIR-1 –WV) to study the rapid changes in the inner core of TC. The surface wind speed of SMAP satellite was also analyzed to study the cyclone wind asymmetry. Our plans consist of utilizing multi-satellite multi-sensor approach to retrieve key parameters of tropical cyclone e.g. accurate location, surface wind structure, asymmetry, and size of the cyclone, and develop methodology to assimilate this information in NWP models for improving the prediction of cyclone track and intensity. It is also planned to utilize key satellite observations of atmospheric and oceanic parameters to improve the accuracy of the prediction of location and intensity of cyclone at the time of its landfall.

References

1. Cintineo M. J., Pavolonis J., Sieglaff M., and Heidinger A. K. (2013): Evolution of severe and nonsevere convection inferred from GOES-derived cloud properties. *J. Appl. Meteor. Climatol.*, vol. 52, 2009–2023.
2. Chan, J. C. L. and Williams R. T. (1987): Tropical cyclone movement and surrounding flow relationship. *Mon Wea Rev* 110:1354-1374.
3. Dworak, R., Bedka K. M., Brunner J., and Feltz W. (2012): Comparison between GOES-12 overshooting top detections, WSR-88D radar reflectivity, and severe storm reports. *Weather and Forecasting*, Vol. 27, 684–699.

4. Hoover, B.T. and Morgan M.C. (2006). Effects of cumulus parameterization on tropical cyclone potential vorticity structure and steering flow. Preprints of the 27th AMS Conference on Hurricanes and Tropical Meteorology. April 23-28 Monterey, CA, paper 8B.5.
5. Jaiswal, Neeru and Kishtawal, C. M. (2011): Prediction of tropical cyclogenesis using scatterometer data, IEEE Transaction on Geoscience and Remote Sensing, vol. 49, Issue 12, pp. 4904 -4909.
6. Jaiswal, Neeru and Kishtawal, C. M. and Pal, P. K. (2013): Prediction of Tropical Cyclogenesis in North Indian Ocean using Oceansat-2 scatterometer (OSCAT) winds. Meteorology and atmospheric Physics, Vol. 119, pp. 137-149. DOI: 10.1007/s00703-012-0230-8.
7. Jaiswal Neeru, Kaushik Nitesh and Varma A. K. (2021): Advanced Dvorak Technique for Tropical Cyclone Intensity Estimation using INSAT-3D Satellite Data. SAC-Report: SAC/EPSA/AOSG/ASD/SR/05/2021.
8. Kotal, S.D., Kundu, P.K. and Roy Bhowmik, S.K. (2009): Analysis of cyclogenesis parameter for developing and non-developing low pressure systems over the Indian Sea, Nat. Hazards, 50:389-402
9. Kossin, J. P., Knaff, J. A., Berger, H. I., Herndon, D. C., Cram, T. A., Velden, C. S., Murnane, R. J. and Hawkins, J. D. (2007): Estimating Hurricane Wind Structure in the Absence of Aircraft Reconnaissance. Weather and Forecasting, 22, 89-101.
10. Singh, Sanjeev Kumar, Kishtawal, C.M. and Pal, P.K. (2011): Track Prediction of Indian Ocean cyclones using Lagrangian Advection Model. Natural Hazards DOI 10.1007/s11069-012-0121-9.
11. Singh, S. K., Kishtawal, C. M., Singh, R. Jaiswal, Neeru and Pal, P. K. (2012): Impact of Vortex-Removal from Environmental Flow in cyclone Track Prediction using Lagrangian Advection Model. Meteorology and Atmospheric Physics, 117,103–120. DOI 10.1007/s00703-012-0198-4
12. Singh, S. K., Jaiswal Neeru, Kishtawal, C. M., Singh R., Pal., P. K. (2013): Early detection of cyclogenesis signature using global model products, IEEE Transactions on geoscience and remote sensing 52(8), 5116-5121.

2. Observing Ocean Conditions Prior and Post Cyclone using Satellite and In-situ data

**Anup Kumar Mandal, Seemanth M., Jishad M., Suchandra Aich
Bhowmick and Neeraj Agarwal**

2.1 Introduction

Arabian Sea (AS), the western part of North Indian Ocean (NIO) produce lesser number of tropical cyclones as compared to eastern part i.e. Bay of Bengal(BoB). Climatologically, more cyclones form in BoB as compared to inert AS (Sahoo and Bhaskaran 2016) because the ocean/atmospheric dynamics over these regions are entirely different. It is well known that atmosphere plays a crucial role in cyclogenesis. Further studies like Ali et al 2013 and 2007, Shay et al 2000, Bhowmick et al 2019, Goni et al. 2003 etc highlighted role of ocean in modulation of cyclone genesis, track and intensity. Over BoB, active river discharge makes upper layer of the ocean fresh. This make the ocean stratified with shallow mixed layer depth (MLD). A stratified ocean retain heat in upper layers (Akhil et al 2014) making BoB a hotspot for cyclone formation. Unlike BoB, AS is more saline and very well mixed, making it less conducive for cyclogenesis.

Although very few, cyclones over the AS are catastrophic in nature and west coast of India is vulnerable to these hazards. AS registers cyclonic events during pre-monsoon phase from May –June and in post monsoon October to December. In an interesting study Evan and Camargo (2011) showed that cyclones of May and June over AS are associated with early and late monsoon onset, respectively whereas post-monsoon cyclogenesis over this region is known to be modulated by both monsoon rainfall and the El-Niño accompanied with positive Indian Ocean Dipole events. No single phenomena, however, can fully explain the variability of cyclogenesis observed in AS region. Further in recent years AS has shown a significant rise in the cyclonic activities which was also linked to global warming by Prassana kumar et al 2009 and Murakami et al 2017.

In the current study, we analyse the ocean conditions before and after the recent pre-monsoon cyclone Tauktae that formed over AS on 14th May 2021. It attained a category 4 ‘extremely severe cyclonic storm’ status on 17th of May with 3 min sustainable wind speed of 195 km/h. The damage because of this extreme event accounted to 2.1 billion dollars with 174 fatalities. The study shows ocean features were conducive for the formation of the cyclone. The Sea Surface Temperature (SST) from INSAT3D and Sea Surface Salinity (SSS) from Soil Moisture Active Passive (SMAP) were used for studying Ocean precondition before the event. The sea surface salinity anomaly observed from the satellite indicated freshening near the Kerala and Karnataka coast with salinity between 33-34 PSU. This relative fresh water was persistent between 70-72° E from 7-14 May and has been instrumental in trapping ocean heat. The SST anomaly observed from INSAT shows a positive temperature anomaly of 1°C during this

phase. The storm surges up to 4m and wave height of 5.6 m were observed in numerical model simulations during the cyclone. The post cyclonic period shows SST cooling by 2 °C and upwelling driven enhancement in salinity.

2.1.1 Cyclone Tauktae

On May 11, a large area of low pressure in the equatorial AS was observed which slowly moved eastwards and organized amid favourable conditions. The system on May 13 was identified as a potential tropical cyclone. The system gradually intensified, around the low-level vortex. It further strengthened to become a deep depression at 12:00 UTC the next day. Around this time, the system turned north-eastwards towards India and caused heavy rainfall over the southern portions of the country. As the system became even more organized and intensified into a cyclonic storm, it received the name Tauktae by the IMD. Later, the storm continued intensifying, and at 03:00 UTC on May 17 Tauktae reached its peak intensity as an extremely severe cyclonic storm. The maximum 3-minute sustained winds of 195 km/h and maximum 1-minute sustained winds of 220 km/h were observed. Minimum sea level pressure was 950 hPa making the storm equivalent to a Category 4 tropical cyclone on the Saffir–Simpson scale. Finally the storm neared the coast of Gujarat and made landfall near Una in Gujarat. Insat-3D Thermal Infrared images during different phases of cyclone ‘Tauktae’ are shown in Fig. 2.1.

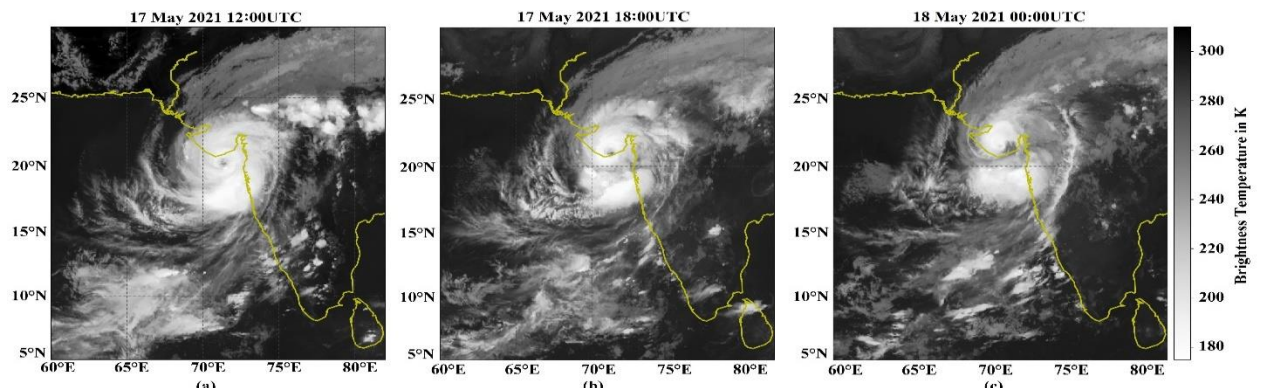


Figure 2.1: Tauktae cyclone images acquired by Insat-3D (a) 6h prior landfall (b) during landfall and (c) 6 hour after landfall

2.2 Data and Model used

2.2.1 Satellite Data

The Sea Surface Temperature (SST) from INSAT3D and Sea Surface Salinity (SSS) from Soil Moisture Active Passive (SMAP) were used for this study for May 2021. Indian satellites for met-ocean applications, INSAT-3D having a six-band imager and 19-band sounder. SST is derived with a spatial resolution of 4 km from split thermal window channels (10.2- 11.3 μ m

and $11.5 - 12.5 \mu\text{m}$) during daytime and using additional mid-IR window channel ($3.7 - 4.1 \mu\text{m}$) during night time over cloud-free oceanic regions (Gangwar and Thapliyal, 2020; Walton et al., 1998). The SST data sets were downloaded from MOSDAC (Meteorological and Oceanographic Satellite Data Archival Centre, <https://mosdac.gov.in/>).

The eight-day averaged SMAP L3 product having spatial resolution of 0.250×0.250 is used for this study. The eight-day product is created by averaging eight days of L2 data. The primary goal of the SMAP mission is the retrieval of measurements over land. However, the L-band microwave instrument enables the SMAP to retrieve SSS over ocean. The SSS datasets are available at NASA Physical Oceanography Distributed Active Archive Center (PO.DAAC) (<http://podaac.jpl.nasa.gov>). The temperature and Salinity anomalies were computed with respect to the average of May 2021 data.

In this study merged field of SSH has been used to look into the existing eddies prior to formation of the cyclone. Global ocean multi-mission altimeter gridded sea surface heights (SSHs) and derived variables are currently available from the European Copernicus Marine Monitoring Service Environment (CMEMS). The merged field of SSH combine the observations from Jason-3, Sentinel-3A, HY-2A, Saral/AltiKa, Cryosat-2, Jason-2, Jason-1, T/P, ENVISAT, GFO, ERS1/2. The sea-level anomaly (SLA) is computed after removing long-term mean (20 years) SSH from the original data. Weekly average SLA has been analysed to examine the SLA conditions prior to and during the formation of Tauktae.

2.2.2 Numerical Model

In assessing the impact of Tauktae over the Ocean two numerical models, one for surge and the other for wave predictions were used. The coupled Adavanced CIRCulation Model and Simulating WAve Nearshore (ADCIRC+SWAN) is used for the surge prediction and WAVEWATCH-III is used for the wave height prediction.

ADCIRC+SWAN

Storm surge induced coastal inundation maybe considered as the worst disaster caused by a cyclone. We therefore analysed storm surge forecast generated using state of the art coupled ADCIRC+SWAN model. The ADCIRC model discretizes the shallow-water equations using finite element methods defined on unstructured meshes (Luettich and Westrink 2004). The accurate description of coastal bathymetry fromETOPO-2 global relief model data was used to prepare the mesh for storm surge simulations as shown in Fig. 2.2. The spatial resolution near land is 1km and 60km in the open ocean. ADCIRC model is primarily forced by tides,

winds and wind-waves; during a cyclone, wind stresses are the dominant forcing. Coupling of the ADCIRC model with a wind wave model for capturing wave-induced setup has been established (Dietrich et al. 2011). This model is forced using winds from National Centre for Medium Range Weather Forecasting (NCMRWF), which are available at 0.25° spatial resolution. The ADCIRC+SWAN model was integrated for 10 days with analysed wind fields to achieve model spin up. After that storm surge forecast was generated using NCMRWF 0.25° forecast wind fields.

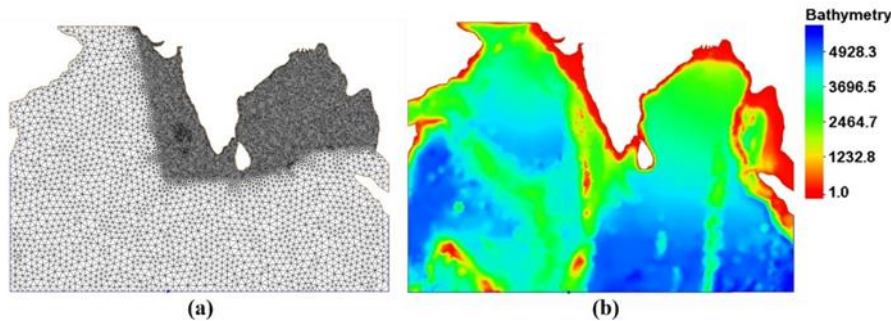


Figure 2.2: Computational domain (a) with nodes and (b) with bathymetry

Wave Watch-3

Wave prediction during such an extreme event is extremely important for safe passages of cargo ships and fishing activities. For this purpose, high resolution data assimilative wave forecasting system based on WAVEWATCH III (WW3) model (Ardhuin 2010, Hasselmann 1985, user manual 2016) consisting of four nested grids (Global grid at 100 km, Indian Ocean grid at 50 km, Northern Indian Ocean grid 10 km and a Coastal grid 2.5 km resolution) is used. The region covered under each domain is shown in Fig. 2.3. For grid generation, bathymetry data has been derived from ETOPO1 and shoreline data is taken from Global Self-consistent Hierarchical High resolution (GSHHS) database. Spectrum is discretized with 29 frequencies, ranging from 0.0350 to 0.5047 Hz with 1.1 Hz increment factor and 36 directions with a 10-degree increment. The forecasting system uses 10m analysis and forecast wind components obtained from the National Centre for Medium Range Weather Forecasting (NCMRWF) as the forcing field. In order to improve the predictability of the model, SARAL/AltiKa, Jason3 and Sentinel measured wave heights are being assimilated into this 24-hr hindcast cycle.

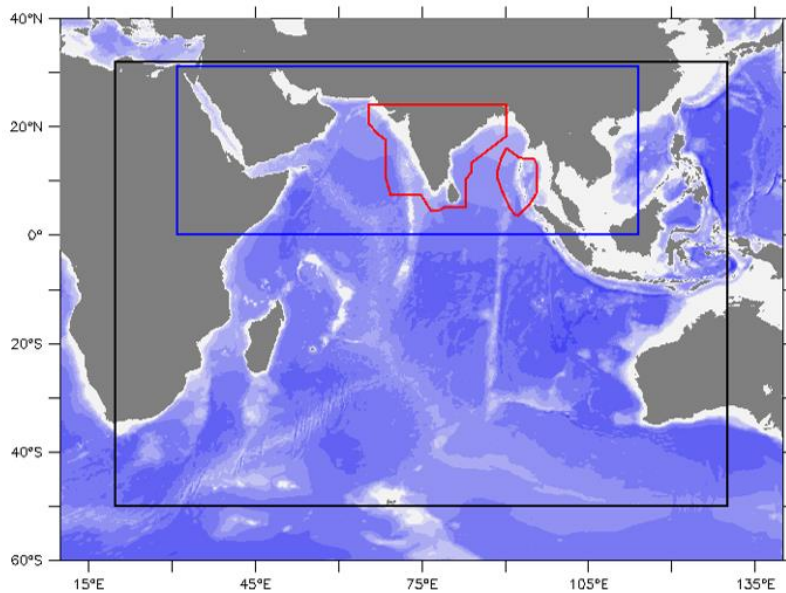


Figure 2.3: Nested domains chosen for the WW3 model. Black box is Indian Ocean domain with $0.5^{\circ}\text{x}0.5^{\circ}$ resolution and blue box is the Northern Indian Ocean domain ($0.1^{\circ}\text{x}0.1^{\circ}$ resolution). Red box represents the Coastal domain ($0.025^{\circ}\text{x}0.025^{\circ}$) covering the EEZ of India. All these domains are nested in a parent global domain ($1^{\circ}\text{x}1^{\circ}$ resolution).

2.3 Results and Discussion

Cyclone Tauktae developed over the AS during pre-monsoon month of May, was a category - 4 cyclone, which caused severe devastation and fatalities. Evan and Camargo (2011) in their study showed cyclones of May and June over AS are associated with early and late monsoon onset, respectively. Hence it is useful to understand the mechanisms and processes associated with the cyclone not only for its better predictability but also to generate an outlook on behavior of upcoming monsoon. Thus, to begin with, evolution of SST anomaly from INSAT -3D (Fig. 2.4) is analysed over the AS near the location where low pressure area was observed prior to the formation of Tauktae. Typically, this region was between $8\text{-}13^{\circ}$ N. Interestingly positive SST anomalies up to $0.5\text{-}1^{\circ}\text{C}$ were observed in this region from 3rd May -14th May, prior to the formation of the low pressure area. However, after 14th May the gradual cooling was evident. One of the obvious reasons for this positive SST anomaly could be insolation, but as it can be seen that, ocean is cold on the west of this location and warmer on the east. Fig. 2.5a show the salinity and its anomaly for AS on 13th May and 20th May respectively. The figure clearly shows that the salinity prior to passage of the cyclone (i.e. on 13 May, 2021) near the Kerala and Karnataka coasts (shown in the black box) was between 33-34 PSU. The region was relatively fresh as compared to its surroundings by around 1psu. This freshening might have resulted in stratification induced warming of the upper ocean in this region as compared to western part of AS. In fact, analysis of SMAP data from 2017 to 2021 also highlights

phenomenal freshening of this area in 2021 implying an enhanced stratification induced heating of coastal AS (Fig. 2.5b). Time evolution of salinity anomaly between 8-13 ° N clearly indicated trapped fresh water patch near these coastal areas from 8 -16 May 2021 (Fig. 2.6). Incidentally the initial low pressure area was also formed in the same region.

After the passage of the cyclone, salinity anomaly clearly indicates gradual increase in its salinity which is now 35-36 PSU along the track of the cyclone. This implies an increase in salinity by 0.6-1 psu and can be impact of the upwelling due to cyclone. Fig. 2.7 shows the snapshot of daily averaged SST, 8-day averaged SSS and estimated density for 12th May 2021 and 20th May 2021, corresponding to period prior to and post passage of Tauktae cyclone. As discussed previously, low salinity features (< 34 psu) in the southeastern AS, around Lakshadweep islands, can be clearly seen in the sea surface salinity image for 12th May 2021. This low salinity is suspected for strong surface stratification, which resulted in surface heating due to high solar insolation (Fig. 2.7a). This can be clearly seen in the SST image in southeastern AS, where large scale warming (~ 31°C) can be seen, consistent with the low salinity region. Hence, it can be seen that the ocean surface conditions were conducive for the formation and sustainability of cyclone in the region. The seas surface density is also low as compared to the surroundings in the region.

After the passage of cyclone, surface becomes cool and saline due to Ekman pumping associated with high cyclonic winds. There is a drastic change in the physical properties after the passage of cyclone, which can be seen in the SST, SSS and density difference maps post and pre cyclone. There is a temperature drop of ~ 2°C from 12th to 20th May, while a salinity increase of ~ 1psu, due to which the density increases by > 1 Kg/m3.

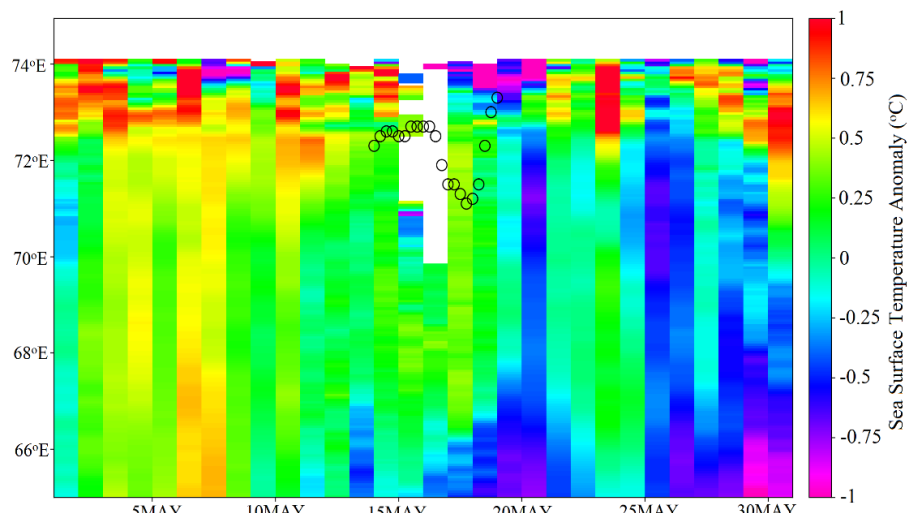


Figure 2.4: The time evolution of SST anomaly from INSAT3D for an area between 8-13° N. The black circles indicate the location of cyclone passage in time.

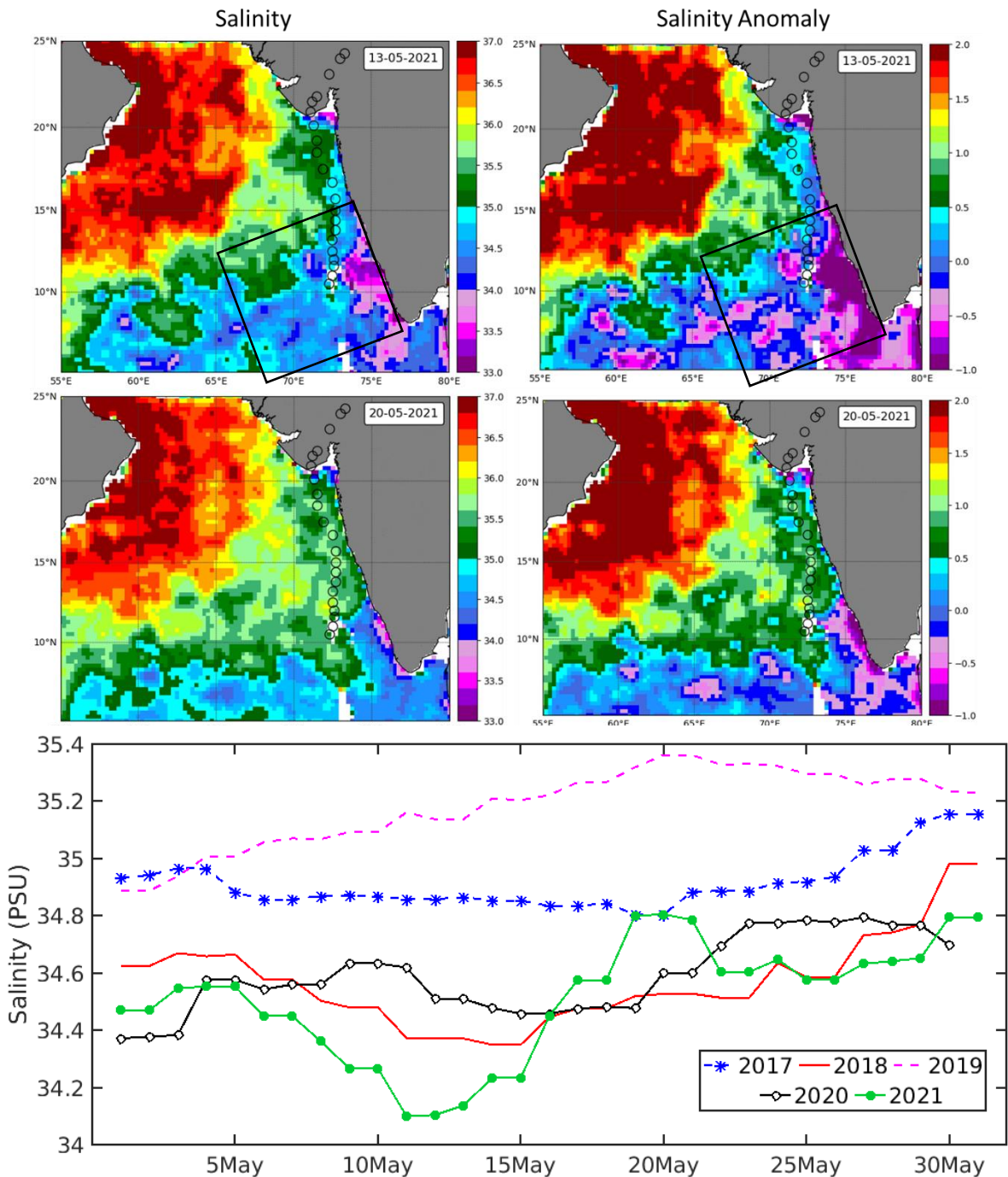


Figure 2.5: (a) The Sea Surface Salinity and its Anomaly over Arabian Sea on 13th May 2021 before Tauktae and on 20th May 2021 after passage of the cyclone. (b) Five years timeseries of average salinity over coastal AS between 70 - 78E and 08 - 15N]

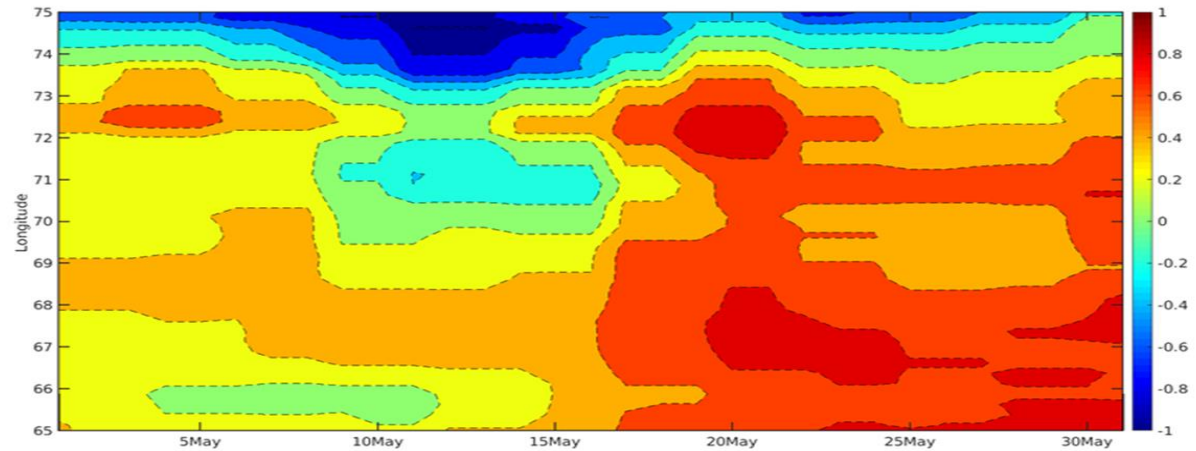


Figure 2.6: The time evolution of Sea Surface Salinity Anomaly over Arabian Sea

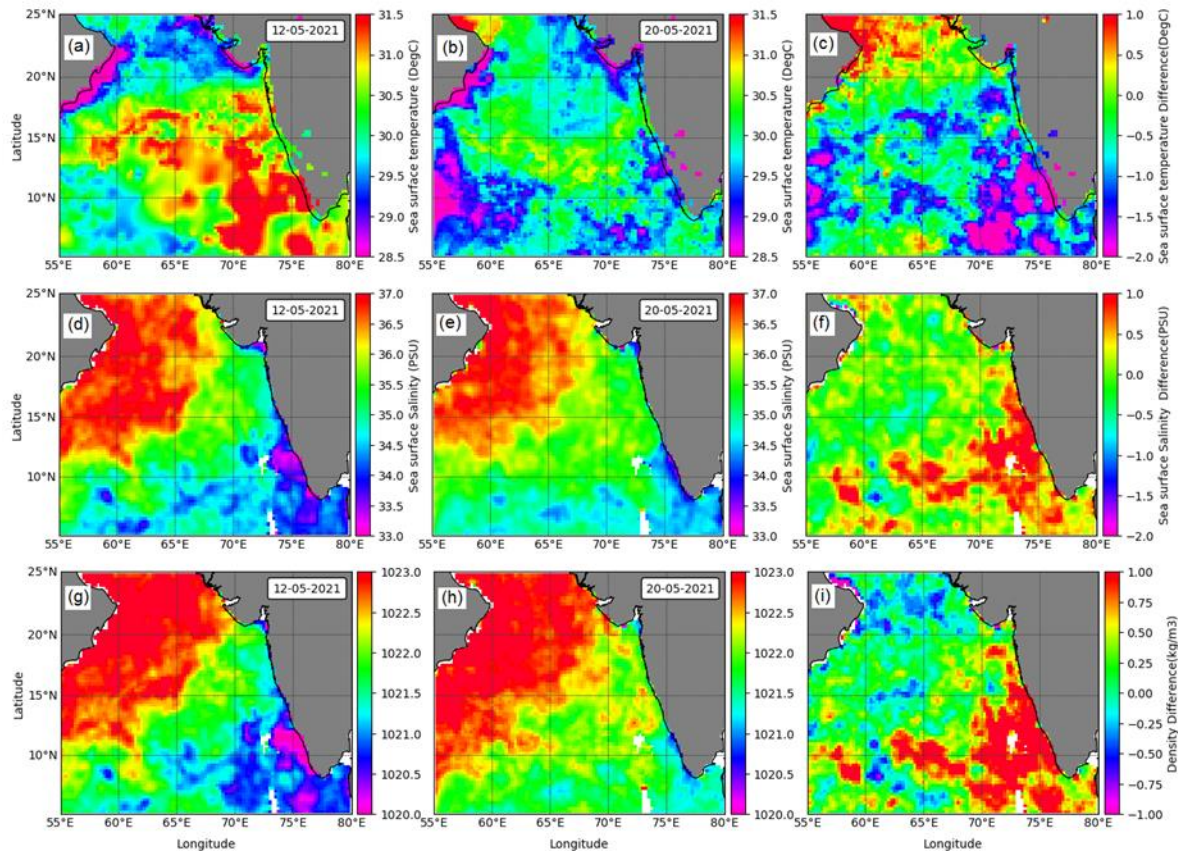


Figure 2.7: SST, SSS and density for before and after the cyclone and difference between before and after cyclone

Density changes are associated with both salinity and temperature changes, surface cooling and salinification can increase the density, however, which physical parameter (SST or SSS) contributed more to changes in density is not known.

Density changes were computed in two ways, one by keeping fixed SST and another, by keeping fixed SSS (both corresponding to 12th May) in order to assess the individual contribution of SST and SSS in density change and the results are shown in Fig. 2.8. It can be clearly seen that density changes (~ 50%) resulted mainly due to cooling of SST, while the salinity changes resulted in change (~ 40%) in the total density changes.

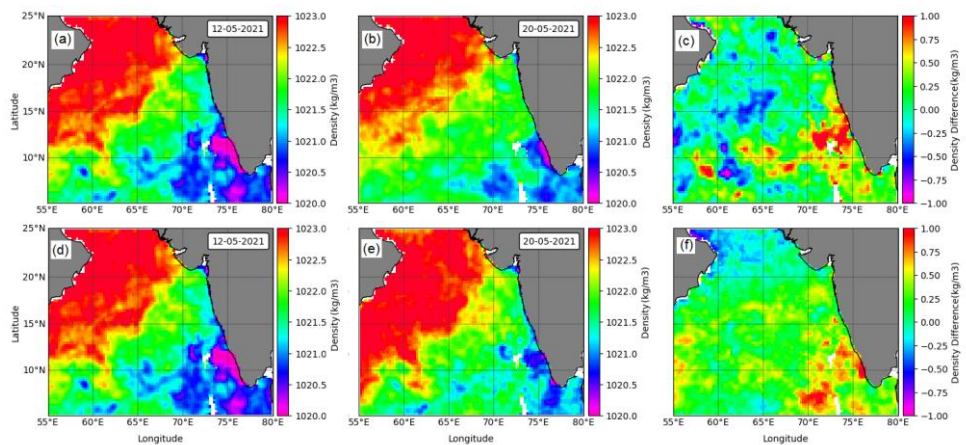


Figure 2.8: The density computed using constant temperature (a-c) and constant Salinity (d-f) for before and after the cyclone and difference between before and after cyclone

On 17th May Tauktae attained its peak intensity (3mins sustainable wind speed of 195 km/h) and did sufficient destruction to the west coast of India as it approached the Gujarat coast near Una. Storm surge that was observed during Tauktae using the coupled numerical model (ADCIRC+SWAN) is shown in Fig. 2.9. The storm surge forecast for 17th May 2021 with a lead time of 12, 18 and 24 hours is shown in Fig. 2.9. The forecast shows storm surge of about 1.25m near Mumbai and 0.8m near Nava Rajapara (Fig. 2.9a) 6 hour before the landfall of Tauktae. From Fig. 2.10b, maximum surge height of about 2.2m was predicted near Nava Rajapara in the Bhavnagar district of Gujarat region during landfall. However, the forecasted surge height was maximum (3.8m near Nava Rajapara) 6 hour after landfall of the cyclone as shown in Fig. 2.9c.

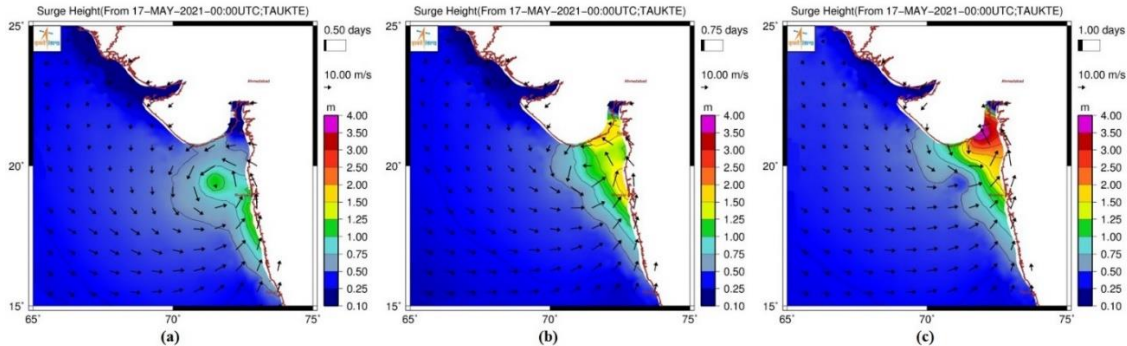


Figure 2.9: Storm surge forecast during Tauktae cyclone (a) 6h prior landfall (b) during landfall and (c) 6 hour after landfall

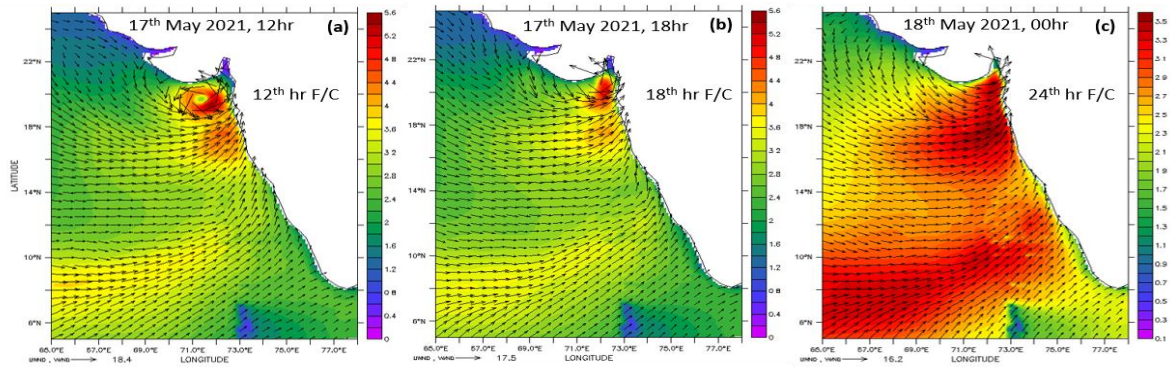


Figure 2.10: WW3 forecasted SWH (m) initialised from 17th May 2021 overlaid with forcing wind vectors. (a) Before the predicted landfall, (b) during the predicted landfall and (c) after the predicted landfall.

WW3 forecasted SWH initialised from 17th May 2021 is shown in Fig. 2.10. 12th hour forecast valid for 12 UTC of the same day (before the landfall of the cyclone) showed a maximum SWH of ~5.5m off the northern Maharashtra coast (Fig. 2.10a). High waves with SWH ~2.5m were predicted along the Diu coast. During the landfall of the cyclone, predicted maximum wave height was ~5m in the offshore region and near the coast of Diu, Hazira and Bhavnagar, it was around 2-2.5m (Fig. 2.10b). Wave height in the southern part of Gulf of Khambhat was also high (~3-3.5m.). After Tauktae made landfall, during the early hours of 18th May 2021, the 24 hours forecast of SWH was ~3.5m in the southern part of Gulf of Khambhat and ~1.5m inside the Gulf (Fig. 2.10c). Wave height near the coast of Diu and Bhavnagar was predicted to be ~2m.

2.4 Conclusion

Ocean conditions before and after post monsoon cyclone Tauktae that formed over AS on 14th May 2021 is analysed using the satellite as well as in-situ observations. Numerical models simulations are used to analyse the impact of the cyclone in terms of surge and waves. Tauktae is a category 4 ‘extremely severe cyclonic storm’ which had a landfall over Indian coastal belt

of Gujarat. The damages caused by the cyclone was of worth 2.1 billion dollars with fatalities of 174 lives. The study shows ocean features were conducive towards the formation of the cyclone and satellite observations clearly points at this. The Sea Surface Temperature (SST) from INSAT3D and Sea Surface Salinity (SSS) from Soil Moisture Active Passive (SMAP) are explored to the fullest for analysing the ocean preconditions. The sea surface salinity and its anomaly from the satellite indicated the fresh sea water patch near to the Kerala and Karnataka coast. The salinity over this area was between 33-34 PSU. This fresh water mass was stagnated between 70-72° E from 7-14 May. This patch of less saline water mass trapped enormous amount of ocean heat and thus we observe SST anomaly observed from INSAT showing a positive anomaly up to 1°C during this phase. The storm surges up to 4 m and a wave heights of 5.6 m are observed in numerical model simulations during the cyclone. The post cyclonic period shows SST cooling by 2°C and upwelling driven enhancement in salinity.

References

1. Ardhuin, F., Rogers, W.E., Babanin, A.V., Filipot, J., Magne, R., Roland, A., van der Westhuysen, A., Queffeulou, P., Lefevre, J., Aouf, L., Collard, F., 2010. Semiempirical dissipation source functions for ocean waves. Part I: Definition, calibration, and validation. *J. Phys. Oceanogr.* 40, 1917–1941.
2. Dietrich, J. C., Westerink, J. J., Kennedy, A. B., Smith, J. M., Jensen, R. E., Zijlema, M., ... & Cobell, Z. (2011). Hurricane Gustav (2008) waves and storm surge: Hindcast, synoptic analysis, and validation in southern Louisiana. *Monthly Weather Review*, 139(8), 2488-2522.
3. Dietrich, J. C., Zijlema, M., Westerink, J. J., Holthuijsen, L. H., Dawson, C., Luettich Jr, R. A., ... & Stone, G. W. (2011). Modeling hurricane waves and storm surge using integrally-coupled, scalable computations. *Coastal Engineering*, 58(1), 45-65.
4. Hasselmann, S., Hasselmann, K., Allender, J.H., Barnett, T.P., 1985. Computations and parameterizations of the nonlinear energy transfer in a gravity-wave spectrum. Part II: Parameterizations of the nonlinear energy transfer for application in wave models. *J. Phys. Oceanogr.* 15, 1378–1391.
5. Luettich, R. A., & Westerink, J. J. (2004). Formulation and numerical implementation of the 2D/3D ADCIRC finite element model version 44. XX (p. 74). R. Luettich
6. The WAVEWATCH III Development Group (WW3DG), 2016: User manual and system documentation of WAVEWATCH III version 5.16. Tech. Note 329, NOAA/NWS/NCEP/MMAB, College Park, MD, USA, 326 pp.+ Appendices.

7. Akhil, V., Durand, F., Lengaigne, M. and Vialard, J., (2014) A modeling study of the processes of surface salinity seasonal cycle in the Bay of Bengal JGR: Atmosphere doi: 10.1002/2013JC009632
8. Ali MM, Jagadeesh PSV, Jain S (2007) Effects of eddies and dynamic topography on the Bay of Bengal cyclone intensity. EOS Trans AGU 88(8):93–95
9. Ali MM, Kashyap T, Nagamani PV (2013) Use of sea surface temperature for cyclone intensity prediction needs a relook. EOS 94:117
10. Bhowmick S. A, Agarwal N, Ali M.M, Kishtawal C.M. and Sharma R. (2019), Role of ocean heat content in boosting post-monsoon tropical storms over Bay of Bengal during La-Niña events, Climate Dynamics, 52: 7225-7234, DOI 10.1007/s00382-016-3428-5.
11. Evan, A.T and Camargo S.J. (2011). A climatology of Arabian Sea Cyclonic Storms, Journal of Climate Vol 24, 1, 140-158.
12. Goni GJ, Trinanes JA (2003) Ocean thermal structure monitoring could aid in the intensity forecast of tropical cyclones. EOS Trans AGU 84(51):573
13. Murakami, H., G. A. Vecchi, and S. Underwood, 2017: Increasing frequency of extremely severe cyclonic storms over the Arabian Sea. Nat. Clim. Change, 7, 885-889.
14. Prasanna Kumar, S. Roshin R.P, Navvekar J, Kumar P.K.D, Vivekanandan, E, (2009) Response of the Arabian Sea to global warming and associated regional climate shift, Marine Environmental Research 68, 217-222.
15. Sahoo, B. and Bhaskaran, PK (2016) Assessment on historical cyclone tracks in the Bay of Bengal, east coast of India. Int. Journal of climatology 36(1), pp-95:109.
16. Shay LK, Goni GJ, Black PG (2000) Effects of a warm oceanic feature on Hurricane Opal. Mon Weather Rev 128(5):1366–1383
17. Walton, C., Pichel, W., Sapper, J. and May, D., 1998. The development and operational application of nonlinear algorithms for the measurement of sea surface temperatures with the noaa polar-orbiting environmental satellites. Journal of Geophysical Research: Oceans, 103(C12): 27999-28012.
18. Gangwar, R.K. and Thapliyal, P.K., 2020. Variational based estimation of sea surface temperature from split-window observations of insat-3d/3dr imager. Remote Sensing, 12(19): 3142.

3. Rainfall Estimation over Tropical Cyclone

Neerja Sharma and Atul Kumar Varma

3.1 Introduction

Recent decades are witnessing more fiercer and powerful tropical cyclones (TC) in Arabian Sea. Recent TC, Tauktae falls under this category and regarded as extremely severe TC after 23 years to hit Gujarat coast. Such whacky TCs are characterized with extreme winds and rainfall which generally bring major damage to life and infrastructure (e.g. Rappaport, 2000; Webster, 2008). Torrential rain from intense TCs not only severely impact the coastal regions where it make landfall but may also significantly affect far inland from the coast.

Continuous monitoring of rainfall from geostationary satellite INSAT-3D/3DR plays a vital role in providing relief and rescue during these disastrous conditions. Hydro-Estimator (H-E) is one of the method developed for retrieving rainfall from Infra-Red (IR) observations from INSAT-3D/3DR satellite. Rainfall estimation from IR observations depends solely on cloud top temperature and thus termed as an indirect approach. The rainfall measurements from IR may improve further by incorporating additional information of atmospheric parameters in the retrieval technique. H-E method is based on this approach and utilizes model derived additional parameters (e.g. Total precipitable water and relative humidity) along with brightness temperature (Tb) of IR observations to retrieve rainfall from INSAT-3D/3DR satellite (Varma and Gairola, 2015). This technique is successfully providing rain estimates from Tb observations at 10.7 μm channel of INSAT-3D/3DR and products are operationally available on MOSDAC web portal of SAC, ISRO. Kumar and Varma (2016) demonstrated the improvement in short range weather prediction by assimilating H-E rain from INSAT-3D/3DR in WRF model. Technique is further applied to high-resolution IR observations from a polar-orbiting satellite as preparatory to later its operational implementation with Oceansat-3 SSTM observations (Sharma and Varma, 2020).

The present section is aimed to show the efficacy and reliability of H-E products of INSAT-3D/3DR satellite in monitoring rainfall from extremely severe TC, Tauktae formed in Arabian Sea during 12-18 May 2021. Section begins with the briefing of H-E retrieval technique and its methodology followed by discussion on spatial distribution of rainfall during Tauktae. In addition, section also presents the validation results of H-E with Indian Meteorological Department (IMD) surface rain gauges observations and Integrated Multi-satellitE Retrieval for GPM (GPM-IMERG) satellite rain products.

3.2 H-E retrieval technique

The H-E method described herein is based on work by Kuligowski (personal communication). In H-E method, convective and non-convective cores are identified, and different R-Tb relationships are provided for them. This allows higher precipitation rates for the convective cores. For convective core, rain (R_c) is given by,

$$R_c = a \exp(-bTb_{10.7}^{1.2}), \quad \dots\dots\dots(1)$$

Where, $Tb_{10.7}$ is brightness temperature measured at 10.7 μm channel, and a and b are the regression coefficients which are precipitable water (PW) dependent. This makes the Tb versus R relationship dynamic in nature.

For a non-convective core, the relationship between $Tb_{10.7}$ and R_n is given as:

$$R_n = (250 - Tb_{10.7}) * (R_{max}/5) \quad \dots\dots\dots(2)$$

R_{max} is again a function of PW. R_{max} is again PW dependent. R_n is not allowed to exceed - corresponding convective rain rate (R_c).

In H-E method, the precipitation at a pixel is allowed to be combination of both convective and non-convective core. This is worked out by considering a pixel box of 101X101 pixels surrounding the pixel of interest. The Z score at each pixel is determined as,

$$Z = (T_{mean} - Tb_{10.7}) / \sigma \quad \dots\dots\dots(3)$$

The maximum allowable value of Z is 1.5.

If $Z < 0$; $R = 0$, i.e., pixel either cirrus or inactive convective

$$\text{Otherwise, } RR = [R_c * Z^2 + R_n * (1.5 - Z)^2] / [Z^2 + (1.5 - Z)^2] \quad \dots\dots\dots(3)$$

R_c is the rain from the convective core given by (1) with coefficients determined by PW from NWP model. R_n is rain from non-convective core given by (2). If $Z=1.5$, the pixel rain rate RR reduces to convective type only (given by (1)). On the other hand, if $Z=0$, the pixel rain rate RR is determined by purely non-convective rain (given by (2)).

The (3) above provides the first guess precipitation amounts. The precipitation thus estimated is further modified to account for the wetness/dryness of the atmosphere and for the precipitation that comes from the warm clouds. The several steps involved for such modifications are as follows:

(a) *Correction for Wet/dry Environment*

A small correction in the brightness temperature ($T_{b10.7}$) values is carried out to account for wetness of the environment. This adjustment is needed to account for evaporation of the precipitation in the dryer environment below the cloud.

(b) Warm-top modification

The equilibrium level is computed by following a parcel along a saturation adiabat upward (from lifting condensation level) to where the parcel temperature becomes equal to the environmental temperature. Strength of the convection is determined by comparing the temperatures of the convective tops with that of equilibrium level. This level comes before tropopause for the warm rain.

In H-E method, NCEP model derived temperature and relative humidity profiles are used in a atmospheric thermodynamic model to determine equilibrium temperature at a particulate pixel. This correction is applied to pixels that are warmer than the equilibrium level temperature.

- If the $(T_{eq} - T_{min}) < 10 \text{ K}$, then T_{min} in the pixel-area is used instead of $T_{b10.7}$ of the pixel for warm top correction. The modification is as follows:

$$T_{b10.7} - [(213 - T_{eq}) * 0.9] \text{ or } 25 \text{ K (whichever less)}$$

- If the $(T_{eq} - T_{min}) > 10 \text{ K}$, the modification is as follows

$$T_{b10.7} - [(213 - T_{eq}) * 0.6] \text{ or } 15 \text{ K (whichever less)}$$

(c) Orography correction

Orography adjustment is carried out using 850 hPa Winds and topography from a digital elevation model at 4 km resolution (Vicente et al., 2002).

3.3 H-E rain during Tropical cyclone Tauktae

Widespread rainfall prior to the formation of TC started from 12th May 2021 over Lakshadweep in Arabian Sea, H-E rain at 0100 UTC is shown in Fig. 3.1a. On 13th May 2021 at 0830 UTC, low pressure area developed over and near to Lakshadweep area in Arabian Sea. Rainfall occupied larger area near to south Arabian Sea due to formation of low pressure (Fig. 3.1b). Low pressure developed into depression and deep depression in the morning and evening hours of 14th May respectively. At 2330 UTC on 14th May, deep depression strengthens into TC Tauktae. Rainfall region became denser on 14th May at 0500 UTC shown in Fig. 3.1(c). As Tauktae further intensified into severe cyclonic storm on 15th May and moved towards north, high rainfall is also recorded towards north of Arabian sea. In addition, structure of TC is also

captured well by H-E rain. Tauktae, further moved toward north along the west coast of India with more power and classified as very severe cyclone in the evening of 16th May. Rainfall structure of Tauktae is well recorded on 16th May at 1259UTC. H-E not only registered high intense rainfall but well discriminated eye of cyclone with the high intense rain from eyewall. Tauktae rapidly intensified into extremely severe cyclone in the early morning hours of 17th May and further moved to north near to Gujarat coast. Intense rain near to Gujarat and Saurashtra coast is well identified by H-E (Fig. 3.1f). The compact and dense rainfall structure of extremely server cyclone is well marked and most destructive eye wall regions are clearly identified. After landfall on 17th May, cyclone weakened but moved further deep into coast and covered Gujarat region and adjoining Rajasthan on 18th May.

3.4 Validation of H-E rainfall

H-E method based rainfall during TC Tauktae is compared with the IMD surface rainfall observations and IMERG-GPM satellite products.

3.4.1 IMD surface rainfall observation

Tauktae made severe impact on west coast regions (Karnataka, Konkan and Goa, Saurashtra, Gujarat and West Rajasthan) of India. Fig. 3.2 shows H-E rainfall over these district from 12th to 18th May 2021. H-E recorded intense rainfall (>200mm) over the coastal regions from the day when TC gained very severe cyclonic storm category (i.e from 16th May). On 18th May, high rainfall is observed over Gujarat and Saurashtra coast also.

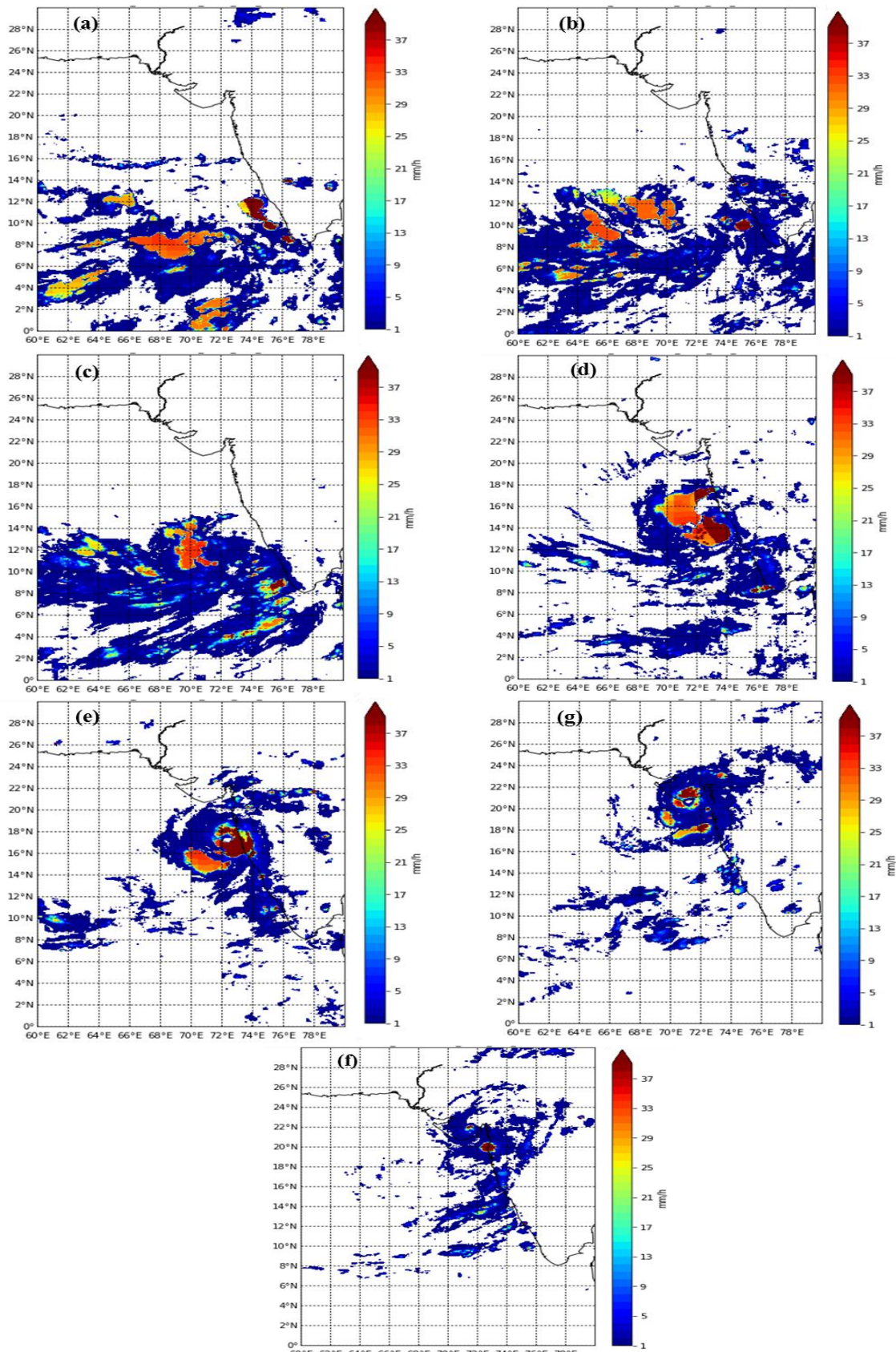


Figure 3.1: Spatial distribution of H-E rain from INSAT-3D on (a) 12th May 2021 at 0100UTC, (b) 13th May 2021 at 1700 UTC, (c) 14th May 2021 at 0500UTC, (d) 15th May 2021 at 059UTC (e) 16th May 2021 at 1259 UTC, (f) 17th May 2021 at 1559 UTC and (g) 18th May 2021 at 0700 UTC.

A comparison of rain from IMD rain gauges stations and H-E on daily scale at $0.25^\circ \times 0.25^\circ$ spatial grid resolution from 12th to 18th May 2021 show a correlation of 0.5. Point to be noted here is that IMD rain gauge observations represents a point measurement whereas, INSAT-3D is average value of 4km spatial resolution.

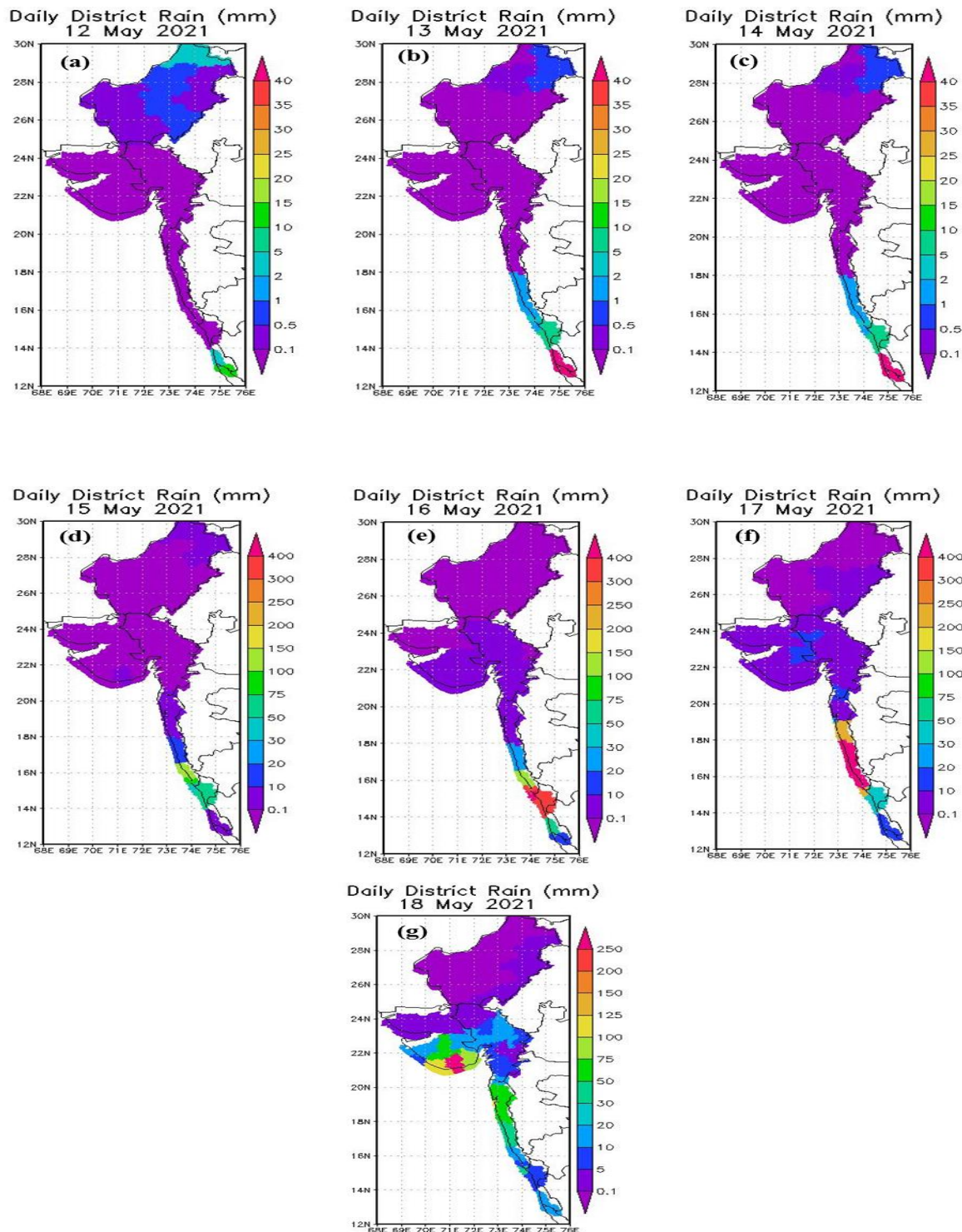


Figure 3.2: Distribution of district averaged daily rain (mm) for 12, 13, 14, 15, 16, 17 and 18 May 2021 associated with Tauktae cyclone from INSAT-3D Hydro-Estimator.

3.4.2 GPM-IMERG rainfall products

Fig. 3.3 (a) and 3.4(b) show rainfall distribution on 17th May 2021 at 0200 UTC recorded by H-E INSAT-3D and GPM-IMERG respectively. H-E well captured extreme cyclonic rain and effectively discriminated destructive eye wall region with warm eye of cyclone. Extreme rain is also recorded well by GPM-IMERG, but it fails to locate warm eye region of cyclone.

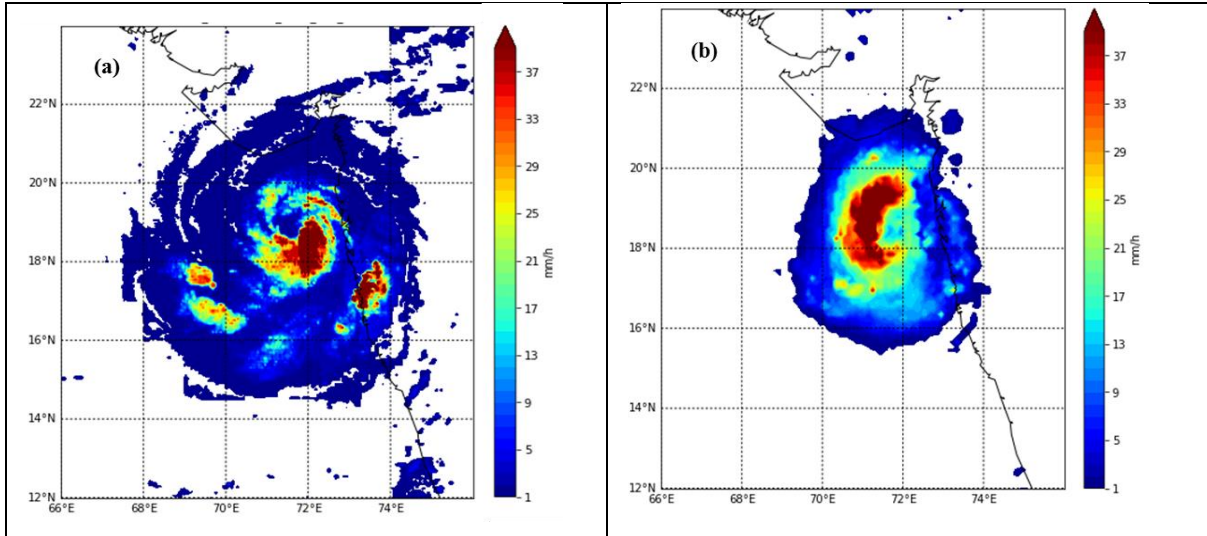


Figure 3.3: Spatial distribution of (a) H-E rain from INSAT-3D and (b) GPM-IMERG on 17th May 2021 at 0200 UTC.

Comparison of rainfall products from H-E and GPM-IMERG on daily scale is also carried out from 12th to 18th May 2021. Since GPM-IMERG rainfall products are available at 0.1x0.1 km spatial grid resolution. Thus, H-E rain is also gridded to same spatial resolution and both the products are compared in TC Tauktae affected region 12°N-30°N and 68°E -76°E. The comparison results show a correlations of 0.59. The comparison shows that H-E compared better with GPM-IMERG product than with IMD gridded product. The reason is that GPM-IMERG and H-E both are spatially averaged products though originally at different resolutions. On the other hand, IMD gridded product is generated using few point measurements from rain gauges. Noteworthy, GPM-IMERG products are late run products that have not calibrated with surface observations.

3.5 Conclusion

Rainfall is one of an important components of TC, which severely affects life and infrastructure of coastal regions. At the time of extremely severe cyclone, such as recent cyclone Tauktae formed in Arabian Sea, its monitoring becomes more significant. H-E method-based rainfall from geostationary satellite INSAT-3D/3DR is successfully captured rainfall from the

depression to dissipation of Tauktae. H-E recorded rain structure of cyclone very well and discriminated the warm eye from destructive eye wall region as well. The rain estimated from H-E shows good agreement with IMD surface observations and GPM-IMERG satellite products with R value of 0.5 and 0.59, respectively. Results infer the reliability and usefulness of H-E rain products from INSAT-3D/3DR in monitoring TC Tauktae rain over ocean and coastal regions as well.

References

1. Kumar P and A K Varma, Assimilation of INSAT-3D Hydro-Estimator Method Retrieved Rainfall on Short Range Weather Prediction, Quarterly Journal of Royal Meteorological Society, 143: 384-394, DOI:10.1002/qj.2929, 2016
2. Rappaport, E.N., 2000: Loss of life in the United States associated with recent Atlantic tropical cyclones. Bulletin of the American Meteorological Society, 81(9), 2065-2073.
3. Sharma, N., and A K Varma, 2020, Preparation of Rain Retrieval Technique for upcoming SSTM onboard OCEANSAT-3: Modified Hydro-Estimator, SAC/EPSA/AOSG/GRD/SR-37/2020, p 9.
4. Webster, P.J., 2008: Myanmar's deadly daffodil. Nature Geoscience, 1, 488-490.

4. Assessment of surface inundation and changes in water turbidity associated with Cyclone

Shard Chander, Amit K. Dubey, Vibhuti B. Jha, Rohit Pradhan,

Nimisha Singh and R.P. Singh

4.1 Introduction

Coastal flooding is one of the most significant risk to life and infrastructure with wide ranging social, economic and environmental impacts. Floods are temporary or permanent inundation of surface and can occupy vast expanses. Cyclones bring high intensity of rainfall with short duration and landmass with low to mild slope is remain vulnerable to flooding. As a tropical cyclone approaches land, its impact leads to a rise in water level at the coast that can be extremely severe inundating vast low lying areas. Second, flooding from rainfall can also occur in conjunction. These events induced flash floods influence many low-lying areas in the coastal regions and changes the turbidity of the wetlands. Rise in sea levels, extreme groundwater withdrawal rates, land surface deformation, land use and land cover have further intensified the impact and extent of inundation following land falling tropical cyclones. Rivers get swollen due to incessant rain under the influence of cyclone. The traditional monitoring of river gauges is limited to few locations over a river basin. Worldwide, the number of operational stations has been decreasing continuously. Remote sensing techniques are an effective source of information to understand various hydrological aspects related with the cyclone induced flooding and so can be effectively used to map inundated areas with sufficient temporal and spatial resolution. Space borne measurements of terrestrial surface water has the capability that can address some pivotal questions, which the in situ measurements find hard to answer.

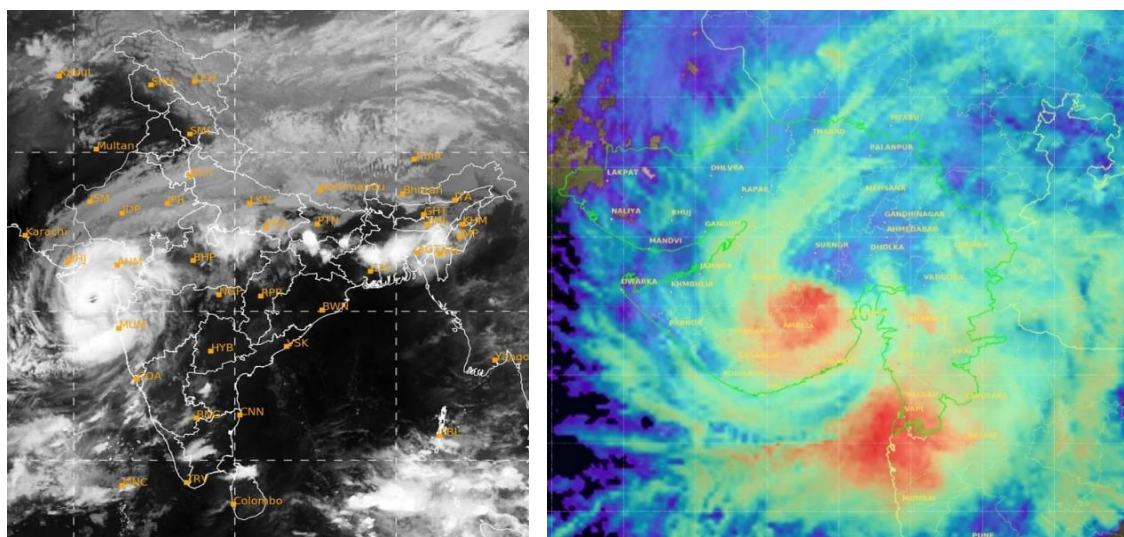


Figure 4.1: INSAT-3D image during landfall of TC Tauktae on 17 May 2021

Extremely Severe Cyclonic Storm Tauktae was a powerful tropical cyclone in the Arabian Sea that became the strongest tropical cyclone to make landfall in Gujarat since 1998 and one of the strongest tropical cyclone to ever affect the west coast of India. Cyclone Tauktae had affected the Indian states of Kerala, Gujarat, Maharashtra, Goa and Karnataka, along with two

Union Territories: Daman & Diu and Lakshadweep. Heavy rain due to Cyclone Tauktae created flood like situation in many parts of Gujarat including the coastal districts of Amreli and Bhavnagar along with Rajkot, Botad, Ahmedabad and Surat. Effects of Cyclone Tauktae were felt inland, including Northern regions of Madhya Pradesh and parts of Uttar Pradesh as well. Cyclone brought heavy rainfall and surface inundation to areas along the coast and caused widespread infrastructure and agricultural damage to the western coast of India. Accumulated rainfall showed a high amount (> 75 mm) of precipitation received at the landfall location in Gujarat on May 17 2021.

4.2 Data Used

Surface inundation was estimated using synthetic aperture radar Sentinel-1 and Advanced Microwave Scanning Radiometer AMSR-2 dataset. Optical dataset of Sentinel-2 was analysed to understand the changes in the turbidity of the nearby rivers and lakes.

Table 4.1: Dataset used to carry out assessment of Cyclone TAUKTAE

Satellite	Sensor	Spatial Resolution	Temporal Resolution
Sentinel-1	Microwave Synthetic aperture radar- C band	10 m	12 days (6 days for Sentinel 1A and 1B)
AMSR-2	Passive Microwave Radiometer	0.1 degree	1-2 days
Sentinel-2	Optical Multispectral 12 bands (440-2200 nm)	10 m 20 m 60 m	10 days (5 days for Sentinel 2A and 2B)

4.3 Analysis of Cyclone Induced Flooding using Hydrological Modelling

SACHYDRO model is a deterministic, distributed and unsteady flow model. It is developed to simulate the hydrological fluxes at regional scale (5x5 km grid). The model takes care of several hydrological processes such as infiltration, surface runoff, evapotranspiration, runoff routing and snow melt runoff within the catchment. These hydrological processes are divided into different modules and linked in a synergistic way so that maximum space based inputs can be ingested into modeling framework. To solve different hydrological processes in these modules, data set such as meteorological parameters from weather models and remote sensing data products for land surface variables are taken. Energy budget component of the model is solved using Weather Research and Forecasting (WRF) simulated fluxes. Remote sensing products such as vegetation fraction, Leaf Area Index (LAI), Snow cover, Albedo are ingested in the model. To perform hydrological simulations meteorological parameters such as temperature, wind speed, relative humidity and radiation fluxes are extracted from WRF

forecast. WRF forecast of 24 hr were considered for the data set preparations with spatial resolution of 5 km. Rainfall and Snow cover was taken from satellite derived product interpolated into model grid. To perform the surface and sub-surface water partitioning Green-Ampt infiltration equation was used in the model. Green-Ampt equation over slopes was adopted here to estimate the infiltration rate Green Ampt infiltration parameters (soil porosity, saturated hydraulic conductivity, suction head) are used from the relations developed between soil texture and their hydraulic properties. To estimate snowmelt depth energy budget approach is adopted in the model. The major component of energy budget approach is radiation fluxes (shortwave and longwave radiation), turbulent fluxes (convective and latent heat flux) and ground heat flux. To estimate the inundation probability a functional relationship is established between surface runoff and the topography (Dubey et al. 2021). Since, cyclones bring high intensity of rainfall with short duration it generates instantaneous flooding conditions at low lying regions of coastal areas. Landmass with low to mild slope is also remain vulnerable to flooding due to high intensity of rainfall. These characteristics of cyclones are utilized here to derived flood inundation probability. Surface runoff is scaled to 0 to 1 based on amount of surface runoff and topography slope is also converted into 0 to 1 scale. By combining these two variables flood inundation probability is derived for the cyclone induced flooding (Fig. 4.2).

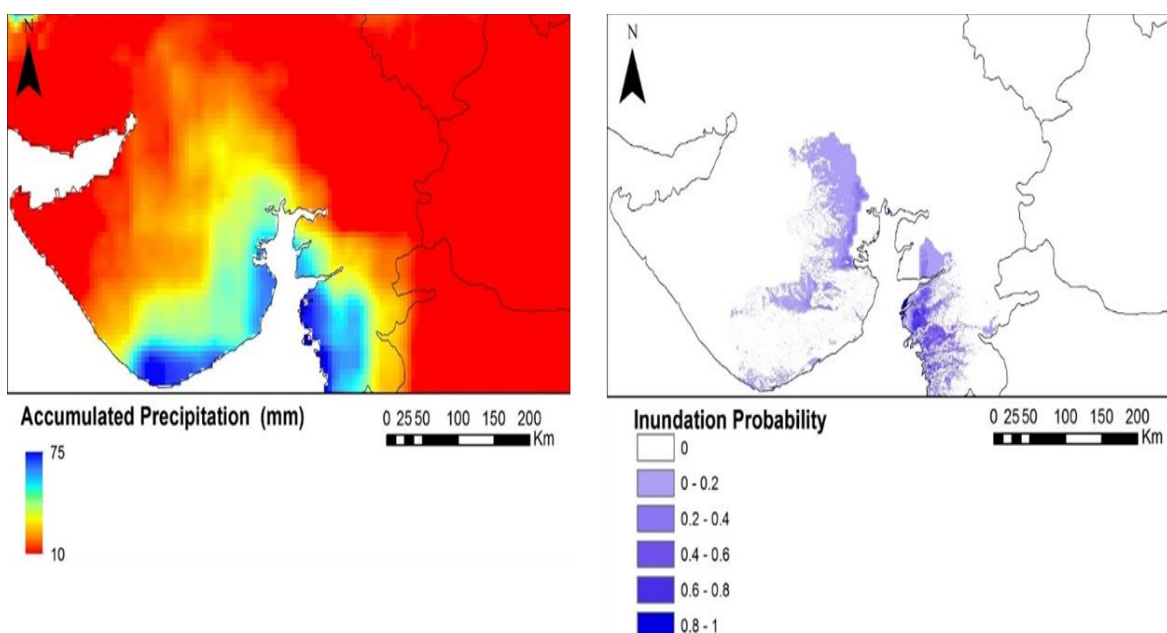


Figure 4.2: Cumulative precipitation and Inundation probability during Cyclone Tauktae (17 May 2021)

Hydrological modelling of Tauktae cyclone was carried out to identify the high flood prone region. The satellite rainfall product and WRF meteorological forecast was used for Hydrological modelling. Accumulated rainfall (Fig. 4.2) showing high amount (> 75 mm) of

precipitation received at the landfall location in Gujarat on May 17 2021. Rainfall and high wind speed affected the many parts of Kerala, Gujarat and Maharashtra state. Cyclonic rainfall also caused the inundation in different regions of these states. High amount of precipitation was observed at the landfall location in Gujarat state as highlighted by the satellite rainfall which, generated high inundation probability for the low-lying region of the state.

4.4 Surface Inundation mapping using SAR

Synthetic Aperture Radars like RISAT, Sentinel-1 prove very useful in delineating inundated regions during cyclones and floods. For flood mapping SAR has the advantage to penetrate cloud cover and remains largely un affected by adverse weather conditions that often persist during flood events. SAR sensors emit electromagnetic pulses in the microwave region and receive the signal returned from the surface, termed as backscatter, in the form of amplitude and phase. The backscatter signal from a surface depends on the sensor parameters (wavelength and polarisation) and other parameters like dielectric constant, the geometry of the target, and surface roughness. The flooded regions appear dark with varying shades depending on the underlying heterogeneity and wind conditions. Therefore, the general idea is to find low backscatter regions in the SAR image that generally act as specular reflectors thus appearing as dark areas.

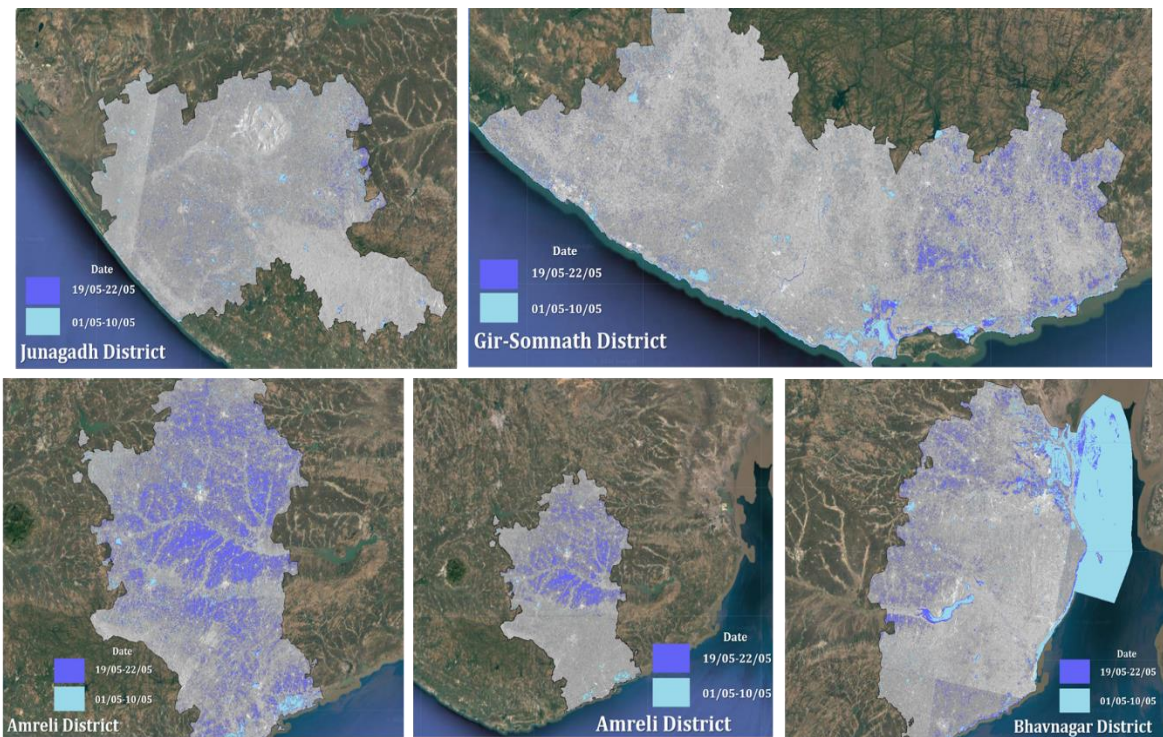


Figure 4.3: Inundation after Cyclone Tauktae in the Junagarh, Gir-Somnath, Amreli, Ahmedabad and Bhavnagar district, Gujarat using Sentinel-1 C band 10 m spatial resolution dataset

Inundation maps using Sentinel-1, C band SAR are prepared after Cyclone Tauktae in the Western Coast of India as shown in Fig. 4.3. The post cyclone flooding was carried out on datasets of the period 19th – 22nd May in comparison to pre-cyclone period 1st-10th May 2021 for cyclone Tauktae. The regional threshold was determined based on the histogram backscatter values to delineate the still water surface and quasi inundated areas. Heavy flooding was observed in the coastal districts of Gujarat. District wise analysis of inundated surface area was also carried out at 10 m spatial resolution and is shown in Table 4.2. Amreli district was the worst affected (29 %) among other district, i.e. Gir, Junagadh, Porbandar and Bhavnagar.

Table 4.2. Inundated area in affected districts after Cyclone Tauktae

District	Inundated Area Post	Percentage of total area
	Cyclone (sq.km)	
Gir	155	6 %
Junagadh	286	4 %
Porbandar	118	5 %
Amreli	2100	29 %
Bhavnagar	960	12 %

4.5 Surface Inundation mapping using Microwave Radiometry

Microwave indices obtained from multi-frequency radiometry have been used in detecting characteristics of land and water surfaces (Paloscia et al., 2018). Brightness Temperature Polarization Ratio (PR), also known as Microwave Polarisation Difference Index (MPDI), at a particular frequency is one such index that is used to study soil moisture, surface inundation and vegetation characteristics (Gupta et al., 2019; Njoku et al., 2003; Zheng et al., 2016). Generally, wet soil that has high soil moisture is associated with high dielectric constant and lower emissivity. Hence High soil moisture reduces the brightness temperature. This principle is used to derive surface inundation during cyclones and floods. Further to improve the temporal period of the analysis radiometry brightness temperature (BT) difference at 36 GHz from Advanced Microwave Scanning Radiometer (AMSR2) at 0.1-degree spatial resolution was utilized for estimating the inundated areas at a much finer temporal resolution. This frequency is suitable to assess surface flooding and avoid signals due to wet soil. Although microwave radiometers have a coarse resolution, it provides repeat observations of the entire country with 1-2-day repetitivity, which makes it suitable for analysis of regional scale inundation from extreme events.

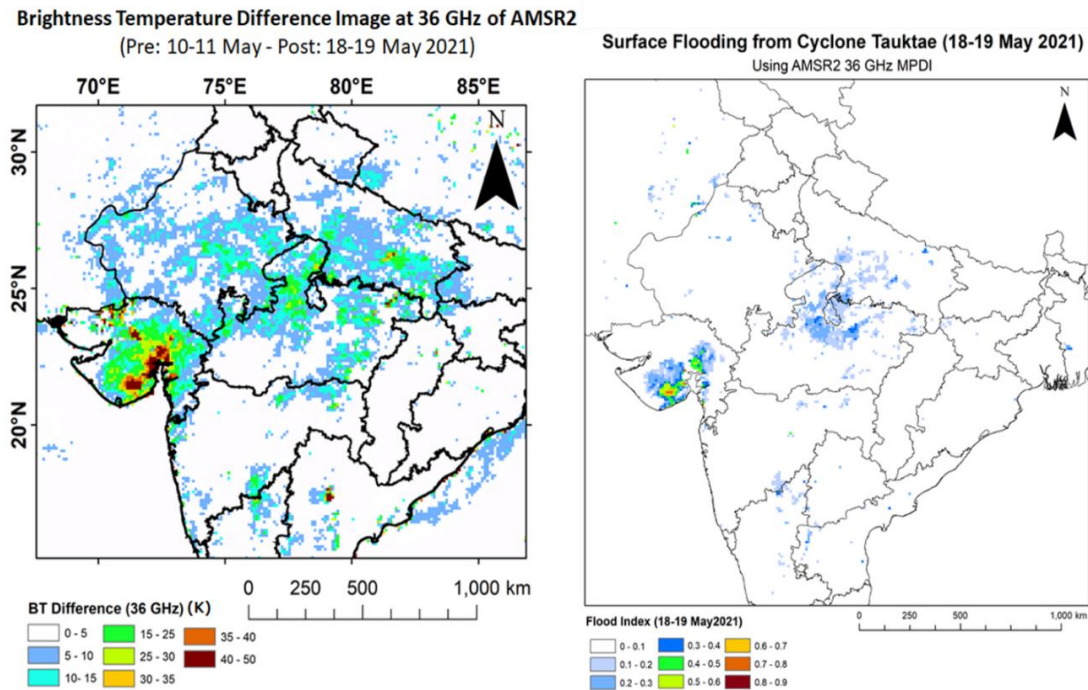


Figure 4.4: Surface flooding map after Cyclone Tauktae using AMSR -2 36 GHz dataset

Long-term MDPI statistics (mean and standard deviation) was computed using AMSR-2 36 GHz Brightness temperature dataset. Water bodies and inundated regions show high value of MPDI. Desert regions and barren land too have high MPDI and these needs to be separated from the true flood signal using LULC maps and appropriate thresholds. Flood Index for pixels with MPDI in the range of 0.01 and 0.1 is computed on a linear scale of 0 to 1. Pixels with $\text{MPDI} < 0.01$ are represented as non-flooded. AMSR2 36GHz MPDI based flood index maps were generated for Cyclone Tauktae during 18-19 May 2021. Heavy rain due to Cyclone Tauktae created flood like situation in many parts of Gujarat including the coastal districts of Amreli and Bhavnagar along with Rajkot, Botad, Ahmedabad and Surat. Effects of Cyclone Tauktae were felt inland, including Northern regions of Madhya Pradesh and parts of Uttar Pradesh as well. This led to reduction in BTh in the region and flooded pixels were picked up using MPDI based flood index maps (Fig. 4.4).

4.6 Impact assessment of Water Quality using optical dataset:

Inland waters are among the most productive natural systems on earth. The maintenance of quality of the coastal and inland waters is essential for any country as they support the day-to-day activities of the people and the economic growth activities such as fishing, transport, agriculture, industry and recreation. Extreme events like cyclones, floods brings a large amount of nutrients from distinct origin and changes the water quality in nearby wetlands. Turbidity is one of the important water quality parameter can be detected in the optical multispectral dataset

(Chander et al. 2019). In the present work, cloud free images of Sentinel-2 at 10 m spatial resolution is used to understand the changes in turbidity levels during pre (7 May) and post (22 May) cyclonic event. As seen in Fig. 4.5, significant increase in turbidity was observed in a water body near Palitana within a span of few days in comparison to pre cyclone time.

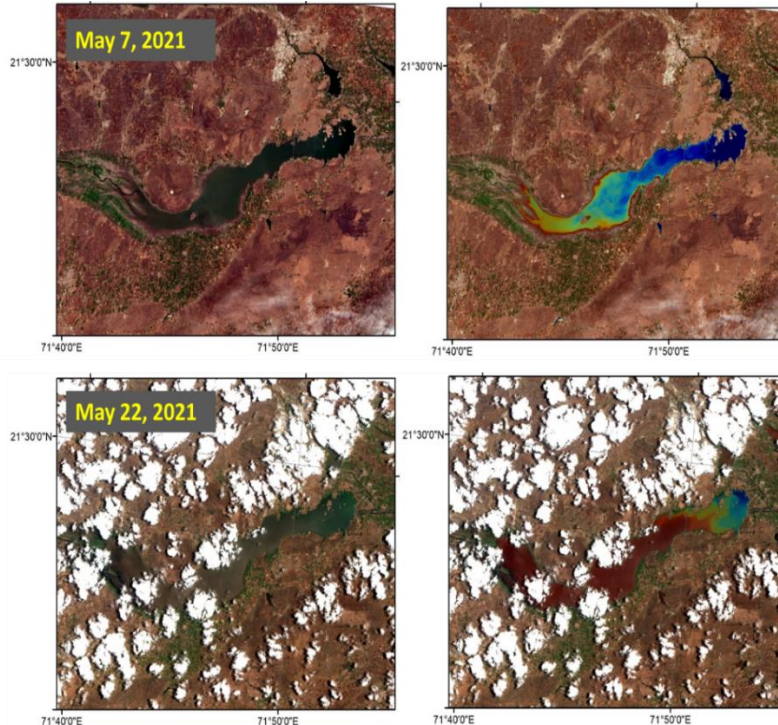


Figure 4.5: Natural colour composite and derived turbidity variation during pre and post cyclone at the East coast of India using Sentinel-2 multispectral dataset of 10 m spatial resolution

4.7 Conclusion

Present section of report provides a detail overview of hydrological aspects analysed with the help of remote sensing dataset associated with Cyclone Tauktae. Heavy rain due to Cyclone Tauktae created flood like situation in many parts of Gujarat including the coastal districts of Amreli and Bhavnagar along with Rajkot, Botad, Ahmedabad and Surat. District wise analysis of inundated surface area was also carried out at 10 m spatial resolution. Amreli district was the worst affected (29 %) among other district, i.e. Gir, Junagadh, Porbandar and Bhavnagar. Effects of Cyclone Tauktae were felt inland, including Northern regions of Madhya Pradesh and parts of Uttar Pradesh as well. Significant increase in turbidity was also observed in many inland water bodies. Better understanding of these hydrological aspects can further help to outline the susceptibility of different localities to potential floods based on analyses of the impacts from earlier events.

References

1. Chander S., Gujrati A., Hakeem A., Garg V., Issac M., Dhote P. K. and Sahay A. (2019). Water quality assessment of river Ganga and Chilika lagoon using AVIRIS-NG hyperspectral data. *Current Science*, 116 (7), pp 1172- 1181.
2. Dubey A. K., Kumar P., Chembolu V., Dutta S., Singh R. P. and Rajawat A. S. (2021), Flood modeling of a large transboundary river using WRF-Hydro and microwave remote sensing, *Journal of Hydrology*, 598, 126391.
3. Gupta, P.K., Pradhan, R., Singh, R. P. and Misra, A. (2019). Scatterometry for land hydrology science and its applications. *Current Science*, 117(6), 1014-1021.
4. Njoku, E. G., et al. (2003). Soil moisture retrieval from AMSR-E, *IEEE Trans. Geosci. Remote Sens.*, 41, 215–229.
5. Paloscia, S., Pampaloni, P., and Santi, E. (2018). Radiometric Microwave Indices for Remote Sensing of Land Surfaces, *Remote Sens*, 10, 1859.
6. Zheng, W., Sun, D. and Li, S. (2016). Coastal flood monitoring based on AMSR-E data. *IEEE International Geoscience and Remote Sensing Symposium (IGARSS)*, Beijing, 4399-4401. DOI: 10.1109/IGARSS.2016.7730146.

5. Impact of Cyclone on coastal-ocean biological productivity

Debojyoti Ganguly, R.K. Sarangi, N. Jaiganesh, Arvind Sahay

5.1 Introduction

Tropical cyclones can have profound influence on the biological productivity of the marine ecosystem. The strong winds produces two kinds of dynamic responses in the upper ocean, namely turbulent mixing and upwelling, both of which can induce a decrease of sea surface temperature (Pan et al. 2018). The wind stress and the rotating wind system can cause nutrients from below the mixed layer to be uplifted to the surface, a process called upwelling, thus enhancing the biological productivity. Upwelling, which is driven by the wind stress curl, is the most important process causing density changes in the thermocline through divergence of upper layer transport (Dickey et al. 1998). In this study, we investigate the impact of extremely severe cyclonic storm Tauktae on the oceanic parameters like SST, Sea Level anomaly (SLA) and chlorophyll concentration.

5.2 Data Used

Parameters	satellite/data source	Scale/Product resolution	Source link
Chlorophyll concentration (Chl, mg m ⁻³)	ESA's GlobColor project – merged data – weighted average of MODIS AQUA, VIIRS and OLCI data (optical channels, 400-700 nm) Ocean Colour Monitor (OCM-2) Local Area Coverage data	Globcolor: Daily/8day 4 Km OCM-2 : daily -360 m	https://hermes.acri.fr http://10.61.143.36:8080/SDIS_2.0/
Sea Surface Temperature (SST, °C)	Global High Resolution Sea Surface temperature (GHRSST)	Daily-4km	http://apdrc.soest.hawaii.edu
Sea Level Anomaly (SLA, cm) and surface currents	AVISO product - processed data from all altimeter missions: Jason-3, Sentinel-3A, HY-2A, Saral/AltiKa, Cryosat-2, Jason-2, Jason-1, T/P, ENVISAT, GFO, ERS1/2	Daily – 25 Km	https://resources.marine.copernicus.eu/
Wind velocity(m/s) and direction	Advanced Scatterometer (ASCAT)	Daily-25km	http://apdrc.soest.hawaii.edu

5.3 Methodology

- Wind stress and Ekman suction velocity are computed on a daily basis from 17 May 2021 to 9 June 2021 using following equations:

$$\tau = \rho \omega * C_d * W^2. \quad (1)$$

$$v = \frac{\nabla \times \tau}{\rho f}. \quad (2)$$

Where τ is the wind stress, ρ is the density of water and f is the Coriolis parameter, ω is the density of air taken as 1.25 kg/m^3 , W is the wind speed and C_d is the wind dependent drag coefficient given by (Sun et al. 2010).

$$C_d = (0.73 + 0.069W) * 10^{-3} \quad (3)$$

- Daily SST data from GHRSST is procured from the period 17 May 2021 to 9 June 2021 and 8-day composites generated for the 24-day period.
- 8-day composite images of chlorophyll are obtained from Globcolor multi-sensor merged products from 17 May 2021 to 9 June 2021. Single day OCM-2 Local Area Coverage (LAC) images from 17 May to 31 May are also obtained. OCM-2 data are processed for atmospheric correction and chlorophyll is obtained from remote sensing reflectance using OC2 algorithm (O'Reilly et al. 1998; O'Reilly et al. 2019).
- 8-day composites of sea level anomaly (SLA) and geostrophic current velocity components have been generated and current vectors overlaid on SLA data. Mesoscale eddies appear as rotating (clockwise or anticlockwise) vortices with depressed or elevated sea surface heights. Eddies are detected using outermost closed contours of sea level anomalies using the methodology of Faghmous et al. (2015).
- Every 6-hour position of cyclone track point is obtained from Indian Meteorological Department (IMD). Cyclone translation speed is calculated as the average speed during the 6-hour period from the 6-hour track position.
- The thermocline displacement due to the cyclonic wind stress is computed along cyclone track using the following equation (Price et al. 1994; Walker et al. 2005).

$$\eta = \frac{\tau}{\rho * f * U_T} \quad (4)$$

Where, η is the thermocline depth (in metres), τ is the wind stress, ρ is the water density, f is the Coriolis parameter and U_T is cyclone translation

5.4 Results

The data are divided into three 8-day periods. The first 8-day period from 9-16 May, 2021 is the pre-cyclone period. The next 8-day period from 17 May to 24 May, 2021 is during cyclone period and the following 8-day period from 25 May to 1 June, 2021 is the post-cyclone period. SST, chlorophyll and sea level anomaly are analysed for each of these three periods. Ekman suction velocity is analysed during all these three periods using 5-day averaged products. In Tauktae, 5-day averages are considered because the cyclonic storm was active only for 5 days (14-18 May 2021) and 8-day averaged data was unable to pick up the cyclone induced wind stress curl. The pre-Tauktae, during Tauktae and post-Tauktae Ekman suction velocities are shown in Fig. 5.1.

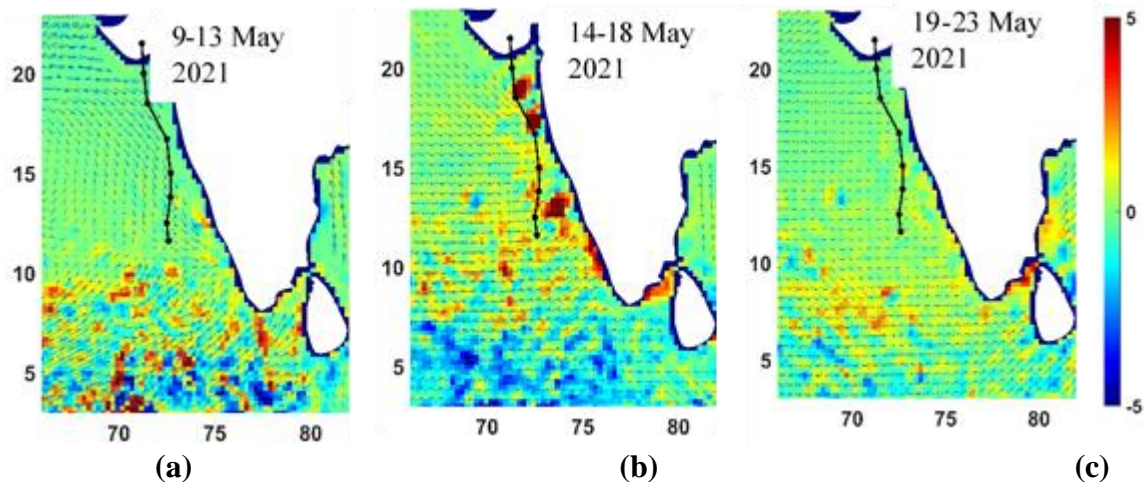


Figure 5.1: (a) Ekman suction velocity(m/d) during 9-13 May 2021 (Pre Tauktae), (b) Ekman suction velocity(m/d) during 14-18 May 2021 (during Tauktae), (c) Ekman suction velocity during 19-23 May 2021 (post Tauktae).

It can be observed from Fig. 5.1 that the period from 14-18 May is characterized by high Ekman suction velocities ranging around 5m/day. The rotating storm system causes Ekman mass divergence and upwelling due to the wind stress curl. Ekman suction velocities in pre- and post cyclone period are significantly lower (<1m/day).

The 8-day composite SST, SLA and chlorophyll for pre-Tauktae, during Tauktae and post Tauktae period are shown in Fig. 5.3.

An increase in chlorophyll concentration (CC) in the 8-day average chlorophyll image (Fig. 5.3i) was observed in the aftermath of the Tauktae cyclone in the northeast Arabian Sea. The mean CC computed in a rectangular region (Fig. 5.3g) centred over the cyclone track in the three sequential 8-day images was observed to be 0.284, 0.277 and 0.371. Similarly, a decrease in SST has been observed following the passage of Tauktae. The SST mean for the 3 sequential 8-day images have been observed as 30.69, 29.9 and 29.7°C for the Arabian Sea region (Fig. 5.3a-c). The SST warming and increase was seen in the 1st image, just before the cyclone had

its landfall on 18th May 2021. Subsequently, in the 2nd week, a decrease in SST, in the range 29.8 to 30.6°C (Fig. 5.3 b,c) was observed. The SST dropped further in the proceeding week. The drop in SST is due to cyclone induced turbulent mixing and entrainment.

To investigate the change in chlorophyll after the cyclonic event images of pre-cyclone and post-cyclone period were analysed by differencing. The difference images are shown in Fig. 5.4. It was observed that average chlorophyll increased by 0.07 mg/m³ during May 17-24 and by 0.15 mg/m³ during May 25-June 1.

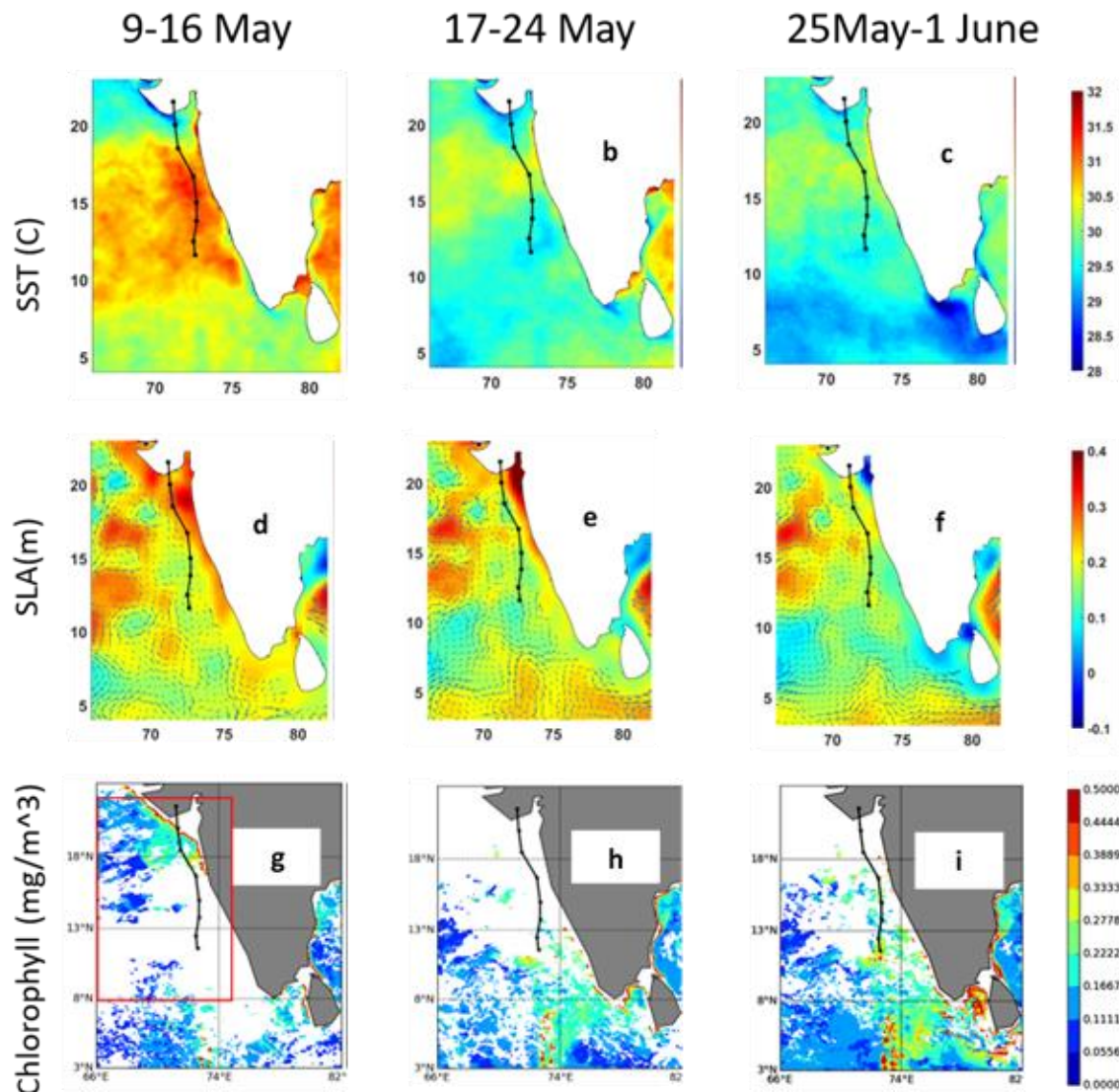


Figure 5.2: SST, SLA and chlorophyll concentration (mg/m³) for pre Tauktae period (9-16 May 2021), during Tauktae period (17-24 May 2021) and post Tauktae period (25 May-1 Jun 2021).

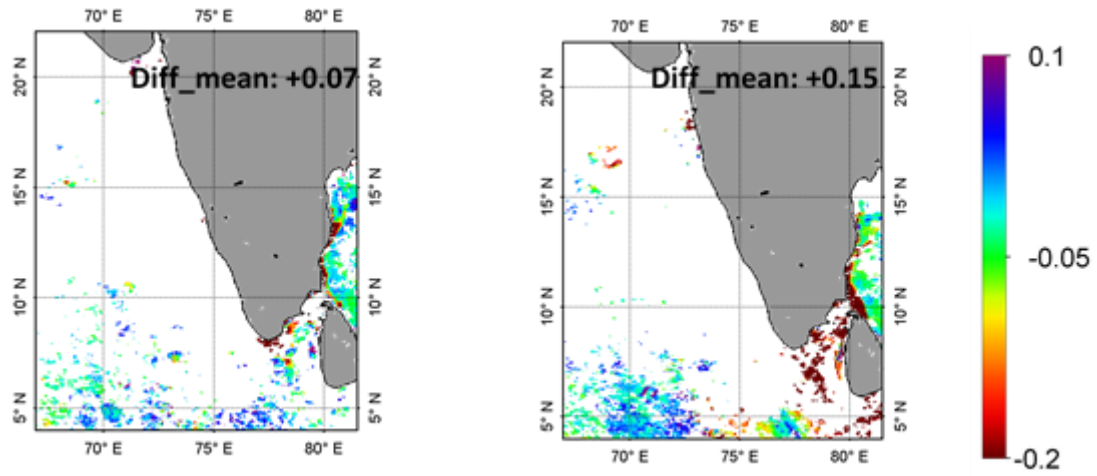


Figure 5.3: (a) Chlorophyll difference image (May 17_24 – May 9_16), (b) Chlorophyll difference image (May 25_June 01 – May 9_16)

The average Chlorophyll and SST from May 1 to June 9, 2021 over the rectangular region (Fig. 5.3g) are shown in the form of bar plots in Fig. 5.5 (below).

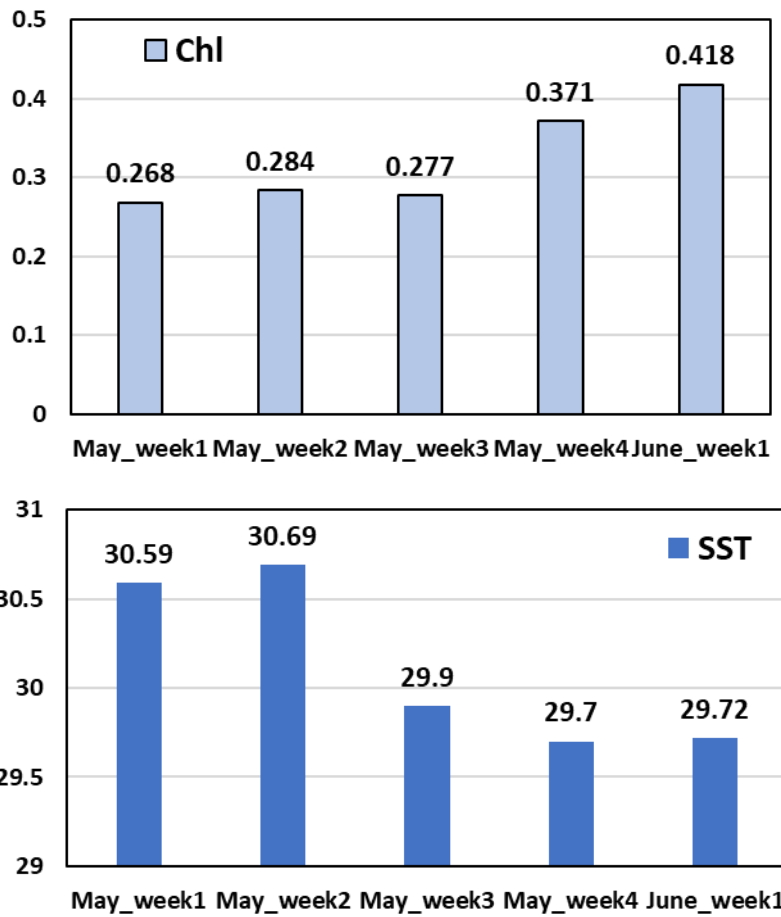


Figure 5.4: (a) 8-day average chlorophyll from May 1, 2021 to June 9, 2021, (b) 8-day average SST from May 1, 2021 to June 9, 2021

From Fig. 5.4, it is observed that the minimum SST of 29.70C was observed in the post cyclone week (May 25-1 June 2021) and maximum SST of 30.690C was observed just before the

cyclonic storm in 2nd week of May (May 9-16). Thus, average SST drop of around 20C was observed after the passage of Tauktae. Chlorophyll concentration in the rectangular box ranged between 0.268 to 0.284 mg/m³ before the passage of Tauktae, which increased to 0.371 mg/m³ during 4th week of May and further increased to 0.418 mg/m³ during June 1-8.

5.4.1 Chlorophyll from Ocean Color Monitor (OCM-2) imagery before and after cyclone

We investigated OCM-2 single day passes over Arabian Sea in order to assess if chlorophyll data could be obtained due to higher spatial resolution of OCM-2 (360 m). OCM-2 scenes before and after cyclone Tauktae were inspected for cloud-free data availability. Finally, two scenes were selected, one dated 10 May, 2021 and other dated 20 May, 2021. The OCM-2 scenes are processed and chlorophyll are retrieved using OC-2 algorithm (O'Reilly et al. 1998; O'Reilly et al. 2019). The true color images are shown in Fig. 5.5.

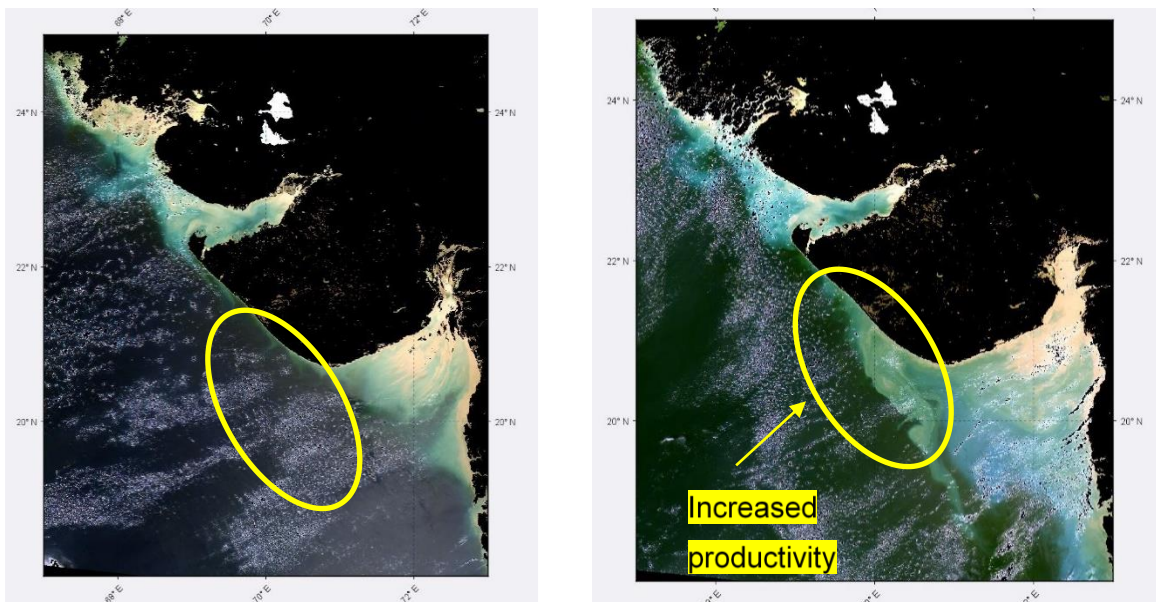


Figure 5.5: OCM-2 true colour radiance images before and after Tauktae.

Highly productive (bloom like features) can be distinctly seen in coastal waters of Gujarat and Maharashtra after the passage of Tauktae. A plume like feature of phytoplankton bloom can be seen spreading out from coastal regions of Porbandar up to offshore waters of Mumbai. The processed chlorophyll images are shown in Fig. 5.6.

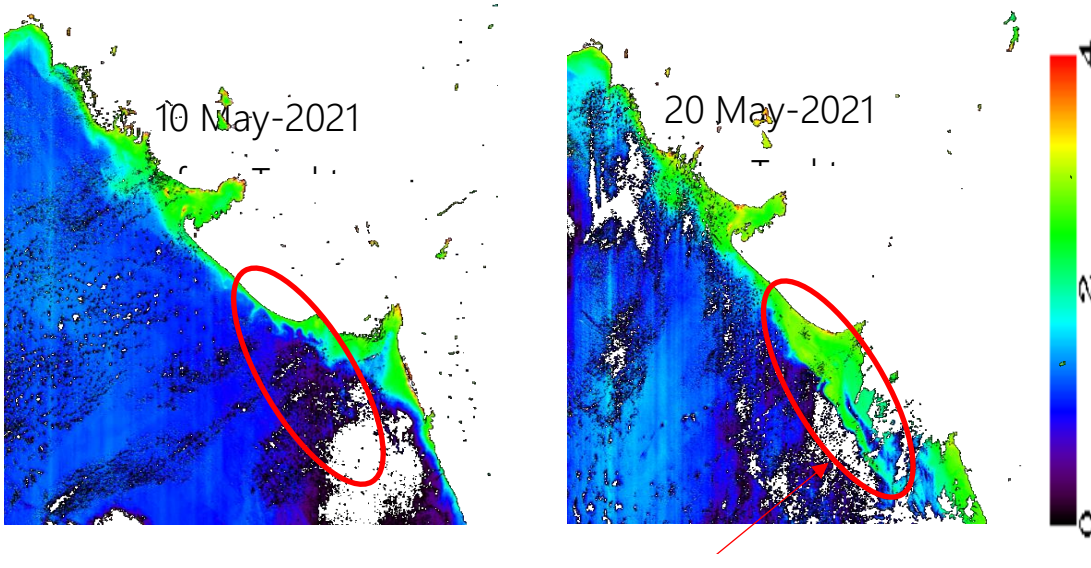


Figure 5.6: OCM-2 derived chlorophyll concentration (mg/m^3) before and after Tauktae.

A coastal patch of increased chlorophyll concentration is observed in the 20 May OCM-2 imagery. This patch extends in a linear ribbon like fashion all along the coast extending from coastal regions near Porbandar, Gujarat up to Northern Maharashtra. Even though upwelling velocities of 4-5 m/day are observed at many regions along the cyclone track, increased chlorophyll concentrations are only observed near coastal areas of Gujarat and northern Maharashtra. This needs more investigation.

5.5 Discussion

Sarangi et al. 2015 reported that for cyclone Phailin, the post-cyclone chlorophyll was around $0.80\text{--}1.50 \text{ mg}/\text{m}^3$ in the offshore water, which was quite high as compared to pre-cyclone concentration ($<0.60 \text{ mg}/\text{m}^3$). Ganguly et al. 2020 reported 300-500 percent increase in chlorophyll concentration in Arabian Sea following the passage of Ockhi. Subrahmanyam et al. 2002 reported very high chlorophyll concentrations ($5\text{--}8 \text{ mg}/\text{m}^3$) in the Arabian Sea after the passage of a tropical cyclone during 21-28 May 2001. Byju and Kumar 2011 reported an average chlorophyll enhancement of $0.5 \text{ mg}/\text{m}^3$ and SST drop of 2°C in Arabian Sea following the passage of cyclone Phyan. The chlorophyll increase for cyclone Tauktae ranged between 100-200 percent in the coastal regions of Gujarat to up to 40 percent in open ocean regions.

The post cyclone increase in chlorophyll depends on a number of factors like upper layer stratification, depth of nitracline, cyclone translation speed and pre-existing oceanic eddies apart from the cyclonic wind stress. The cyclone related changes in biological productivity needs be investigated in light of above-mentioned facts.

5.6 Conclusion

- Upwelling velocity of ~5 m/day was observed during Cyclone tauktae. This dropped to less than 1 m/day in the post landfall week. SST decrease of up to 2.-3°C was observed in daily data.
- A coastal patch of increased biological productivity was observed near coastal regions of Gujarat and northern Maharashtra in daily OCM-2 imagery. This patch spread in a linear plume like pattern along the coast. This bloom like feature was absent in pre Tauktae image.
- Thermocline upward displacement of up to 20m was observed along the track confirming cyclone induced upwelling.

References

1. Byju, P., Kumar, S.P. 2011. Physical and biological response of the Arabian Sea to tropical cyclone Phyan and its implications, *Marine Environmental Research*, 71 :325-330.
2. Dickey, T., D. Frye, J. McNeil, D. Manov, N. Nelson, D. Sigurdson, H. Jannasch, D. Siegel, T. Michaels and R. Johnson. 1998. Upper-ocean temperature response to Hurricane Felix as measured by the Bermuda Testbed Mooring. *Monthly Weather Review*. 126: 1195–1201.doi: 10.1175/1520-0493,126<1195:UOTRTH>2.0.CO;2.
3. Ganguly, D., K. Suryanarayana, and M. Raman. 2020. Cyclone Ockhi induced upwelling and associated changes in biological productivity in Arabian Sea. *Marine Geodes.* 44 (1): 70-89.
4. Maneesha, K., et al., 2011, Meso-scale atmospheric events promote phytoplankton blooms in the coastal Bay of Bengal, *J. Earth Syst. Sci.*, vol. 120, no. 4, pp. 773–782.
5. O'Reilly, J.E., Maritorena, S., Mitchell, B.G., Siegel, D.A., Carder, K.L., Garver, S.A., Kahru, M., and McClain, C. 1998. Ocean color chlorophyll algorithms for SeaWifs. *Journal of Geophysical Research*. 103 (C11): 24937-24953.

6. O'Reilly, J.E., and Werdell, P.J. 2019. Chlorophyll algorithms for ocean color sensors- OC4, OC5 & OC6. *Remote Sensing of Environment*. 229: 32-47.
7. Pan J., L. Huang, A.T. Devlin, and H. Lin. 2018. Quantification of Typhoon-Induced Phytoplankton Blooms Using Satellite Multi-Sensor Data. *Remote Sensing*. 10.318.doi: 10.3390/rs10020318.
8. Price, J.F. 1981. Upper ocean response to a hurricane. *Journal of Physical Oceanography*. 11: 153–175. doi: 10.1175/1520-0485(1981)011<0153:UORTAH>2.0.CO;2.
9. Sarangi, R.K., Mishra, M. and Chauhan, P., 2015, Remote Sensing Observations on Impact of Phailin Cyclone on Phytoplankton Distribution in Northern Bay of Bengal, *IEEE Journal of Selected Topics in Applied Earth Observations and Remote Sensing*, 8(2):539-549. doi:10.1109/JSTARS.2014.2347036, February 2015.
10. Subrahmanyam, B., Rao, K.H., Rao, N.S., Murty, V.S.N., and Sharp, R.J. 2002. Influence of a tropical cyclone on Chlorophyll-a Concentration in the Arabian Sea, *Geophysical Research Letters*, 29 (22): 22-1-22-4.

6. Damage Assessment of Agricultural and Horticultural crops using Opti-SAR data over Saurashtra region of Gujarat caused by cyclone

**Ayan Das, Mukesh Kumar, Saroj Maity, Mehul R. Pandya and
Bimal K. Bhattacharya**

6.1 Introduction

Agriculture sector in India faces severe challenges in the form of natural disasters like cyclones resulting in crop damage and reduced crop productivity. Natural disasters like cyclones result in heavy rainfall thereby causing flood in the vicinity. It also accompanies with major storms and heavy wind in addition to flood and it is highly detrimental to agricultural and horticultural crops like mango, coconut and banana. The cyclone and its associated flood incidence cause severe damage to agriculture in several ways. The crops get affected in terms of both establishment and productivity. The stagnation of water inside the crop fields result in crop damage. The pulses, oil seeds, and vegetable crops are highly susceptible to flood and the flood results in complete crop loss. Cyclone associated floodwater also brings sand and silt along with it to the crop fields and thereby resulting in change in soil physical condition. The orchard crops are mainly affected by heavy storms that cause uprooting of trees and dropping of fruits.

Tauktae was only the second ‘Extremely Severe Cyclone’ category storm to hit Gujarat in 23 years. The cyclone made its landfall east of Diu on May 17 with wind speed ranging between 160-170km/hr gusting to 185 km/hr. Cyclone track has been depicted in Fig. 6.1. Winds of that strength can easily uproot trees and cause damage to standing crops. The main districts in Saurashtra region that got affected by cyclone Tauktae were Amreli, Gir Somnath, Bhavnagar, Junagadh, Botad, Rajkot, Porbandar and Jamnagar. It had also affected crops in South Gujarat districts of Navsari, Surat, Valsad and Bharuch. The major crops that got affected were Bajra, Sesame, Green gram, Black gram, Guar gum and summer paddy while main horticultural crops that got affected were Mango, Banana, Coconut, Chickoo, Lemon and Guava.

Google Earth Engine (GEE) is a cloud-based computing platform, where users can analyze all available remotely sensed images using a web-based Integrated Development Environment (IDE) code editor without downloading these data to the local machine. With routine data acquisition and calibration, Sentinel 1 and 2 provide a consistent and reliable data source for spatial and temporal comparisons of vegetation conditions. Among numerous vegetation indices from optical bands, NDVI is the most commonly used for vegetation studies, and has a strong correlation to the presence and density of green vegetation. NDVI changes with different phenological stages and vegetation density. Its disparity in the spatial domain may simply indicate different vegetation composition or structure, and intra-seasonal difference may be a result of vegetation status between

two successive growth stages or two different time frames. Vegetation anomaly can be defined, specifically, as the significant change of vegetation vigor due to sporadic events, either naturally or anthropogenically-induced. Such change of vegetation vigor is expressed as the inter-seasonal difference of NDVI, with temporal (seasonal) and spatial coincidence which can be used to assess the damage caused by these events. On the other inter-seasonal comparison of synthetic aperture radar (SAR) data provides information on structural damage in plantation crops or lodging of field crops.

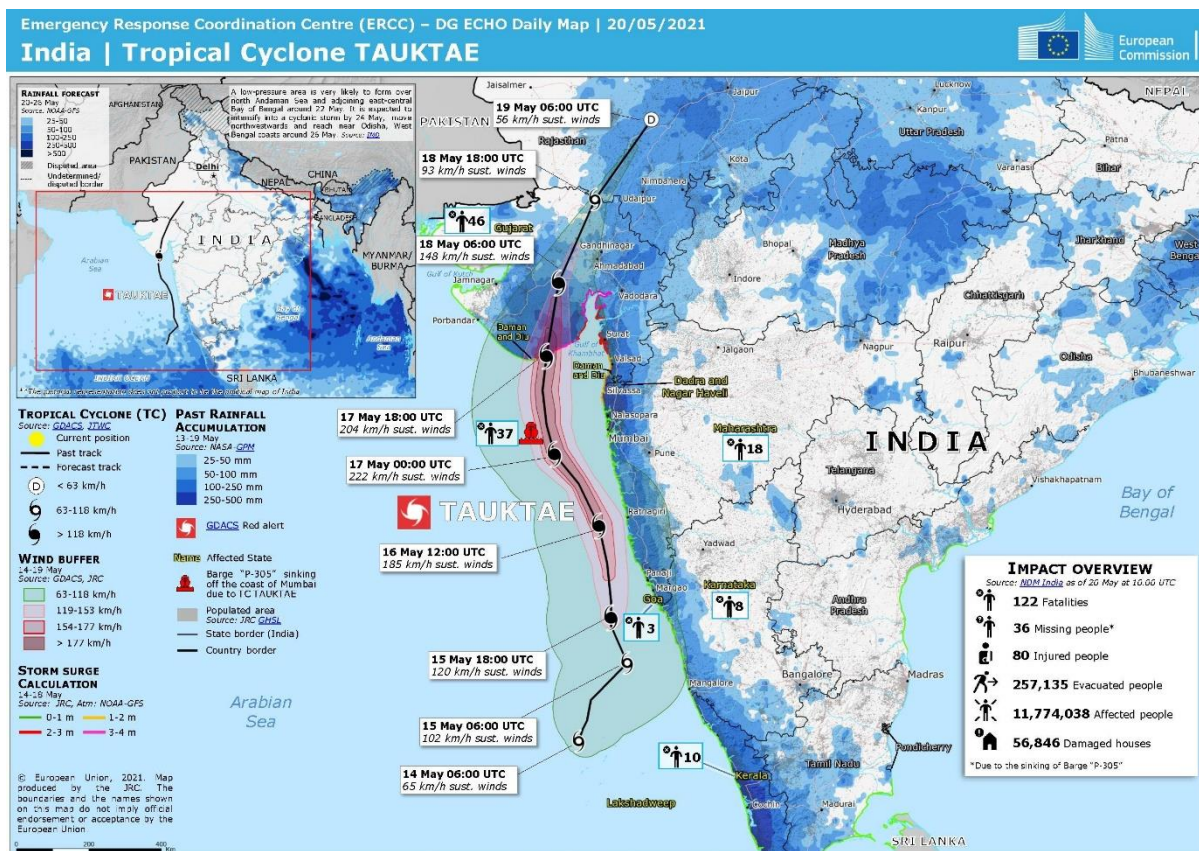


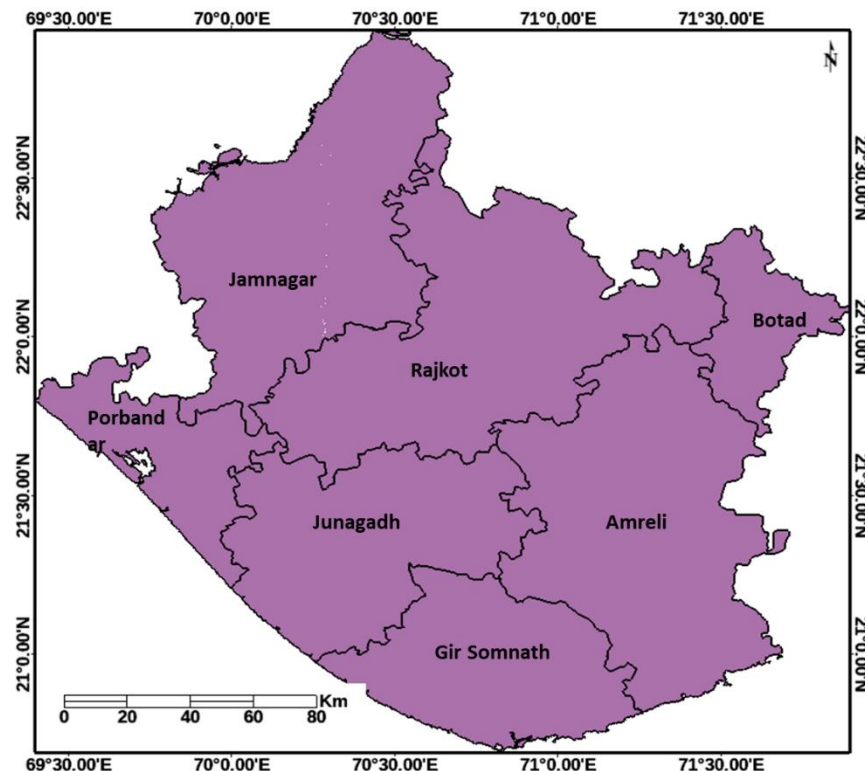
Figure 6.1: Sowing location and track of cyclone Tauktae.

6.2 Study Area and Dataset

A detailed study has been carried out to assess the damage caused by cyclone Tauktae on agricultural and horticultural crops over Saurashtra region of Gujarat. The study districts were Amreli, Gir Somnath, Bhavnagar, Junagadh, Botad, Rajkot, Porbandar and Jamnagar (Fig. 6.2). Optical and C-band SAR data from Sentinel 2 (A & B) and Sentinel-1 (A & B) were used for the study. The satellite data corresponding to pre and post cyclone dates from the current year (2021) and last 5 years were used for the study as summarized Table 6.1.

Table 6.1: Details of data Used

Sensor type	Sensor name	Data type	Date of Pass	Parameters used	Pixel Spacing
Optical	Sentinel 2A/2B	Multi-spectral	20th May 2021, 10th May 2021, 16th May 2020, 15th May 2019, 18th May 2018, 23rd May 2017	NDVI	10 m
C-band SAR	Sentinel 1A/1B	Microwave	9th May, 2021; 21st May, 2021	VV and VH backscatter	10 m

**Figure 6.2:** Study Area

6.3 Methodology

6.3.1. Generation of anomaly indicators using only-optical data

Among the existing anomalies, we have restricted the analysis to four commonly used types: i) Mean NDVI Anomaly, Eq. (1), ii) Post and Pre NDVI difference, Eq. (2), iii) Standard score (z-score, Eq. (3)), and, iv) the Vegetation Condition Index (VCI, Eq. (4)).

$$\text{Mean NDVI Anomaly} = (\text{NDVI}_i - \text{NDVI}_{\text{mean}}) \quad \dots \quad (1)$$

$$\text{NDVI Difference} = (\text{NDVI}_i - \text{NDVI}_{\text{pre}}) \quad \dots \quad (2)$$

$$\text{Standard Score (Z score)} = (\text{NDVI}_i - \text{NDVI}_{\text{mean}}) / \text{NDVI}_{\text{sd}} \quad \dots \quad (3)$$

$$\text{Vegetation Condition Index (VCI)} = (\text{NDVI}_i - \text{NDVI}_{\text{min}}) / (\text{NDVI}_{\text{max}} - \text{NDVI}_{\text{min}}) \quad \dots \quad (4)$$

where, $NDVI_i$ is the NDVI at post-cyclone date. The $NDVI_{mean}$, $NDVI_{sd}$, $NDVI_{min}$ and $NDVI_{max}$, are the statistics extracted from the observations of previous 5 years' data (2017-2021), mean value, standard deviation, the minimum and the maximum values, respectively. In this way, NDVI observations like NDVI anomaly and NDVI difference at different times can be compared in terms of how extreme they are. Standard score assumes normal distribution to normalize the NDVI while VCI uses the range of past observations to locate the value of an observation. Vegetation mask was generated by thresholding pre cyclone NDVI (>0.25) and Forest mask was applied to keep only agricultural and horticultural crop fields. The methodological flowchart is shown in Fig. 6.3.

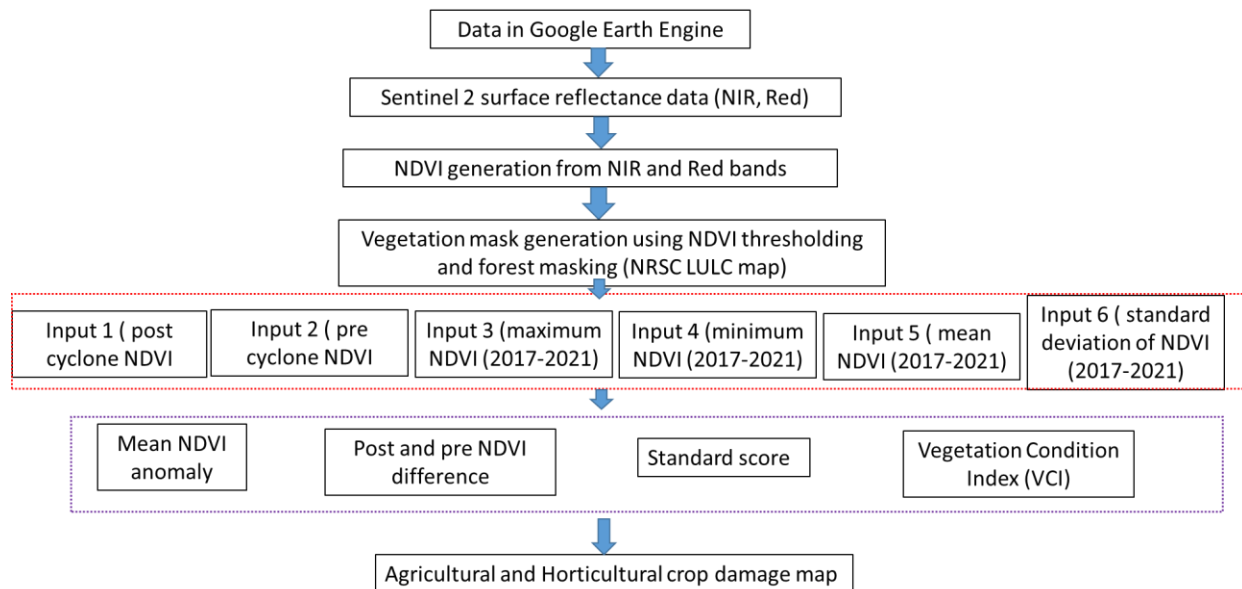


Figure 6.3. Methodological flowchart for optical data

6.3.2. Development of damage detection protocol using only-SAR data

Sentinel 2 derived NDVI images were composited using Maximum Value Compositing (MVC) method from both Pre and post-cyclone. From the pre-cyclone NDVI composite image active vegetation mask was generated using NDVI value thresholding (NDVI greater than 0.25 marked as active vegetation). The agricultural mask (before cyclone) is then applied on all the S1A derived GRD data for further analysis. Sentinel 1A derived VH and VV backscatters over agriculturally active vegetation pixels were analyzed for any changes in frequency distribution histograms before and after cyclone using skewness and kurtosis. Differences in VH, VV and VV/VH backscatter between pre and post-cyclone are mapped over the agriculture pixels. Those pixels with positive backscatter difference (increase in backscatter from pre to post-cyclone resulting in decrease in

backscatter dB values) are mapped as probable affected areas. Probable affected areas are further classified into three damage classes of less affected, moderately affected and highly affected areas using equi-quantile segregation of the 95 percentile values. The flowchart of SAR data processing is shown in Fig. 6.4.

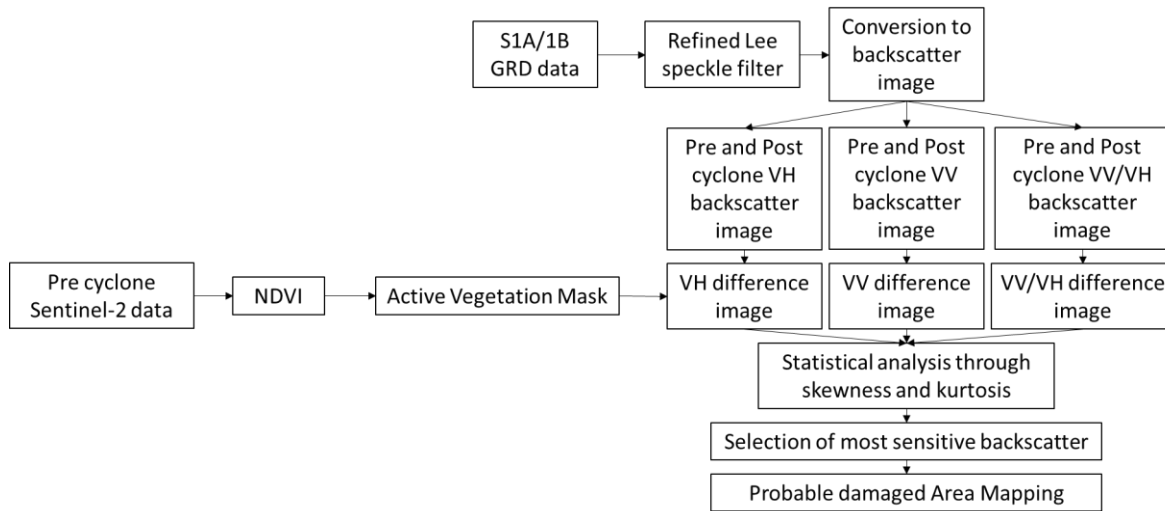


Figure 6.4. Methodological flowchart for SAR data

6.3.3. Opti-SAR Approach

In a separate approach both optical data from Sentinel-2 and microwave data from Sentinel-1 were used to segregate damage between agricultural and horticultural crops. Difference images of Sentinel-2 derived NDVI between pre and post cyclone were computed. Separately, VH, VV and VV/VH backscatter difference images were also computed. Stacked images of NDVI images and SAR backscatter images were then generated. Through random sampling, numerous points were generated over the stacked image. From pairwise scatterplots between SAR backscatter and optical NDVI, the whole data points could be segregated into four quadrants. On the basis of certain value thresholding and expert logic, the probable damage area was segregated into probable horticultural and agricultural crop damaged area. The methodology followed is shown in Fig. 6.5.

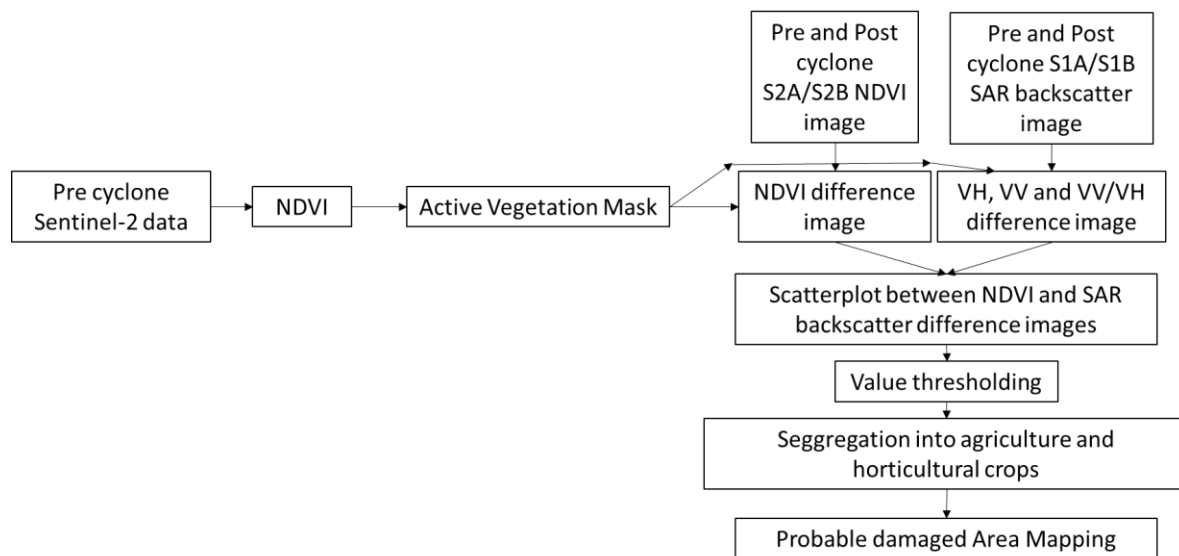


Figure 6.5: Methodology flowchart for Opti-SAR approach

6.4 Results and Discussion:

6.4.1. Damage detection

6.4.1.1. Using only-Optical data

The multi-temporal NDVI profile of a specific crop would be expected to reflect the crop's general phenological characteristics (e.g., timing of green up, peak greenness, and senescence) if the data have sufficient spatial and temporal resolution. The biological window of summer crops starts from mid-February and ends in last week of May to 1st week of June depending on the type and duration of crops. It reaches its maximum peak NDVI during first week of May when the crop is in peak vegetative stage and afterwards decreases towards physiological to harvest maturity. The temporal 5-year NDVI profile of summer crops during normal year and cyclone year has been depicted in Fig. 6.4. In all the normal years from 2017 to 2020, the temporal NDVI started increasing from mid-February, reached maximum during first week of May and started decreasing when the crop reached in senescence phase and finally reached lowest level during last week of May when the crop was harvested. However, in 2021 when cyclone Tauktae came the summer crops were in flowering to grain/seed/pod development stage and were advancing towards reproductive stage. The heavy rainfall caused flooding of fields and since these crops are sensitive to water logging, chlorosis started, leading to decline in greenness of these crops and as a result, there was a sudden drop in NDVI profile (Fig. 6.6). After flooding there is a chance of immediate receding of excess water and in that case crop can withstand the damage and recover quickly

resulting in somewhat increase in greenness and NDVI. To ensure this we analysed NDVI data of 9th June 2021, which showed that there was no any increasing trend of NDVI profile for 2021 crops. It continued to decline, suggesting damage to the crops. FCC of post cyclone date (20th May 2021) also indicated the same phenomenon, which shown in Fig. 6.7.

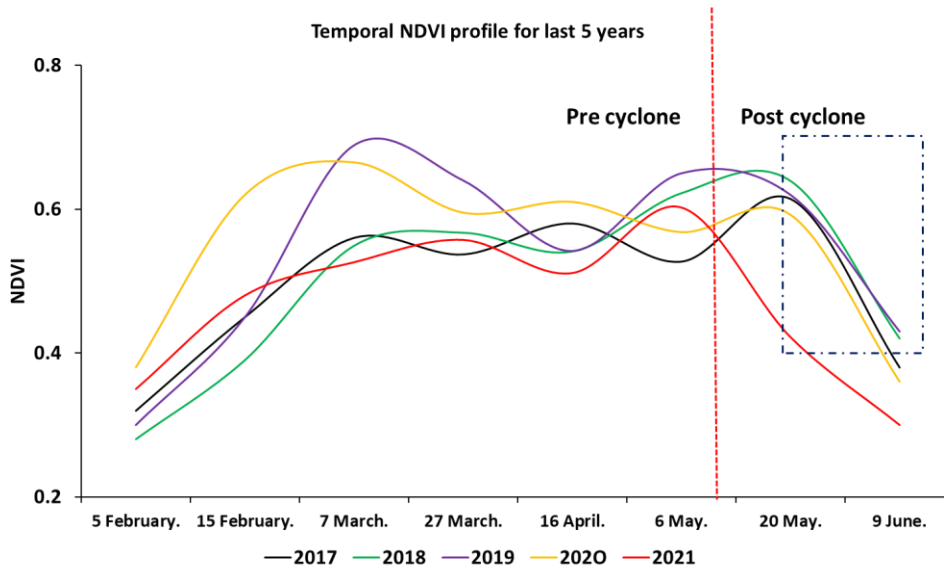


Figure 6.6: Temporal NDVI profile of summer crops during normal and cyclone year

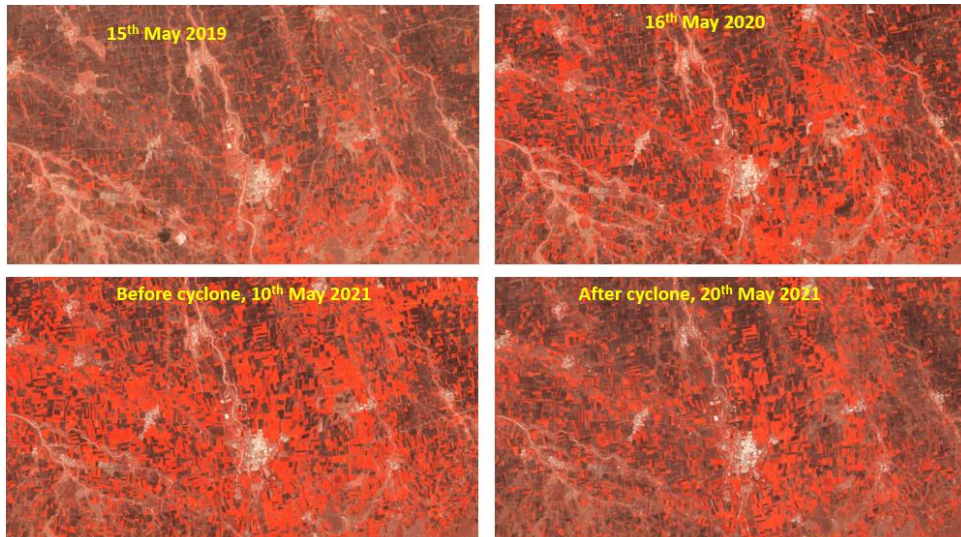


Figure 6.7: FCC over part of Junagadh district showing changes in agricultural fields during pre and post cyclone

Therefore, to analyze the damage four indices were studied, which were mean NDVI anomaly (2017 to 2021), post and pre NDVI difference, Standard score and Vegetation Condition Index

(VCI). Based on these indices four (4) categories of affected areas were made. Those were highly affected, moderately affected, less affected and not affected. To improve the readability of anomaly maps and to highlight major spatial patterns, anomaly values are often reclassified into a few classes separating normal, above or below normal and extreme conditions. The number of classes and the thresholds employed are somehow subjective and vary among users. Here we have used the setting proposed by the World Meteorological Organization to classify z-score. To classify VCI anomalies we use the settings proposed by Klisch and Atzberger (2016). To classify mean NDVI anomaly and NDVI difference we computed the histogram of each index over the entire region and divided it into 4 equal intervals for the purpose. The histogram diagram of these indices has been shown in Fig. 6.8 and range of each type of anomaly i.e. highly affected, moderately affected, less affected and not affected is given in Table 6.2 and classified map of each anomaly type has been given in Fig. 6.9.

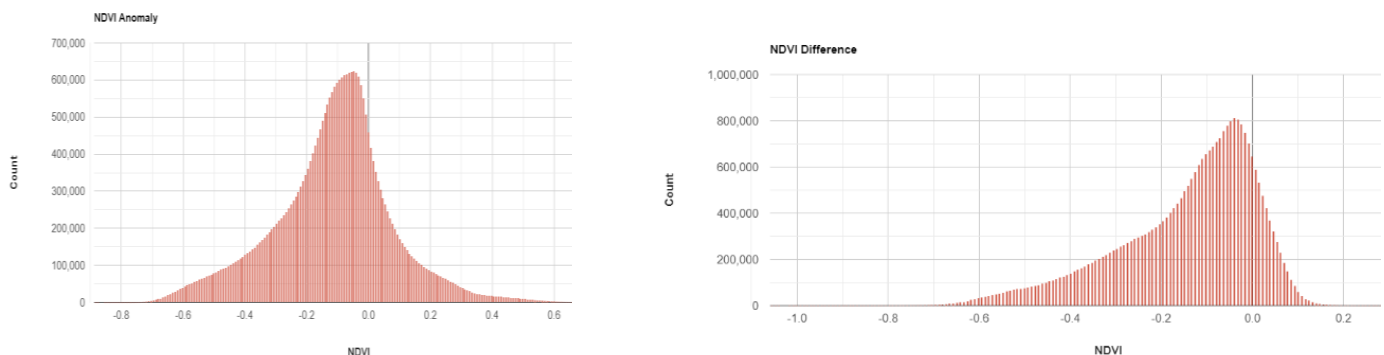


Figure 6.8: Histogram chart for mean NDVI anomaly and NDVI difference over selected districts

Table 6.2. Categorization of anomaly values into anomaly classes

Indices/Value	Highly Affected	Moderately Affected	Less Affected	Not Affected
Mean NDVI anomaly	< -0.2	-0.2 to 0.1	0.1 to 0.2	> 0.2
NDVI difference	< -0.2	-0.2 to 0.1	0.1 to 0.2	> 0.2
Standard score	< -1.5	-1.5 to 1	1 to 1.5	> 1.5
VCI	< 10%	10 to 30%	30 to 50%	> 50%



Figure 6.9. Example of NDVI anomaly, NDVI difference, Standard score and VCI map

After generating the different anomaly indices over vegetation mask of agricultural and horticultural crops district wise crop classification was made as, highly affected, moderately affected, less affected and not affected. The classified crop map has been shown in figure 10.

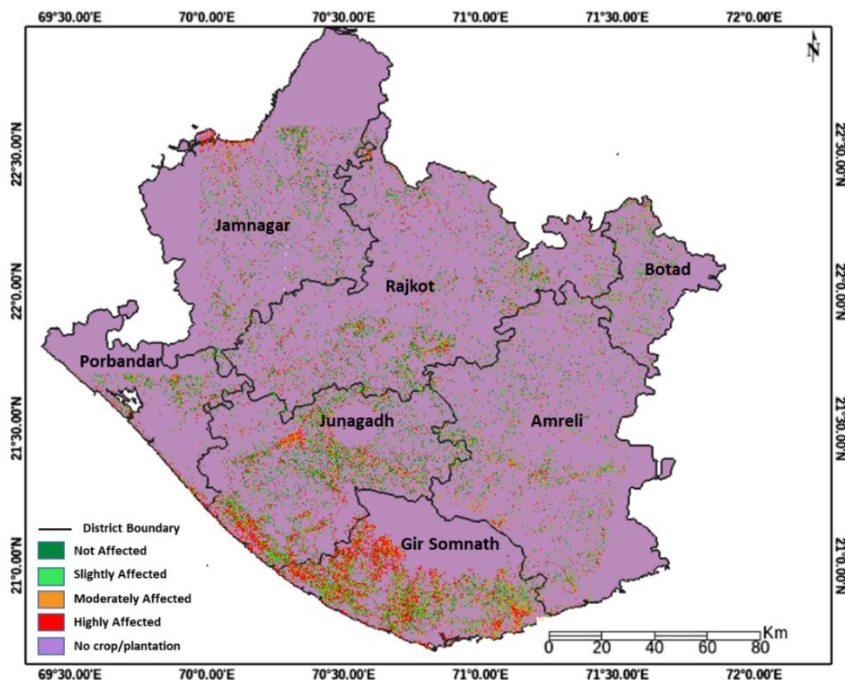


Figure 6.10: Classified damage map for most affected districts of Saurashtra region of Gujarat

6.4.1.2. Using only-SAR data

From the results, it can be seen that from pre to post-cyclone both VH, VV and VV/VH backscatter (in dB) either decreased in some part or increased in some part of the study area. However, the increase in dB is more profound in VH channel rather than VV (Fig. 6.11). In VV/VH backscatter difference, more area is showing decrease in backscatter ratio as compared to either VH or VV backscatter alone. Decline in both VH and VV backscatter (positive dB difference as shown in red to magenta color) might be due to inundation of crop fields resulting in lowering of backscatter values. However, interestingly in rest of the parts, the backscatter difference between pre and post-cyclone are found to be negative, which could be due to increase in backscatter values either due to increase in surface soil moisture (exposed soil between crop rows) or increase in surface roughness due to crop canopy disturbances. From the table in Fig. 6.12, it could be seen that both skewness and kurtosis of frequency distribution of histograms varied between pre and post-cyclone for both VH, VV and VV/VH. Fig. 6.12 shows the relative changes in skewness and kurtosis after cyclone for both VH, VV and VV/VH backscatters. The δ changes in skewness is highest in case of VV backscatter while change in kurtosis is highest in VV/VH backscatter (Fig. 6.13). Considering the dilemmatic situation of major change in skewness and kurtosis values between pre and post cyclone, it is difficult to select one parameter that could be used for further analysis. However, as skewness signifies changes in the lateral spread of data distribution as compared to change in peakedness in case of kurtosis, it can be stated that, in the former case the change signifies increase in frequency in new data range while, in kurtosis, any change tells that the same value range has increased its frequency. Moreover, as the damage caused by cyclone Tauktae over inland areas of Saurashtra region are mainly caused by high wind, it will be rational to use VV backscatter than VH backscatter, as in high wind damage, canopy structure is damaged and VV backscatter is more sensitive to canopy structure than VH backscatter. Therefore, on the basis of interaction mechanism of SAR backscatter with vegetation and also statistical distribution parameters, VV backscatter difference over the study sites is used for further mapping of affected areas. However, at this point, it is difficult to map the probable damaged area from SAR backscatter difference alone, as the damage could affect throughout the range of values.

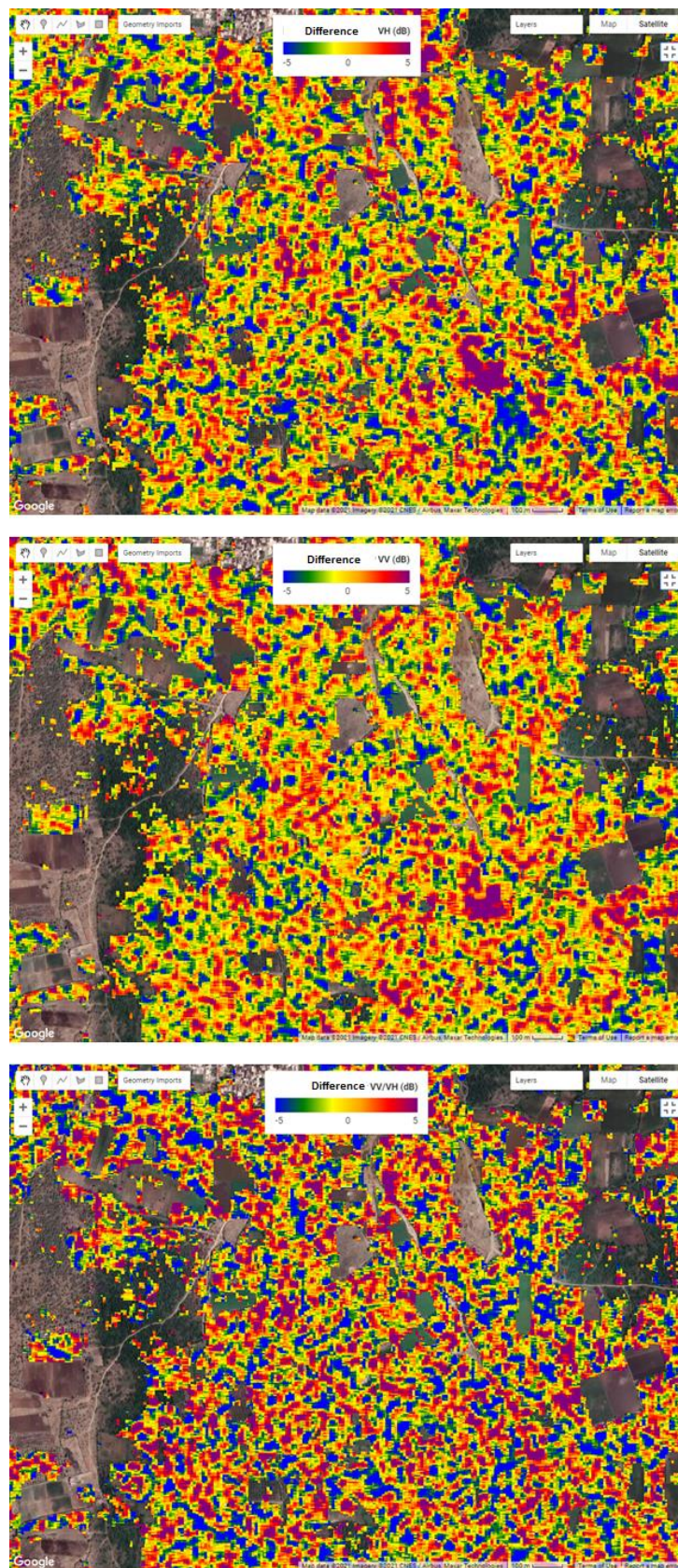


Figure 6.11: VH, VV and VV/VH backscatter difference (Pre – Post) over Junagadh, Gujarat

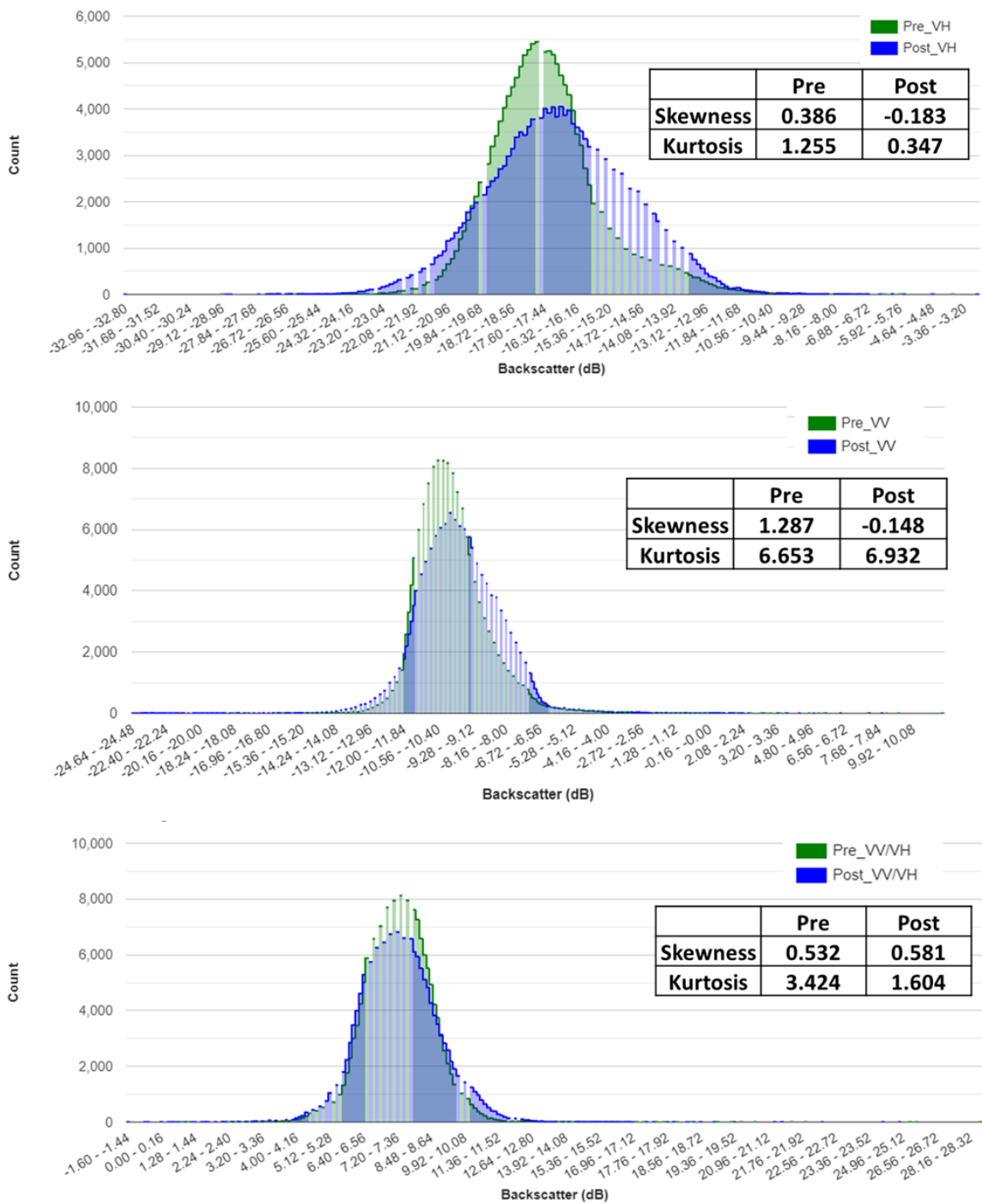


Figure 6.12: Frequency distribution histograms of Pre and Post cyclone VH and VV backscatter and change in Skewness, Kurtosis.

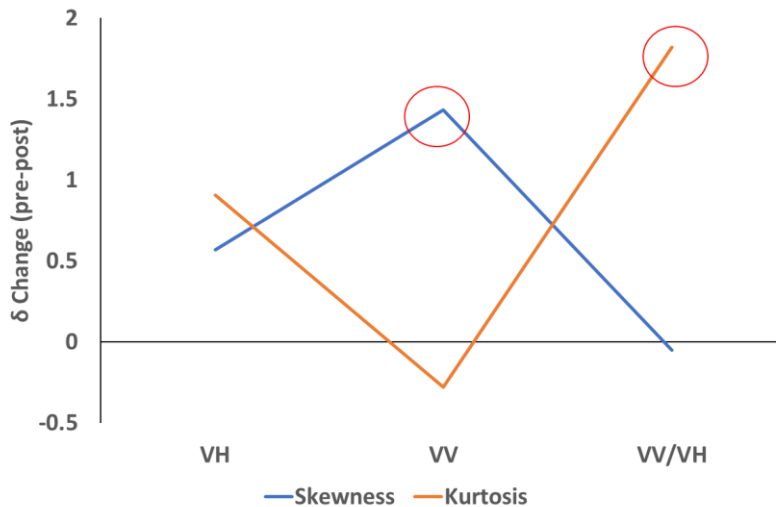


Figure 6.13: δ Change in Skewness and Kurtosis from Pre cyclone to Post cyclone

6.4.1.3. Using Opti-SAR combined data:

From scatterplot between NDVI difference and VV backscatter difference (Fig. 6.14), it can be found that, in quadrant 1 and 2 there are more points than quadrant 3 and 4. In quadrant 1, VV backscatter increase might be due to increase in surface roughness and NDVI also decreased because of probable decrease in leaf area. Therefore, these points in quadrant 1 belong to agricultural pixels that are damaged. However, in quadrant 2, both VV backscatter and NDVI decreased. Stagnation of water over crop fields might have increased smoothness resulting in decline in VV backscatter after cyclone. At the same time water background also caused NDVI values to drop. Interestingly, in quadrant 4, VV backscatter increased post cyclone owing to increase in surface roughness. At the same time NDVI also increased, which could be due to the change in orientation of fallen tree branches from vertical to horizontal position. Therefore, the pixels in quadrant 4, might belong to probable damaged horticultural crops. On the basis of this logic the pixels were segregated into probable damaged areas over agricultural and horticultural patches, separately. From Fig. 6.15 and 6.16, it can be seen that VV backscatter difference over the probable affected agricultural and horticultural areas varied from 0 to 7 dB and 0 to 1 dB, respectively. These backscatter differences in either case were classified through equi-quantile segregation into three classes of affected areas. Low affected agricultural patches are having dB difference of 0 to 3 dB, moderately affected areas are having dB difference of 3 to 5 dB and highly affected regions are having dB difference of 5 to 7 dB. While low affected horticultural patches are having dB difference of 0 to 0.3 dB, moderately affected areas are having dB difference of 0.3 to 0.6 dB and highly affected regions are having dB difference of 0.6 to 1 dB.

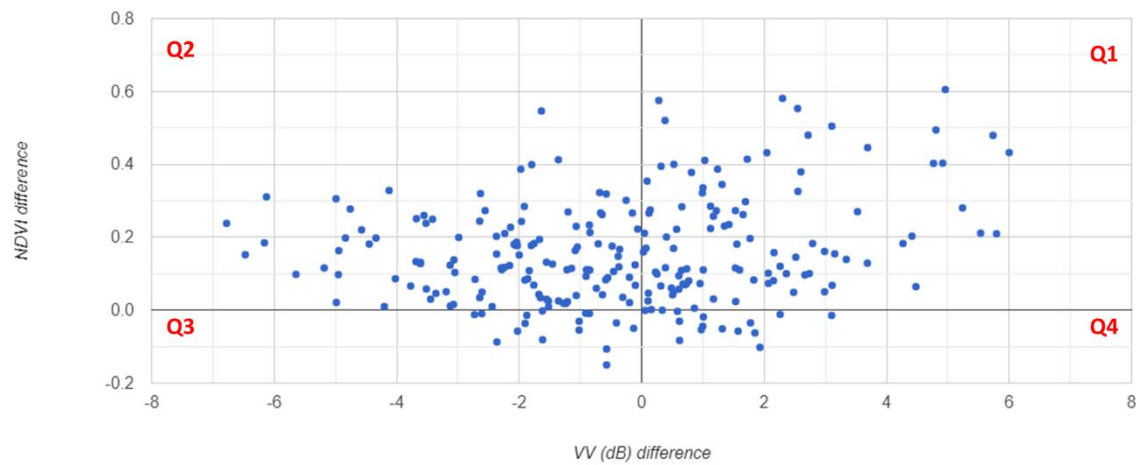


Figure 6.14: Scatterplot between NDVI difference (Pre-Post) and VV backscatter difference (Pre-Post) segregated into four quadrants, Q1, Q2, Q3 and Q4.

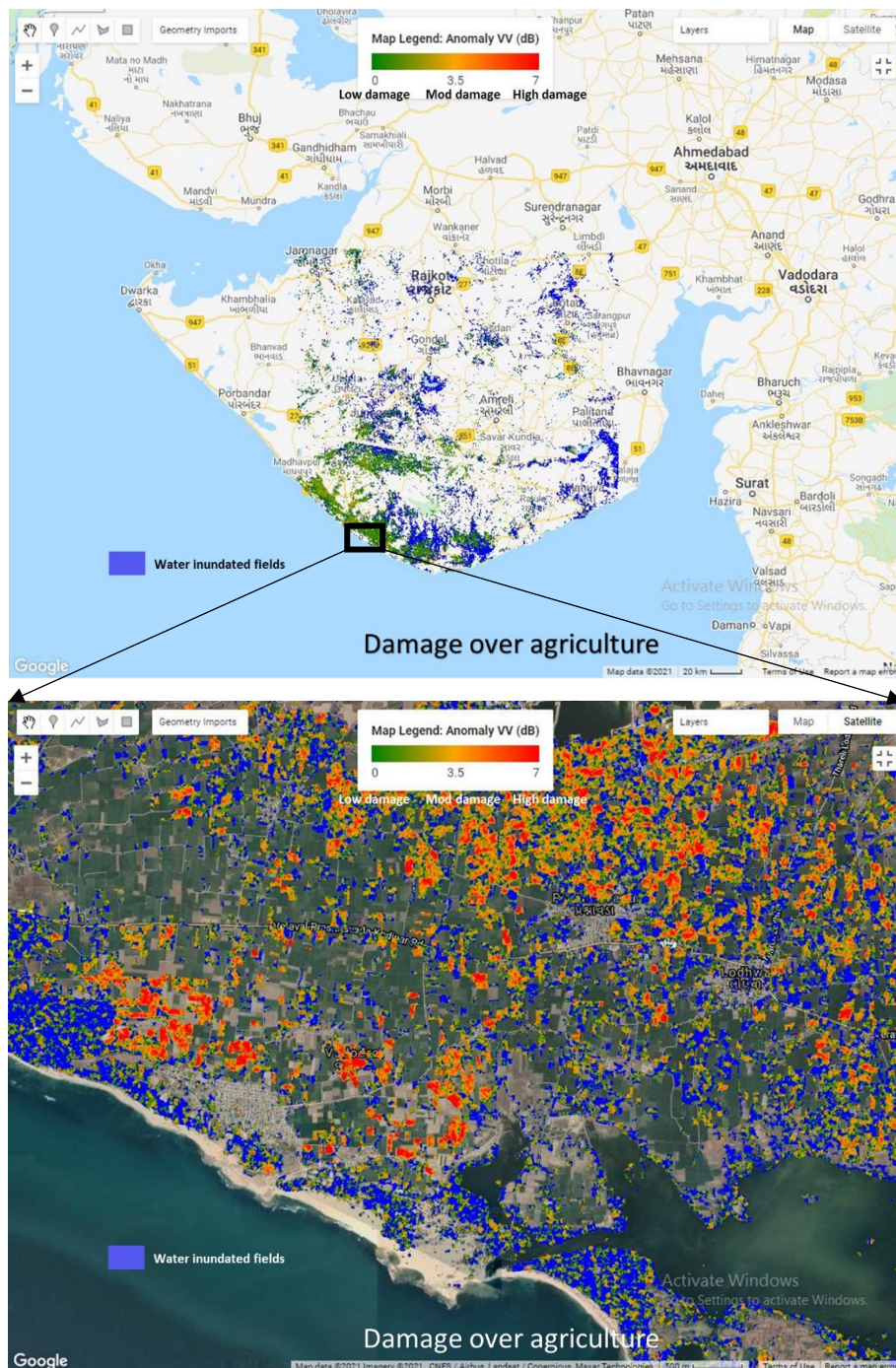


Figure 6.15: Probable affected areas over agricultural patches as obtained from Opti-SAR combined approach

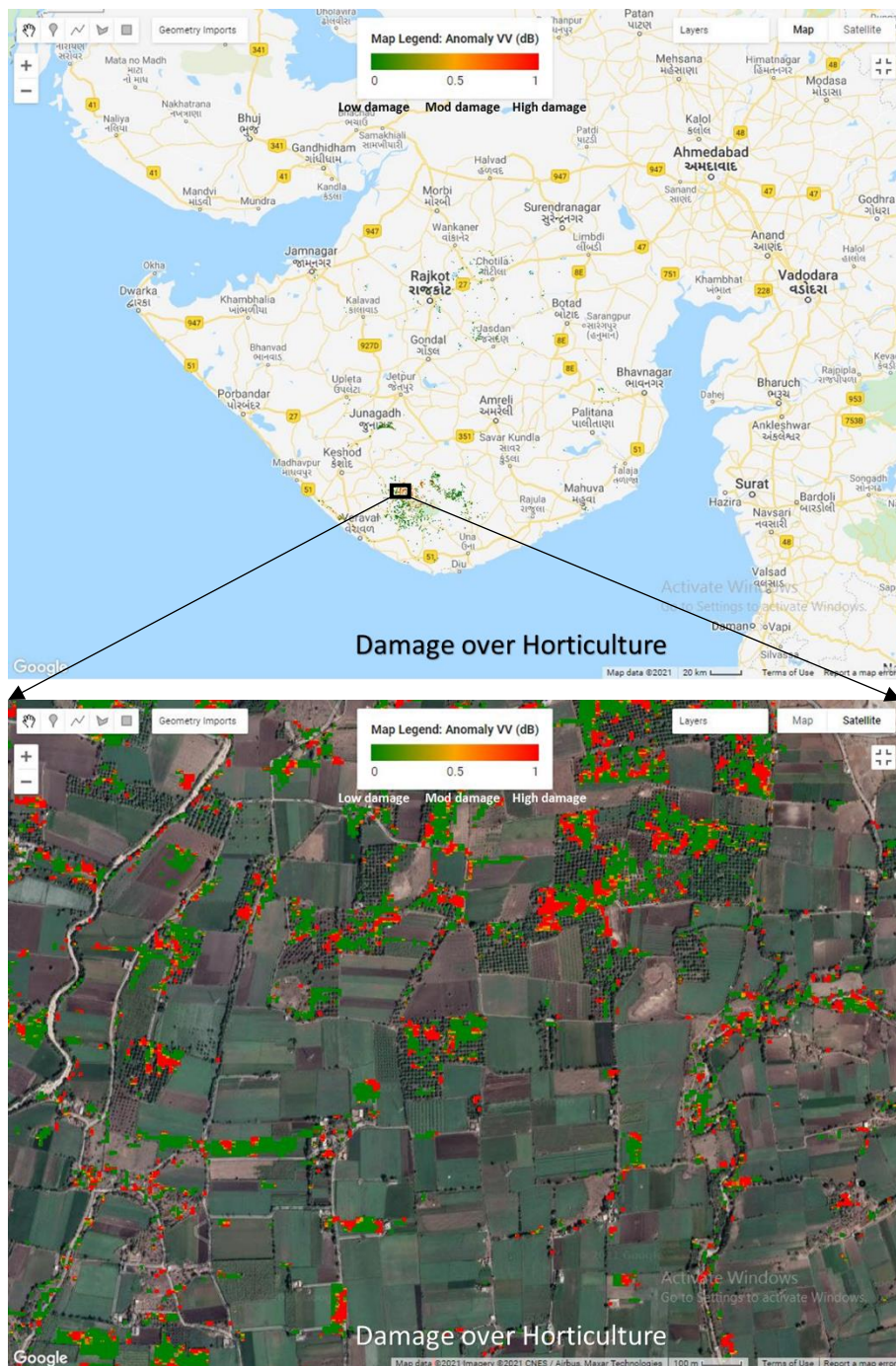


Figure 6.16: Probable affected areas over horticultural patches as obtained from Opti-SAR combined approach

6.4.2 Damaged area estimation

6.4.2.1 From Optical data

The results showed that Gir Somnath was the most affected district with 41.4% crop acreage in highly affected class and 24.6% in moderately affected class. It was followed by Junagadh district where highly and moderately affected area were 29.7 and 20 %, respectively. Highly affected area

in Rajkot, Amreli, Botad, Jamnagar and Porbandar came around 19.1%, 20.5%, 12.7%, 21.8% and 29.6% respectively. Among these districts, not affected class was found to be maximum in Jamnagar district (31.2%) followed by Rajkot (29.2%). Crop area that withstands this cyclone in Gir Somnath, Junagadh, Amreli, Botad and Porbandar were 11.5%, 26.2%, 19%, 25.5% and 26.4%, respectively. The district wise statistics and damage assessment map are shown in Table 6.3 and Fig. 6.17.

Table 6.3: Crop/Plantation damage assessment for different districts

Sl No.	Value	Area (ha)	Area (%)
Gir Somnath			
1	Not Affected	12697	11.5
2	Less Affected	24845	22.5
3	Moderately Affected	27098	24.6
4	Highly Affected	45727	41.4
	Total	110367	100

Sl No.	Value	Area (ha)	Area (%)
Rajkot			
1	Not Affected	21930	29.2
2	Less Affected	19310	25.7
3	Moderately Affected	19538	26.0
4	Highly Affected	14350	19.1
	Total	75128	100

Sl No.	Value	Area (ha)	Area (%)
Junagadh			
1	Not Affected	27211	26.2
2	Less Affected	24844	24.0
3	Moderately Affected	20912	20.1
4	Highly Affected	30883	29.7
Amreli			
1	Not Affected	10764	19
2	Less Affected	15311	27
3	Moderately Affected	19027	33.5
4	Highly Affected	11678	20.5
	Total	56780	100

Sl No.	Value	Area (ha)	Area (%)
Botad			
1	Not Affected	3798	25.5
	Less Affected	5150	34.6
3	Moderately Affected	4050	27.2
4	Highly Affected	1868	12.7
	Total	14868	100

Sl No.	Value	Area (ha)	Area (%)
Jamnagar			
1	Not Affected	13884	31.2
2	Less Affected	10612	23.8
3	Moderately Affected	10332	23.2
4	Highly Affected	9670	21.8
	Total	44498	100

Sl No.	Value	Area (ha)	Area (%)
Porbandar			
1	Not Affected	4776	26.4
2	Less Affected	4150	22.8
3	Moderately Affected	3866	21.2
4	Highly Affected	5365	29.6
	Total	18157	100

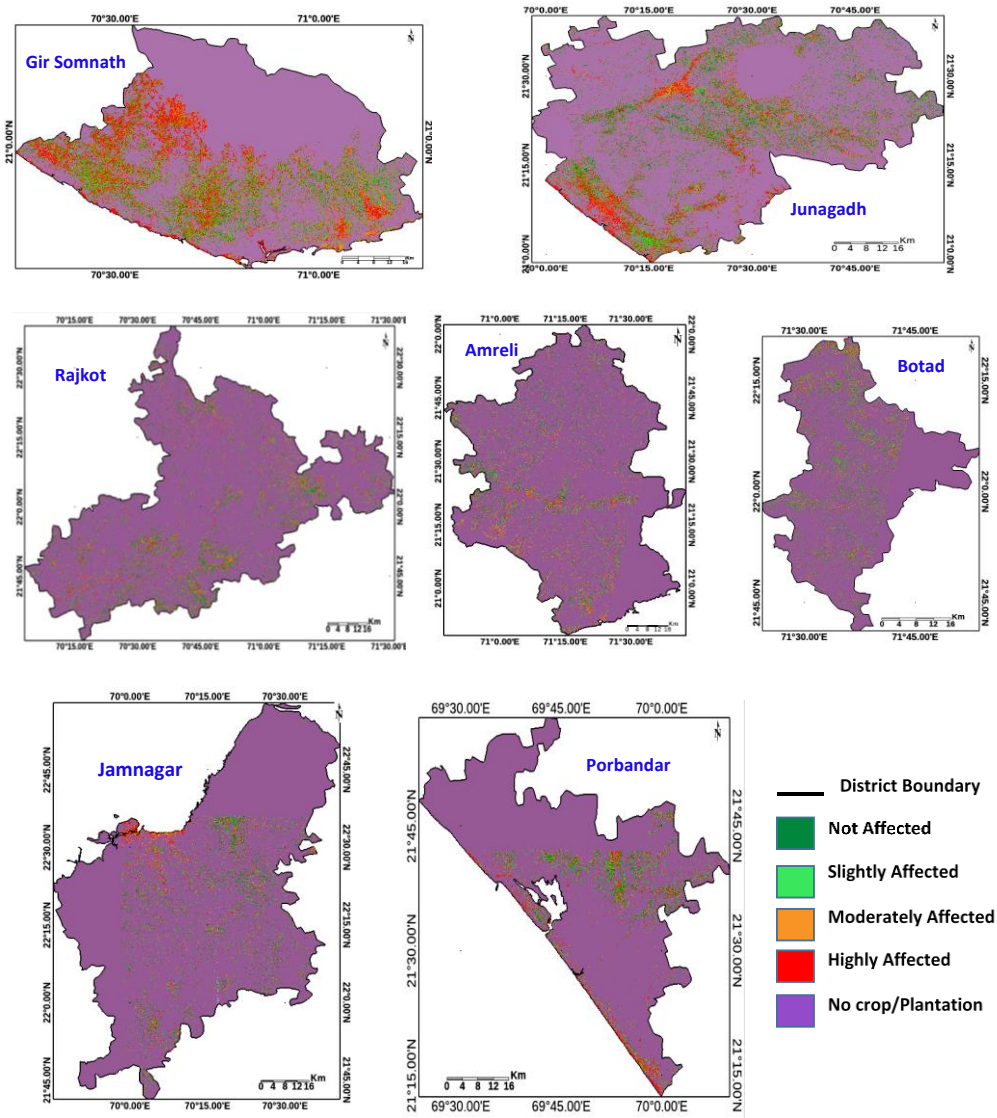


Figure 6.17: Classified damage map for Gir Somnath, Junagadh, Rajkot, Amreli, Botad, Jamnagar and Porbandar districts of Saurashtra region of Gujarat

6.4.2.2 From Opt-SAR combined data

The district wise acreage of probable affected agricultural and horticultural areas for Amreli, Bhavnagar, Junagadh, Porbandar and Rajkot are shown in Table 6.4. Although disagreements are found between district-wise damaged area estimates from either optical or opti-SAR approach, the general trend of damage across districts are almost same. From the table it can be seen that over agricultural patches major damage was caused in Junagadh district, followed by Porbandar, Rajkot, Bhavnagar and Amreli district. In Junagadh and Porbandar, 21% area was highly damaged, while 66 % and 54 % area were moderately damaged and 13% and 25 % area were less damaged,

respectively. Considering the damage over horticulture, major damage was caused in Bhavnagar, followed by Junagadh. In Amreli, Rajkot and Porbandar, affected area was less. Although the total area under damage was higher in Bhavnagar than Junagadh, considering the level of damage moderate to high level of damage was caused in around 34 % of the area in Junagadh while less than 4 % area was affected in Bhavnagar. Further validation of acreage estimates with independent government estimates are henceforth needed.

Table 6.4: Damaged agricultural and horticultural area over different districts of Gujarat from Opti-SAR approach

District	Acreage (ha)			
	Low damage	Moderate damage	High damage	Total
Damage over Agricultural patches				
Amreli	16215 (80 %)	3036 (15 %)	1228 (5 %)	20479
Bhavnagar	25224 (84 %)	3740 (13 %)	1141 (3 %)	30105
Junagadh	4645 (13 %)	25210 (66 %)	8097 (21 %)	37952
Porbandar	8666 (25 %)	18205 (54 %)	7208 (21 %)	34079
Rajkot	24489 (73 %)	6836 (20 %)	2076 (7 %)	33401
Damage over Horticultural patches				
Amreli	1952 (95 %)	45 (2 %)	56 (3 %)	2053
Bhavnagar	6162 (97 %)	108 (3 %)	20 (<1 %)	6290
Junagadh	3506 (66 %)	1442 (28 %)	305 (6 %)	5253
Porbandar	1102 (94 %)	50 (4 %)	25 (2 %)	1177
Rajkot	1561 (77 %)	429 (21 %)	39 (2 %)	2029

* Value in parentheses shows the % contribution in acreage to the total damaged area in a district

6.5 Conclusions

The systematic and analysis-ready data (ARD) of various optical as well as SAR sensors like Sentinel-2A/2B or Sentinel-1A/1B in Google Earth Engine's (GEE) cloud platform provides ample opportunity to assess quick damage caused by natural disaster like cyclone. This also allows a novel combination of both optical and microwave data in a common platform. NDVI, which

represents the crop phenological cycle, can be used to study sudden change in its temporal pattern due to any event that can cause potential damage in crop vigour and finally productivity. Cyclones such as Tauktae results in flooding of agricultural fields, thereby causing yellowing of crops, which finally results in sudden drop of NDVI profile. To assess the damage caused by cyclone Tauktae over Saurashtra region of Gujarat, four anomaly indices i.e. mean NDVI anomaly, NDVI difference, Standard Score and Vegetation Condition Index (VCI) have been studied. Although NDVI based metrics could be used successfully over agricultural crop patches for probable damage detection, this approach failed to detect damage over horticultural patches. Similarly, use of C-band SAR data alone was not enough to quantify cyclone damage. However, combined use of optical data along with microwave data enabled segregation of damage over agricultural and horticultural patches and it also helped in identifying flooded areas. From the results we could find that Gir Somnath was the most affected district where severe crop damage was found followed by Junagadh, Porbandar and Rajkot. While in case of horticultural crops, moderate to high damage was found in Junagadh while, in rest of the districts, damage level was low. This analysis also suggested that crops in Jamnagar were least affected followed by Rajkot. Therefore, during a catastrophic event like cyclone, this kind of analysis could prove to be very useful for quicker damage assessment and contingency planning subject to frequent (1-3 days) availability and on-line accessibility of Analysis-Ready-Data (ARD) in optical bands and SAR from very high resolution (1-5m) satellites.

References

1. https://earthobservatory.nasa.gov/cyclone_Taukate-strikes_India.
2. https://en.Wikipedia.org/wiki/cyclone_Taukate.
3. Kanjir, U., Duric, N., Veljanovski, T.2018. Sentinel-2 based temporal detection of agricultural land use anomalies in support of common agricultural policy monitoring. ISPRS International Journal of Geo-information. 7, 405; doi:10.3390/ijgi7100405.
4. Klisch, A., Atzberger, C. 2016. Operational drought monitoring in Kenya using MODIS NDVI time series. Remote Sens. 8. <https://doi.org/10.3390/rs8040267>.
5. Kumar, A., Brahmanand, P.S., Nayak, A.K.2014. Management of Cyclone Disaster in Agriculture Sector in Coastal Areas. Directorate of Water Management. Bhubaneswar. P108.

6. Meroni M., Fasbender D., Rembold F., Atzberger C., Klish A.2019. Near real-time vegetation anomaly detection with MODIS NDVI: Timelines vs accuracy and effect of anomaly computation options. *Remote Sensing of Environment* 221, 508-521.
7. Mouret, F., Albughdadi, M., Duthoit, S., Kouamé, D., Rieu, G., Tourneret, J.-Y.2021. Outlier Detection at the Parcel-Level in Wheat and Rapeseed Crops Using multispectral and SAR Time Series. *Remote Sens.* 13, 956. <https://doi.org/10.3390/rs13050956>.
8. Phan, N.P., Kuch, V., and Lehnert, L.W.2020. Land cover classification using Google Earth Engine and Random Forest classifier- The role of image composition. *Remote Sensing*.12,241, doi:10.3390/rs12152411.
9. World Meteorological Organization. 2012. Standardized Precipitation Index User Guide. World Meteorological Organization (WMO), Geneva, Switzerland.

7. Damage Assessment of Gir Forest Area in Gujarat

**C. P. Singh, C. Patnaik, Ayan Das, Mehul Pandya and Bimal
Bhattacharya**

7.1 Introduction

A detailed study has been carried out to assess the damage in forest region due to Tauktae cyclone in Gir protected area. The study included use of microwave and optical sensor data to explore the regions affected by the cyclone. Cyclone namely Tauktae hit the Gujarat (approx. 27 km east of Diu) on May 17, 2021. After making landfall, moving further inland it gradually weakened and ended as a low-pressure area on May 19, 2021 (Fig. 7.1). Just while hitting the Gujarat coast, Tauktae reached its peak intensity with maximum 3-minute sustained winds of 195 km/h and maximum 1-minute sustained winds of 220 km/h, and a minimum central pressure of 950 millibars making the storm the equivalent of a Category 4 tropical cyclone on the Saffir–Simpson scale. This kind of enormous wind speed not only caused damage to property but overturning of trees in Gir forest.

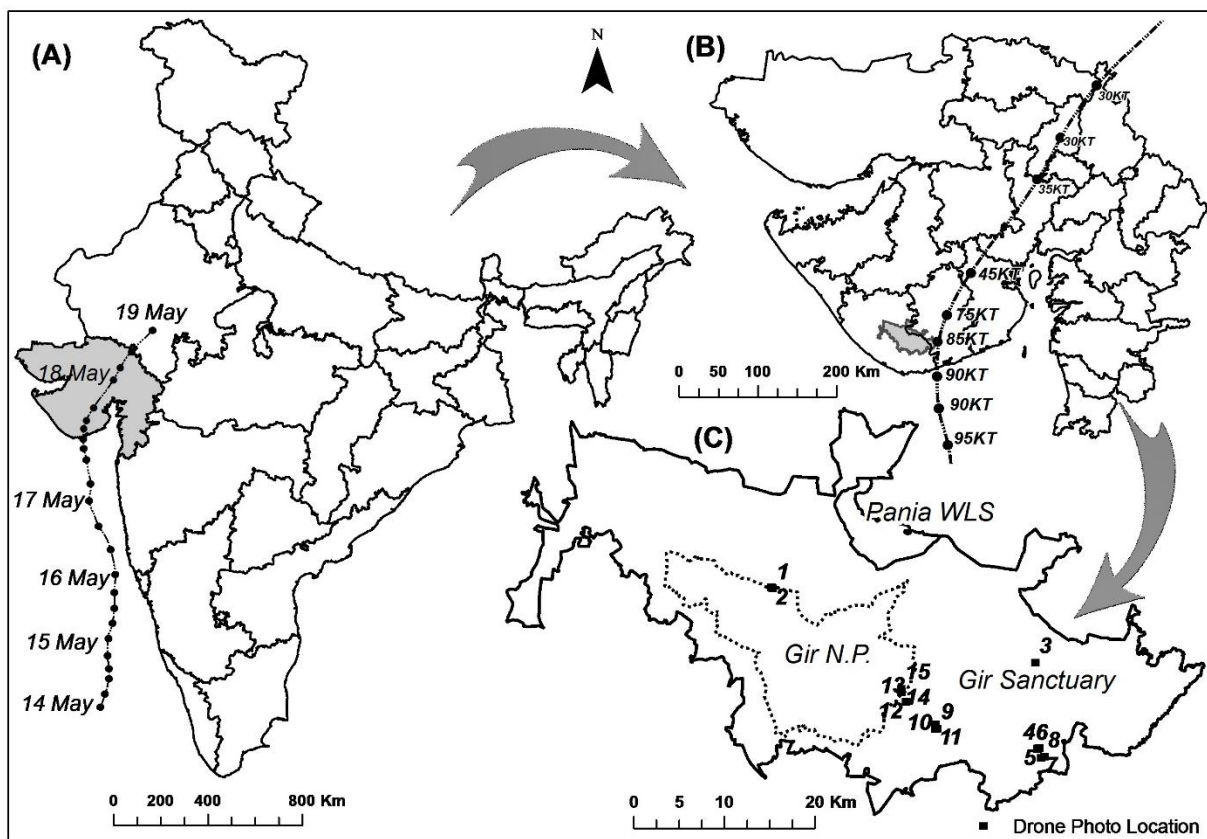


Figure 7.1: Study area showing (A). Track of Cyclone Tauktae over Arabian Sea and India, (B). Track of Cyclone Tauktae with speed in Knots (1KT = 1.852km/h) (C).Study area with Gir protected area boundary including Gir national park, Gir sanctuary and Pania wildlife sanctuary.

The districts of Junagadh, Gir-Somnath, Amreli and Bhavnagar were highly affected by heavy rainfall and winds (Fig. 7.2). The high wind velocity in Gir forest area reportedly flattened large number of trees. The main objective of the study was to assess the damage done by Tauktae cyclone in Gir protected area using best possible spatial resolution data available from optical as well radar-imaging satellites, and to provide qualitative spatial map and statistics on affected areas to stakeholders (Gujarat Forest Department).

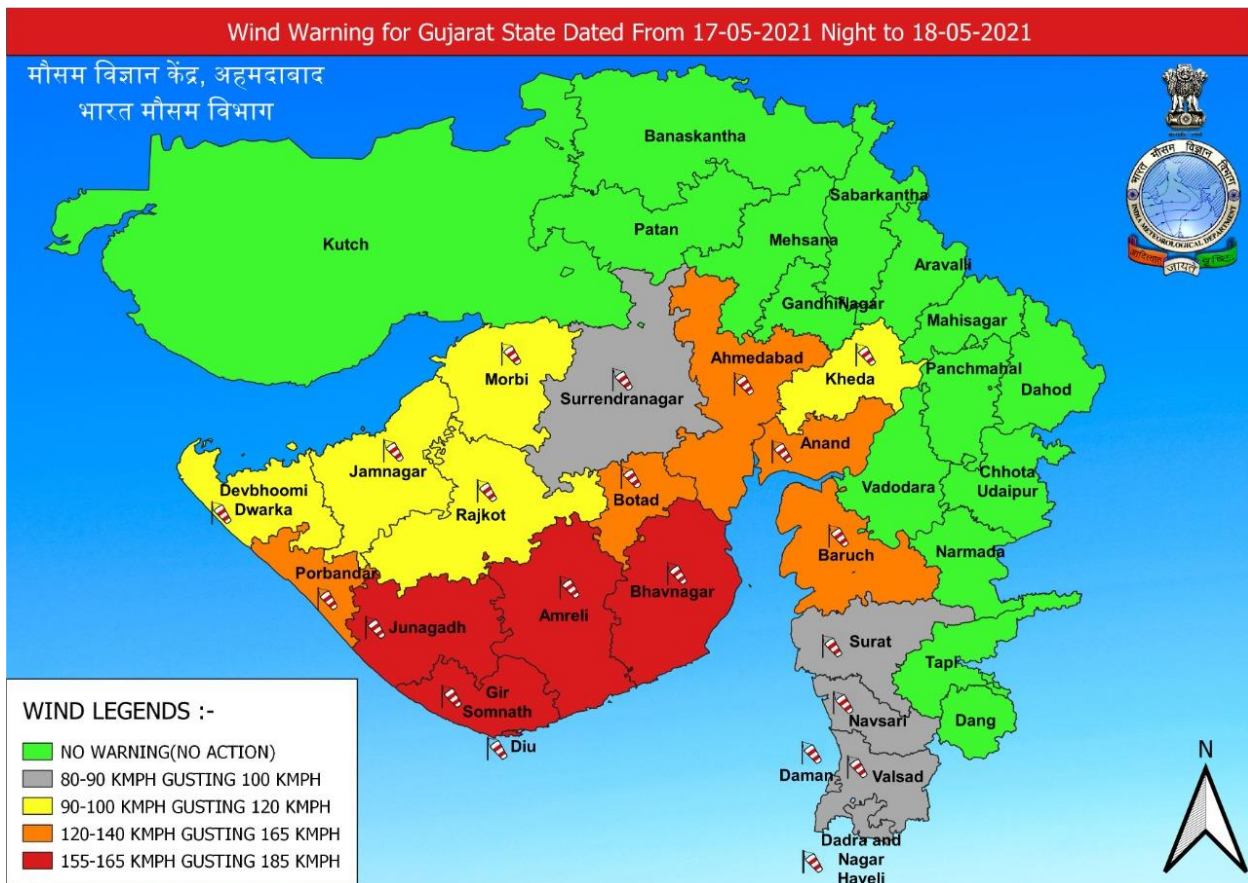


Figure 7.2: Wind warning map of Gujarat State (source: IMD)

7.2 Materials and Methods

7.2.1 Study Area

Gir National Park and Wildlife Sanctuary, also known as Sasan Gir, is a forest and wildlife sanctuary. It was established in 1965 with a total area of 1,412 km² of which 258 km² is fully protected as national park and 1,153 km² as wildlife sanctuary. Chanchai-Pania wildlife sanctuary was also included in the study area. Altitudinal range of the area varies between 83 - 524 m above mean sea level. The area is basically a dry deciduous open scrub forest with dry savannah. *Tectona*,

Butea, Acacia, Ficus, Zizyphus, Syzygium, Diospyros etc are the main tree species in the area. The 63.5 % area has forest canopy density < 10–40%, and about 35.89 % forest has density > 40 % to > 70% (Alam et al., 2014). Phenology of this dry deciduous forest is marked with leaf fall in the winter months (Fig. 7.3 & 7.4) and maximum senescence is observed in the summer months (March – May).

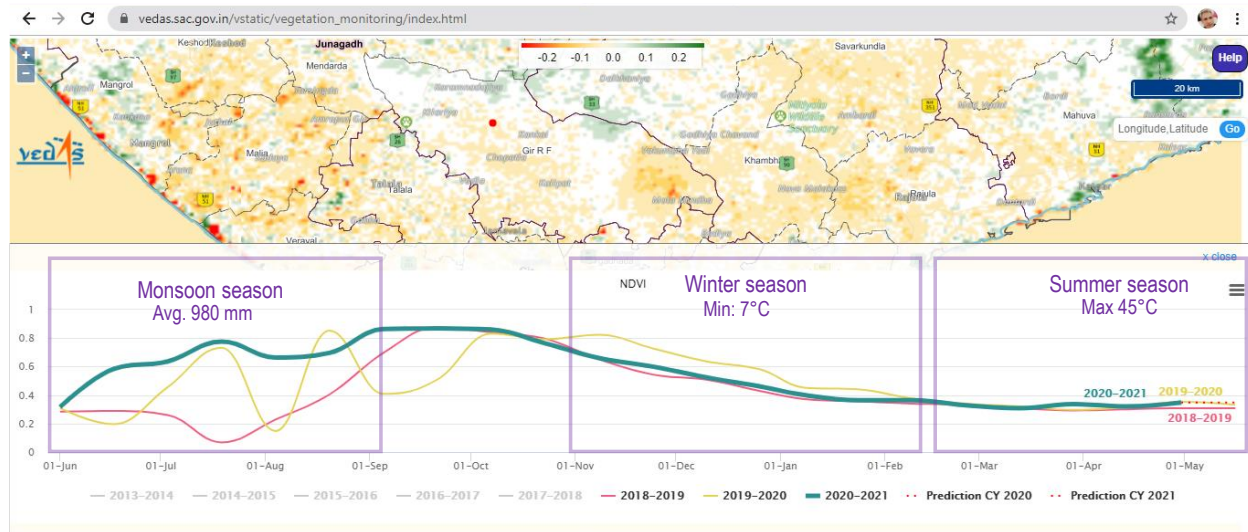


Figure 7.3: Phenological (greening to browning) curve of the Gir forest area (source: <https://vedas.sac.gov.in>).

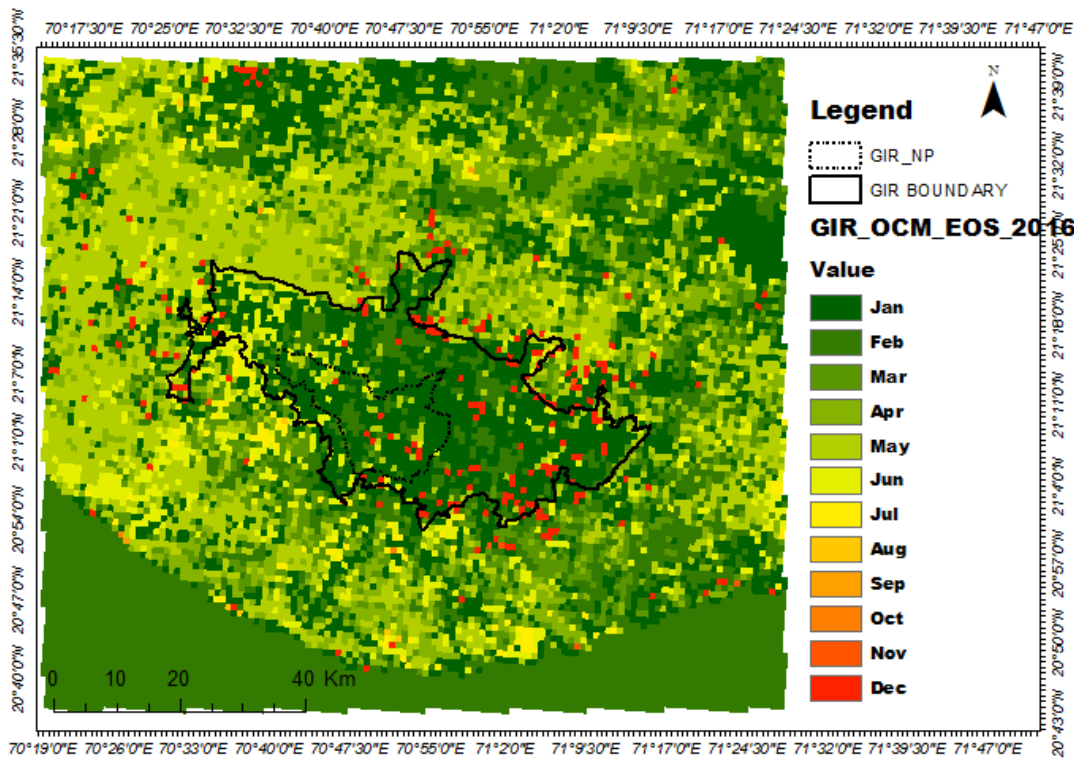


Figure 7.4: Phenological calendar map of Senescence period (when 80% of the leaf fall is observed) in the Gir forest and environs using Oceansat data (source: CP Singh, SAC).

7.2.2 Data-used

The data used for the analysis is given in the Table 7.1 with information on its acquisition date and ground sampling distance (GSD):

Table 7.1: List of datasets used for damage assessment in Gir protected area.

S.N.	Satellite	Sensor	Acq. Date	GSD (m)	Source
1	Sentinel 2B	MSI	20 May 2021	10	Copernicus
2	Sentinel 2B	MSI	10 May 2021	10	Copernicus
3	Sentinel 2B	MSI	20 May 2020	10	Copernicus
4	Sentinel 2B	MSI	18 May 2019	10	Copernicus
5	Sentinel 2B	MSI	18 May 2018	10	Copernicus
6	Sentinel 2B	MSI	23 May 2017	10	Copernicus
7	RCM 1	C-Band SAR	19 May 2021	12.5	Charter
8	Sentinel 1A	C-Band SAR	09 May 2021	10	Copernicus
9	Sentinel 1A	C-Band SAR	21 May 2021	10	Copernicus
10	Sentinel 1A	C-Band SAR	26 May 2020	10	Copernicus
11	Sentinel 1A	C-Band SAR	20 May 2019	10	Copernicus
12	Sentinel 1A	C-Band SAR	25 May 2018	10	Copernicus
13	Sentinel 1A	C-Band SAR	18 May 2017	10	Copernicus

7.2.3 Methodology

A hybrid approach of assessment was followed in which Vegetation Indices in optical and synthetic aperture radar (SAR) domain were derived for pre-cyclone and post cyclone periods (see Table 7.1). The standard pre-processing was adopted for arriving at the Normalized Difference Vegetation Index (NDVI, eq.1) and Radar Vegetation Index (RVI, eq.2) followed by computation of anomalies from mean trends in past years. All these processing were done using Google Earth Engine, Geomatica and ArcGIS software. In order to remove the incidence angle effect in SAR data, the backscattering across the range was normalized using the calibration coefficients. The preprocessing was carried out using the software: SNAP version 8. It was imperative to process the backscatter coefficient in the normal unit domain and then finally convert the same into log domain, to avoid arithmetical errors. The scattering characteristics of forest vegetation and other land use types were studied using dual-pol data over the study site, both in pre and post cyclone phases. Care was taken to understand the forest – SAR interactions under the given conditions with respect to the canopy, vegetation structure and background information. Both the vegetation indices were subjected to slicing (thresholding) based on field photographs (drone pictures shared with Gujarat forest department) and statistical distributions of the data, in order to come out with qualitative assessment on affected areas. The drone survey photographs were registered with archived Cartosat-2C (60 cm spatial resolution) and were used (with 10 - 13 cm spatial resolution) in the analysis as the ground truth information (Fig. 7.5). From the limited set of photographs obtained, the tree density over the area was also computed.

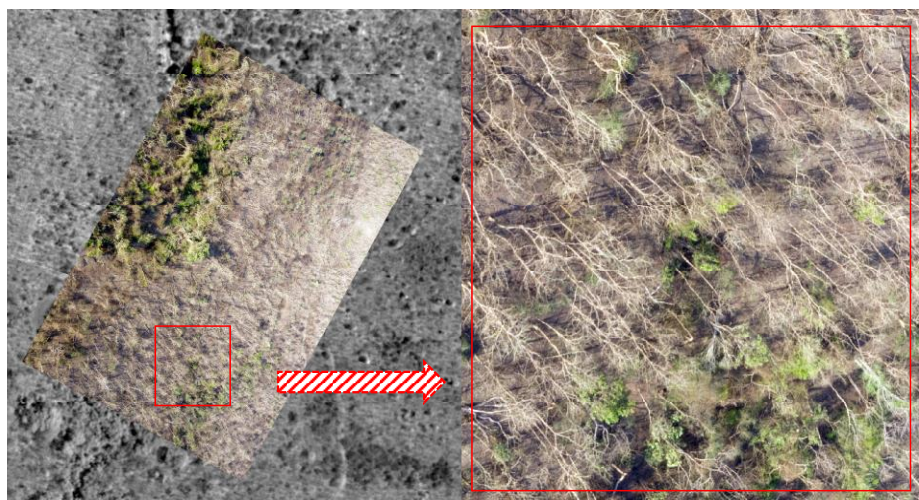


Figure 7.5: Drone photograph (no. 10 of Fig. 7.1C) registered using high-resolution Cartosat data for quantification of trees affected in 1 ha plot (red box area).

$$NDVI = \frac{(gNIR - gR)}{(gNIR + gR)} \quad (1)$$

Where, $gNIR$ = Reflectance of Near Infrared band and gR = Reflectance of Red band

$$RVI = \frac{(4 * \sigma^o_{VH})}{(\sigma^o_{VH} + \sigma^o_{VV})} \quad (2)$$

Where, σ^o = Sigma-nought, VH = vertical transmit and horizontal receive and VV = vertical transmit and vertical receive

Photographs provided by the Gujarat Forest Department from a drone survey in the post cyclone period was used in the analysis as the source of ground truth. From the limited set of photographs obtained, the tree density over the ground area was also qualitatively assessed.

Entropy of the study site was also studied for the pre cyclone and post cyclone period. Grey Level Co-occurrence Matrix (GLCM) based measure of entropy with direction invariant relationships were considered. A window size of 15×15 was used for the construction of the GLCM on SAR data. The entropy could not reveal the subtle textural variations though the entire study area. However, the information layer from entropy was used in conjunction with the cross polarisation ratio of VH/VV and VH to demarcate zones of potentially affected areas as a preliminary guide to the analysis.

The RVI anomaly was then used in conjunction with the optical data based NDVI anomaly to do a conformity analysis and ascertain the actual affected area, to eliminate bias and any uncertainty as both the sensors view the target differently. The overall methodology flowchart is given in Fig. 7.6.

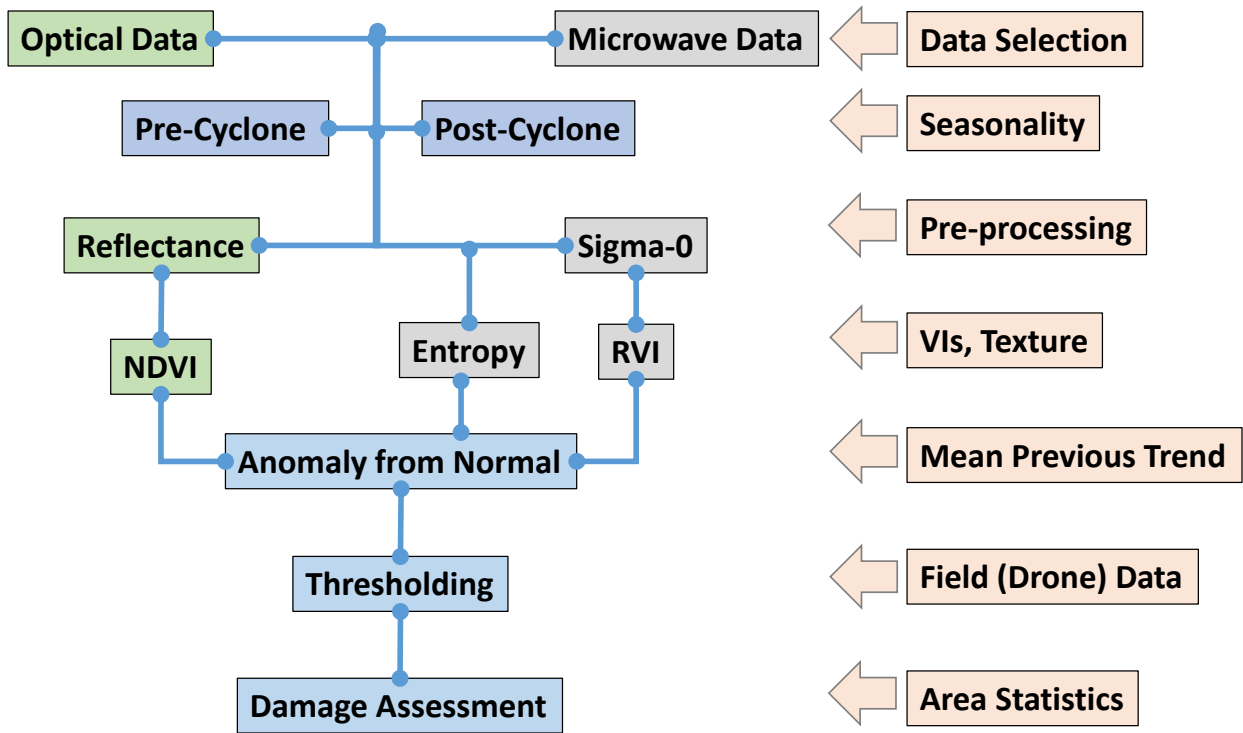


Figure 7.6: Methodology flowchart for assessment of apparent damage in Gir protected area.

7.3 Results and Discussion

Since two different methods of evaluation having different physical basis of observations were adopted the results were first analyzed separately. The optical method of observation relied mainly on detecting the changes in greenness level considering the fact that some of the areas along the moisture zone (drainages) which were having leaf-on trees may have changed after being uprooted due to cyclone. The area affected due to cyclone were mainly found scattered around the moisture zone in the Gir protected areas as seen in Fig. 7.7. The area statistics is provided in Table 7.2, which indicates that around 22% area was affected under moderate to high category.

SAR backscatter values from the forest vegetation during the driest months of the year tend to show a decrease which is more prominent in the VH polarization. The affected areas showed anomaly in backscatter which could be due to two main reasons, the structural changes in the tree orientation and the underlying soil. As scattering from soil under the uniform roughness conditions can be considered nearly similar both under very dry and very wet conditions, it was assumed to contribute marginally to the mean difference of RVI pre and post cyclone. The changes in the backscatter can be attributed more to the trunk and branches (Fig. 7.8). From the synergistic use

of entropy, cross polarisation ratio and backscatter from target in VH polarisation, the affected areas could be identified as shown in Fig. 7.9. Though the whole sanctuary was affected, the eastern part shows slightly more changes than the west.

To further the analysis, the post cyclone RVI was compared against the mean RVI of the preceding five years data and the anomaly in the RVI revealed the significant changes in the backscatter which are indicative of the affected area. From the difference of the RVI it was found that most of the sanctuary was affected. The changes in SAR based RVI anomaly data is mainly attributed to change in structural component (vertical trees in pre-cyclonic period to horizontal trees in post cyclonic period), assuming that moisture in the area due to rains remain same. The result of the anomaly in RVI is shown in Fig. 7.10 and areas statistics is given in Table 7.3, which indicates that around 21% area was affected under moderate to high category. Though the figures in both assessment looks similar, the spatial disturbance zones do not have complete match. Therefore, a map was constructed using both these outputs to have an agreement on spatial disturbances.

The ensemble product of optical and SAR data was generated and thresholding was done to arrive at qualitative assessment on varying degree of damages caused by Tauktae cyclone. Fig. 7.11 and Table 7.4 gives the map and statistics, respectively on areas affected. As per this final output, around 30% area was found affected by the cyclone in moderate to high category. It can be observed (Fig. 7.11) that the eastern part of the Gir protected area is affected more than the western part. The estimated area has inherent error margin of $\pm 5\%$, with a confidence level of 95% arising due to mapping inaccuracies.

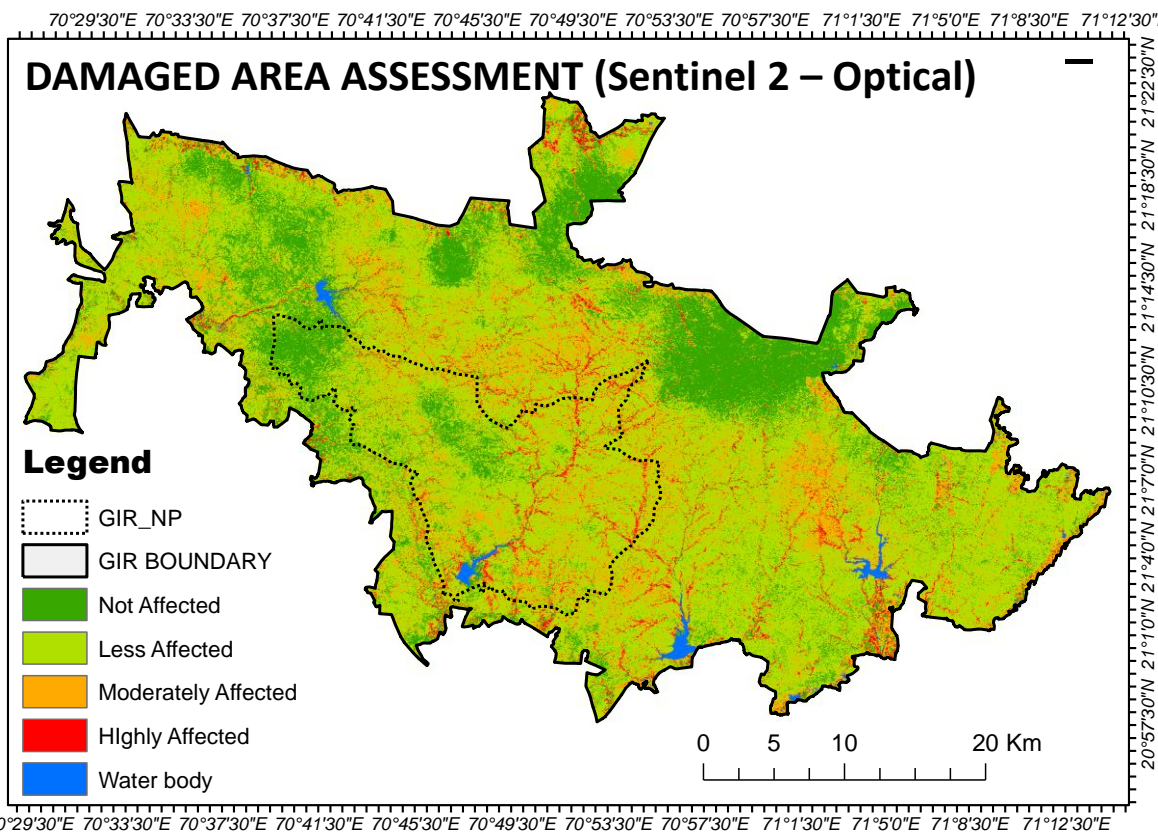


Figure 7.7: Map showing affected areas with varying degree due to Tauktae cyclone in Gir protected area as assessed from mean NDVI anomaly observed in post-cyclone data from Sentinel-2 (Optical).

Table 7.2: Area statistics on damage due to Tauktae Cyclone in Gir protected area as assessed from mean NDVI anomaly from post-cyclone data of Sentinel-2B.

SN	Value	Area (Sq Km)	Area (%)
1	Not Affected	291	20.0
2	Less Affected	834	57.4
3	Moderately Affected	255	17.6
4	Highly Affected	60	4.1
5	Water body	12	0.8
	Total	1452	100

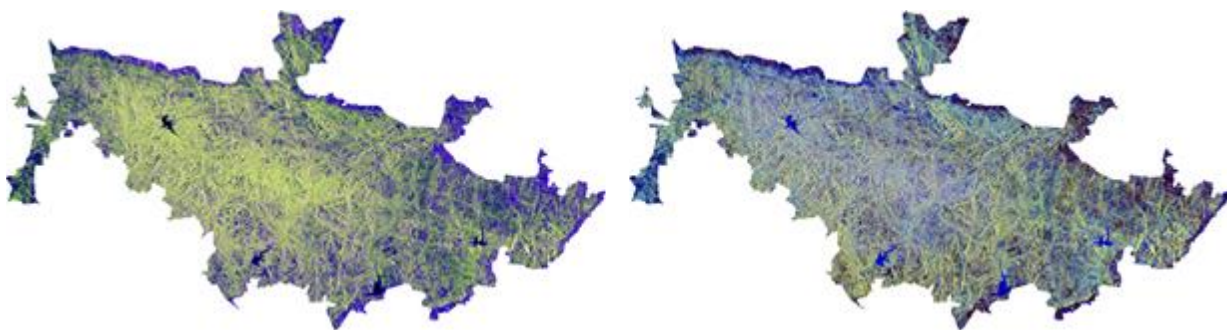


Figure 7.8: Color composite of VV, VH and VV/VH: pre-cyclone (Left) & post cyclone (right)

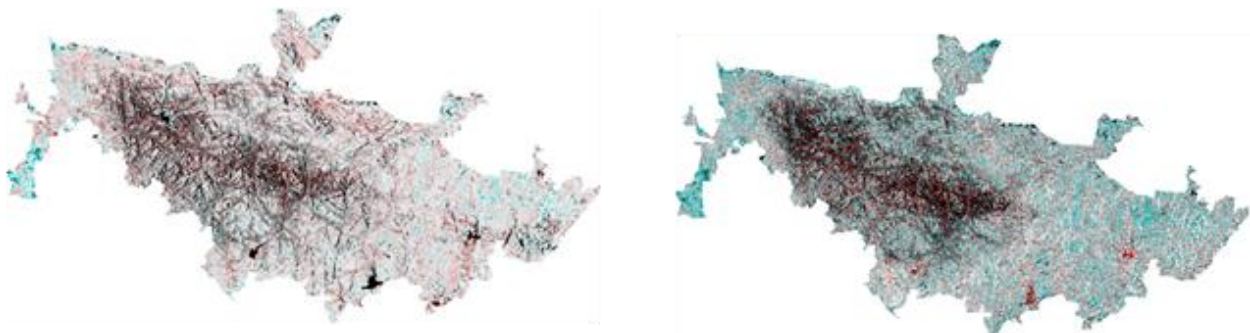


Figure 7.9: (Left) Color composite of Entropy pre-cyclone and (right) pre & post cyclone entropy difference

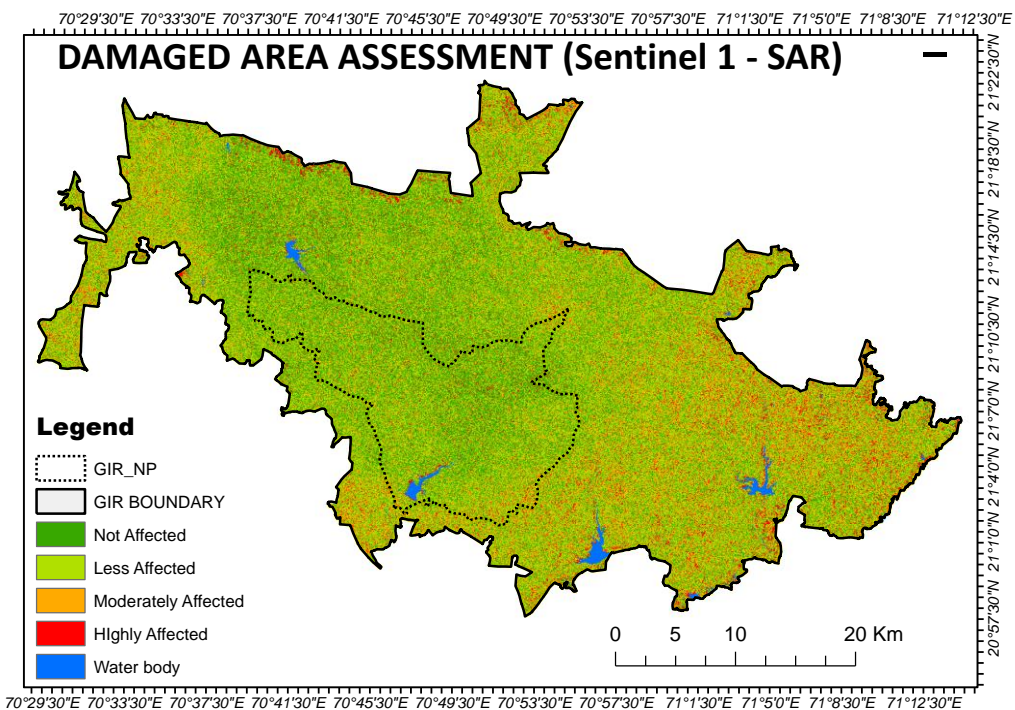


Figure 7.10: Map showing affected areas with varying degree due to Tauktae cyclone in Gir protected area as assessed from mean RVI anomaly observed in post-cyclone data from Sentinel-1 (SAR).

Table 7.3: Area statistics on damage due to Tauktae Cyclone in Gir protected area as assessed from mean RVI anomaly from post-cyclone data of Sentinel-1.

SN	Value	Area (Sq Km)	Area (%)
1	Not Affected	470	32.7
2	Less Affected	651	45.1
3	Moderately Affected	196	13.3
4	Highly Affected	123	8.1
5	Water body	12	0.8
	Total	1452	100

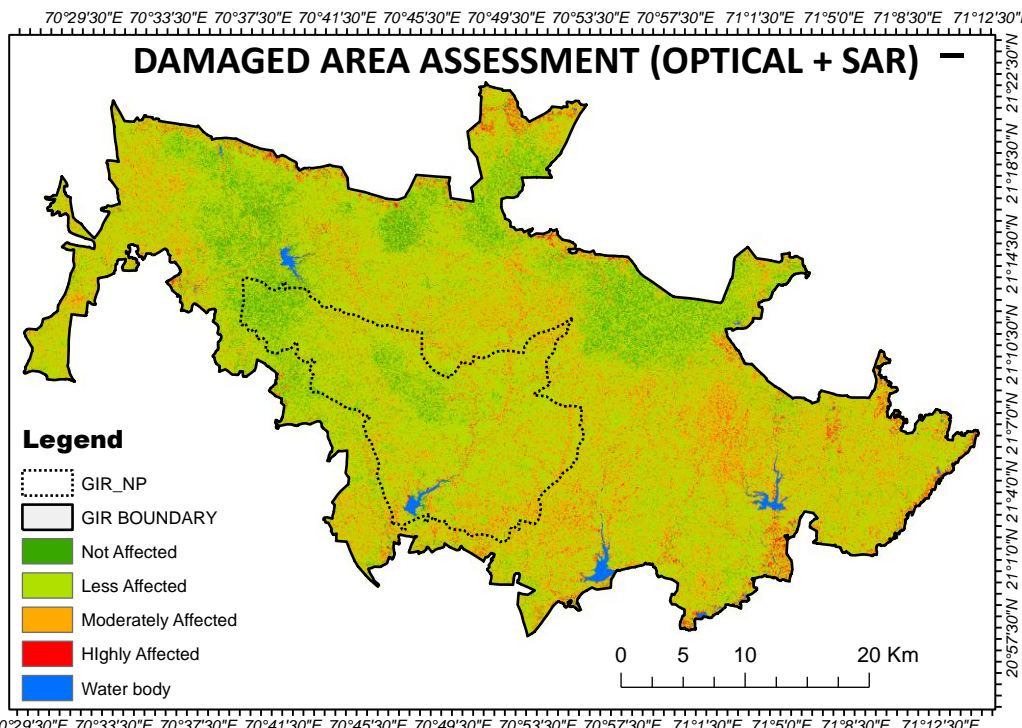


Figure 7.11: Map showing affected areas due to Tauktae cyclone in Gir protected area as assessed from combination of NDVI anomaly from Sentinel-2 (Optical) and RVI anomaly from Sentinel-1 (SAR) data.

Table 7.4: Area statistics on damage due to Tauktae Cyclone in Gir protected area as assessed from ensemble of mean NDVI anomaly and mean RVI anomaly products.

SN	Value	Area (Sq Km)	Area (%)
1	Not Affected	104	7.2
2	Less Affected	895	61.6
3	Moderately Affected	401	27.6
4	Highly Affected	40	2.8
5	Water body	12	0.8
	Total	1452	100

7.3 Conclusions

The Tauktae cyclone has affected 30% (441 sq km) of the Gir protected area with moderate to severe impacts primarily distributed in eastern Gir to Central Gir. Considering the average density of the trees in Gir forest to be 75 Trees / ha, and an affected area of 44100 ha, it is predicted that around 33 lakh trees would have been affected (under moderate to high category). More analysis with very high-resolution data may be taken up to assess quantitative damages and loss of trees.

References

1. Alam, M.S., Khan, J.A., Pathak, B.J., Kumar, S., 2014, Assessment of forest density using geospatial techniques of a tropical protected area, International Journal of Scientific and Research Publications, 4(3) (ISSN 2250-3153).